NONLINEAR SPECTROSCOPY OF SUPPORTED SIZE-SELECTED SILVER CLUSTERS (N=9-55) AND SUPPORTED CHIRAL 2,2′-DIHYDROXY-1,1′-BINAPHTHYL (BINOL) MOLECULES

PHILIPP HEISTER

Doctoral Thesis
Technische Universität München

Philipp Heister: *Nonlinear Spectroscopy of Supported Size-Selected Silver Clusters (n=9-55) and Supported Chiral 2,2′-Dihydroxy-1,1′-Binaphthyl (Binol) Molecules*

TECHNISCHE UNIVERSITÄT MÜNCHEN

Lehrstuhl für Physikalische Chemie

Nonlinear Spectroscopy of Supported Size-Selected Silver Clusters (n=9-55) and Supported Chiral 2,2′-Dihydroxy-1,1′-Binaphthyl (Binol) Molecules

Philipp Heister

Vollständiger Abdruck der von der Fakultät für Chemie der Technischen Universität München zur Erlangung des akademischen Grades eines

Doktors der Naturwissenschaften

genehmigten Dissertation.

Vorsitzender:
Univ.-Prof. Hubert Gasteiger, Ph.D.
Prüfer der Dissertation
1. Univ.-Prof. Dr. Ulrich K. Heiz
2. Univ.-Prof. Dr. Steffen J. Glaser

Die Dissertation wurde am 16.06.14 bei der Technischen Universität München eingereicht und durch die Fakultät für Chemie am 17.07.14 angenommen.

ABSTRACT

Supported size-selected metal clusters are the focus of intensive research since they possess promising (catalytic) properties. The potential development of heterogeneous enantio-selective catalysts plays an important role in this context. Spectroscopic investigations can lead to a better understanding of these catalytic properties. A major challenge here is the very weak signal of such samples as well as the proof of their potential chirality. In order to investigate supported clusters surface-sensitive (Surface-Second-Harmonic-Generation) and chiral-selective (Second-Harmonic-Generation Optical-Rotatory-Dispersion) spectroscopic methods are developed and applied to an experimental setup which allows for the deposition of size-selected clusters. Using these spectroscopic methods, the chiral molecule ($2, 2'$-dihydroxy - $1, 1'$-binaphthyl) is studied and an extremely chiral-selective resolution is revealed. Supported size-selected silver clusters (Ag_9 to Ag_{55}) are investigated spectroscopically. A size-dependent resonance of this non-scalable regime is detected which cannot be explained classically (Mie theory), but by considering quantum size effects. Cluster oxygen interactions are further investigated.

ZUSAMMENFASSUNG

Größenselektierte Metallcluster auf Oberflächen werden intensiv erforscht, da sie vielversprechende katalytische Eigenschaften besitzen. Die potentielle Entwicklung heterogener enantio-selektiver Katalysatoren spielt dabei eine wichtige Rolle. Zum besseren Verständnis dieser katalytischen Eigenschaften tragen spektroskopische Untersuchungen bei. Hierbei stellen das sehr schwache Signal solcher Proben sowie der Nachweis der möglichen Chiralität die größte Herausforderung dar. Um die Metallcluster spektroskopisch zu untersuchen, werden Oberflächen-sensitive (S-SHG) und Enantiomer-selektive (SHG-ORD) spektroskopische Methoden entwickelt und zum experimentellen Aufbau hinzugefügt, der die Deponierung von größenselektierten Clustern auf Oberflächen ermöglicht. Mit Hilfe dieses spektroskopischen Aufbaus wird das chirale Molekül ($2, 2'$-dihydroxy - $1, 1'$-binaphthyl) untersucht und die extrem hohe chiral-selektive Auflösung verdeutlicht. Größenselektierte Silbercluster (Ag_9 bis Ag_{55}) werden ebenfalls spektroskopisch untersucht. Dabei wird eine größenabhängige Resonanz in diesem nicht skalierbaren Bereich nachgewiesen, die nicht klassisch (Mie-Theorie), sondern nur durch quantenmechanische Effekte erklärt werden kann. Außerdem werden Cluster-Sauerstoff Wechselwirkungen untersucht.

CONTENTS

Part I

INTRODUCTION

INTRODUCTION

A "cluster" is an ensemble of bound atoms or molecules that consists of between 3 and $\sim$ 1000 particles. Above this size, it is referred to as nanoparticle. Cluster science emerged in the last $\sim$ 30 years and is a growing and highly interdisciplinary research field with important impact in the field of physics and chemistry [1, 2], biology and medicine [3], material science and nanotechnology [4].

One purpose of cluster science is to study the gradual development from small molecular-like clusters to their corresponding bulk materials [5]. Here, clusters represent an important kind of condensed matter of its own - an intermediate state between atoms on the one hand and the solid or liquid state on the other hand. This is attributed to their different physical and chemical character and properties which can be divided into two regimes; the scalable regime (of nanoparticles) where the properties monotonically converge toward their corresponding bulk values and the so called non-scalable regime for small clusters. Here, physical and chemical properties strongly vary as a function of size, e.g by the addition of a single atom, and are not scalable from those of the corresponding bulk material.

Clusters in this non-scalable regime posses surprising, outstanding and otherwise not observed electronic, optical and catalytic properties. As these properties are not governed by the periodic table, a common method seen in literature is to expand the periodic table by a third dimension which comprises the number of atoms building the cluster [6]. In this regime unexpected phenomena are observed due to quantum confinement and boundary effects [7, 8], e.g. clusters of nonmagnetic elements become magnetic [9], the color of particles changes with size and noble metals become reactive [10, 11].

Metal clusters are of great interest in chemical and pharmaceutical industry because of their catalytic properties. In catalysis a reactant (e.g. a molecule) is modified by the electronic interaction with a catalyst (e.g. a supported metal cluster) which enhances the turnover frequency of a chemical reaction by offering an energetically favorable pathway.

The added value by catalysis in the chemical industry is of enormous economic importance, since over 80% of all chemical products are produced with the aid of catalytic processes [12]. A great number of these chemical products is achieved by heterogeneously catalyzed processes where the easy separation of the catalyst from reactants and products is beneficial. By optimizing these catalysts the energy and resources used can be significantly reduced which is thus of great economic and hence scientific interest.

Supported clusters are especially interesting due to their chemical reactivity and applications in heterogeneous catalysis. One big advantage of clusters is the high surface-atom to volume ratio. This value is especially interesting when surface effects, e.g. for catalytic reactions are used and investigated.

However, unlike common practice in heterogeneous catalysis where the catalytic performance scales with the surface to volume ratio of the dispersed catalytic agent, small size-selected catalysts are distinguished by their unique and non-scalable properties that originate from the highly reduced dimensions of the active catalytic aggregates. Chemical and physical properties of these systems present new opportunities for tuning and control of chemical activity, specificity, and selectivity [13].

The dependency of catalytic activity on cluster size is truly a breakthrough in cluster science and has triggered many experiments on gas phase and on supported size-selected clusters [14, 15, 10, 16, 17].

A further area of special and recent interest are chiral metal clusters. One approach in the last ~ 15 years was to induce chirality in metal clusters by chiral ligands [18, 19]. The observed chiroptical (CD) effect was either attributed to intrinsically chiral cores [20, 21], or to the dissymmetric field of the chiral adsorbates which influence the electrons of the cluster without changing their geometrical lattice [22, 23]. Chiral clusters are of special interest in heterogeneous catalysis as they may lead to enantioselective heterogenous catalytic reactions.

However, the development of enantioselective catalysts is an enormous challenge which has led to new approaches in the study of catalysis by attempting to selectively adjust the catalytic properties of supported metal clusters [24].

For this future goal small, supported, size-selected, chiral clusters need to be tailored and their chirality has to be detected and verified. The tailoring of the properties of a cluster catalyst towards a specific catalytic application, however, requires an understanding of the influence of various factors on the catalytic activity, such as the cluster size, the cluster shape and symmetry, and the influence of the support material. Consequently, systematic studies are needed. Here, the investigation of the electronic structure of metal clusters can play a central role since the intrinsic catalytic activity of a catalyst is mainly determined by its electronic properties. Thus, one way to gain information on the catalytic properties of metal clusters is the study of their electronic structure [25].

Here, spectroscopy comes into play as it is an optimal technique to address electronic structures. Clusters have been spectroscopically investigated in the gas phase [26], embedded in matrices [27], in solutions and at surfaces [28][1]. However, supported clusters are of high importance since they deliver the most practical way of applied implementation. In this regard the interaction between clusters and the support material is of great scientific interest because support materials may strongly influence the observed optical properties by manipulating the electronic structure of the clusters. The medium surrounding the clusters affects the properties of the cluster/medium system. Therefore, this system as a whole should be studied [29].

The spectroscopic investigation of supported size-selected clusters is very challenging and thus sophisticated methods are needed. In order to investigate potential properties in the non-scalable regime the investigated sample must contain only clusters of one single size which are mono-disperse on the surface in order to avoid agglomeration. This can only be achieved by keeping the surface coverage very low. Therefore, the following requirements of the experimental setup are mandatory.

Firstly, a sophisticated cluster source is needed, that produces clusters with the size of interest in a sufficiently high amount. Secondly, the mono-disperse, supported and size-selected clusters lead - in contrast to gas-phase studies and investigations of clusters embedded in matrices - to very weak signals. Hence, an extremely sensitive spectroscopic method has to be applied. Thirdly, in order to investigate potential supported chiral clusters or supported chiral cluster-molecule complexes [30], a chiral-sensitive spectroscopic method has to be applied to the experimental setup. This is very challenging since the aforementioned conditions must be fulfilled simultaneously.

Small silver clusters are known to possess giant resonances [31], which can be attributed to a collective electron oscillation, classically named the Mie-resonance. Silver is also known to oxidize under certain conditions. These aspects make silver the ideal material for spectroscopic investigations of supported metallic clusters and their potential interaction (oxidation) with adsorbed molecules.

Size-selected silver clusters have been studied in the gas phase [32], in cold inert matrices [33, 34, 35, 36] and theoretically [32, 37]. Unselected silver clusters (nanoparticles) have also been investigated on support materials [38, 39]. However, no spectroscopic data of truly size-selected supported metal clusters have been published. This lack of data results from the aforementioned challenges which must be overcome. In terms of heterogeneous catalysis, however, this size regime is of greatest importance since it was shown that supported small size-selected clusters can show remarkable catalytic behavior. Also, for the design of chiral supported clusters this size regime is especially important, since chirality can be induced more easily than

---

[1] The book by U. Kreibig and M. Vollmer is a great summary of both, the optical properties of metal clusters and the performed experiments on metal clusters up to it's publication in 1995 and hence highly recommended for the interested reader [28].

for bigger clusters, where the large number of possible isomers might impede chirality.

Topic

The central purpose of this thesis is the spectroscopic investigation of size-selected silver clusters ($9 - 55$ atoms) and chiral molecules which are both supported on a substrate. Therefore, a highly sensitive spectroscopic setup has to be established and applied to an already existing cluster source which allows for both: The detection of the very weak expected signals from small supported mono-disperse size-selected silver clusters as well as the chiral-sensitive investigation of enantiopure adsorbates. This is especially challenging as both spectroscopic systems should complement one another and allow for measurements of the very same sample. As shown in this work nonlinear (SHG) spectroscopy is the perfect spectroscopic method to fulfill both aforementioned requirements. In order to perform these measurements, the existing experimental setup has to be modified for the production and subsequent investigation of these samples under UHV conditions.

To achieve this, a first step is the characterization and spectroscopic investigation of the support material which is a continuation of previous work [25]. The second step is the chiroptical spectroscopic investigation of the chiral probe molecule ($2,2'$-dihydroxy-$1,1'$-binaphthyl). Here, of special interest is the evolution of the nonlinear chiroptical signal from very low coverages to thin molecular films. In a third step the evolution of the optical (electronic) properties of supported size-selected silver clusters with the cluster sizes ($9 - 55$ atoms) is of central interest.

The results should contribute towards a better understanding of the role of those clusters in catalytic reactions. The combination of both the spectroscopic investigation of size-selected clusters and the chiroptical investigation of thin molecular films could lead to the production of supported size-selected chiral metal clusters which would be a huge step towards heterogeneous enantioselective catalysis.

Outline

This thesis is divided into seven main chapters (marked in red in the table of contents) which are in turn subdivided into several sections. The *Introduction* chapter is followed by the *Theory* chapter where a theoretical background of the spectroscopic methods is given. Here, a special focus is placed on the nonlinear susceptibility tensor $\chi^{(2)}$ as it defines the nonlinear response of the investigated system. By looking at the symmetry properties of $\chi^{(2)}$ both spectroscopic methods which are used in this thesis are derived: S-SHG spectroscopy is introduced and shown to be an extremely sensitive method for the investigation of adsorbates on surfaces. SHG-ORD spectroscopy is introduced as an extraordinarily chiral-selective method for the investigation of chiral adsorbates on surfaces. The optical properties of the probe molecule $2,2'$-dihydroxy - $1,1'$-binaphthyl (Binol) as well as of small (size-selected) metal clusters on surfaces and their interaction with adsorbed molecules are described.

In the next chapter *Experiment* the experimental setup which was built and used for all data presented in this thesis is introduced.

The following *Result* chapter is divided into two main sections. In the first section the experimental results of the nonlinear chiral-selective response of thin molecular films of $2,2'$-dihydroxy - $1,1'$-binaphthyl (Binol) molecules are presented. Here, the great chiral-selective sensitivity of the applied spectroscopic setup is revealed. In the second section the first nonlinear spectra of supported size-selected silver clusters are presented. Special attention is given to the resonance energies as a function of cluster size. Also, the nonlinear investigation of the interaction of supported size-selected silver clusters with background gases is presented.

In the *Summary and Outlook* chapter the experimental results are summarized and suggestions for further investigations are proposed. It is followed by the *Bibliography* and the *Appendix* chapter. Here additional information concerning this thesis are summarized.

Part II

THEORY

1

THEORY

In this chapter the theoretical background for the investigated systems and the investigating spectroscopic methods is given. The chapter is composed of different sections. Firstly, an overview of the linear and nonlinear interaction of light with matter is given, followed by a detailed description of the nonlinear susceptibility tensor $\chi^{(2)}$. Surface-Second-Harmonic-Generation (S-SHG) spectroscopy, as well as Second-Harmonic-Generation Optical-Rotatory-Dispersion (SHG-ORD) spectroscopy are derived from the symmetry properties of $\chi^{(2)}$. It is shown, that S-SHG is a very sensitive and effective nonlinear spectroscopic method for the investigation of adsorbates on surfaces and that SHG-ORD is an extremely chiral-sensitive tool to probe chiral adsorbates at interfaces[1]. The optical properties of the probe molecule $2,2'$-dihydroxy-$1,1'$-binaphthyl (Binol) as well as of small (size-selected) metal clusters on surfaces are described. Here, Mie theory is introduced and expanded by theoretical considerations derived for the "quantum size regime" of very small size-selected clusters. This chapter is concluded with the discussion of possible cluster-cluster, cluster-substrate and cluster-adsorbate interactions.

1.1 LINEAR AND NONLINEAR OPTICS

1.1.1 *Linear Optical Interaction of Light and Matter*

Electromagnetic radiation or light[2] was first classically predicted by James Clerk Maxwell in four equations (Maxwell equations) between 1861 and 1862 [46].

This classical approach has been proven to be very useful in spectroscopy. It is able to provide a better understanding of the studied systems. In nonlinear optics many observations can be explained by the picture of a harmonic and anharmonic oscillator.

In the following description the one dimensional model of the harmonic oscillator is used to derive the fundamental interaction between light and matter. This is, however, a simplification of the used system but still provides important insights into all basic features of

---

[1] Most of the following theoretical background can be found in many standard books about light-and-matter-interaction as well as in books about second-order-nonlinear-optics. However, most of the here described summary is mainly based on following publications or books and can be found in greater detail there [40, 41, 42, 43, 44, 45].

[2] "Visible Light" is called the small visible part of the electromagnetic radiation between 380 nm and 780 nm.

linear and nonlinear optics. Later, the treatment is expanded to three dimensions, where it is of importance for the theoretical description.

A simple solution of the Maxwell-equations is a monochromatic wave given by a varying electric field, E, which can be written as:

$$E(r,t) = E_0(e^{i(kx-wt)} + c.c.) \tag{1}$$

where, $E(r,t)$, is an electromagnetic field which varies by time, t and, space x. E_0 is a constant amplitude, ω is the angular frequency[3], and $k = \frac{2\pi n}{\lambda}$ the unit vector in direction of propagation. "c.c." denotes complex conjugate.

The following theoretical description is done within the electric dipole approximation[4]. Matter consists of charged particles: negatively charged electrons and positively charged nuclei. An oscillating electric field interacts with these particles leading to a movement induced by the field. Since the positively charged protons have a much larger mass than the electrons $\left(\frac{M_P}{M_E} \approx 1836\right)$, the motion of the electrons is more significant for optical frequencies. In dielectrics[5] this charge separation leads to an induced dipole moment, $\mu^{(1)}(\omega)$, which oscillates at the same frequency as the applied optical field. For sufficient low light intensities[6] the relation between the induced dipole moment, $\mu^{(1)}(\omega)$, of individual particles and the electric field, $E(\omega)$, is given by the linear relation:

$$\mu^{(1)}(\omega) = \alpha^{(1)}(\omega)\, E(\omega) \tag{2}$$

$\alpha^{(1)}(\omega)$ describes the frequency dependent first-order polarizability. The induced dipole moment, $\mu^{(1)}(\omega)$, will thus oscillate at the same frequency as the applied optical field and also emit electromagnetic radiation. The polarization, $P(\omega)$, of the entire (isotropic dielectric) medium is given by the sum over all induced dipole moments[7]:

$$P(\omega) = \sum_i \mu_i^{(1)}(\omega) = \varepsilon_0 \chi^{(1)}(\omega) E(\omega) \tag{3}$$

with the permittivity of vacuum $\left(\varepsilon_0 \approx 8{,}854 \frac{A^2 s^4}{m^3 kg}\right)$ and with the first-order electric susceptibility, $\chi^{(1)}(\omega)$, which contains all information of

---

[3] The angular frequency is given by: $\omega = \frac{2\pi c}{\lambda}$, where λ is the wavelength and c the speed of light in vacuum.

[4] The electric dipole approximation is valid as long as the wavelength of the interacting radiation is much larger than typical sizes of atoms, which is the case in UV/VIS spectroscopy. Then, the following approximation is valid: $e^{(-ikr)} = 1 + i\frac{2\pi n}{\lambda}r + ... \approx 1$.

[5] A dielectric is an electric insulator which can be polarized by an applied electric field. Thus, the charges change their position from the equilibrium within the dielectric but do not "flow" as it would be the case for a conductor.

[6] The light intensity is "sufficiently low" as long as the charges oscillate in an harmonic potential, which is a good approximation for small displacements.

[7] The linear susceptibility $\chi^{(1)}$ is treated as a scalar here. This is due to the assumed isotropy of the medium and is valid if the polarization density is parallel to the applied electric field. In general however, $\chi^{(1)}$ must be treated as a matrix.

the macroscopic medium and describes processes such as dispersion, refraction, reflection, absorption and scattering. It is a dimensionless frequency-dependent complex quantity, where the real part describes the refraction and the imaginary part the absorption of radiation respectively ($\chi^{(1)}(\omega) = \chi' + i\chi''$).

For sufficient low intensities the induced motion of the electrons in dielectric media can be described by a harmonic oscillator given by:

$$\frac{d^2x(t)}{dt^2} + 2\gamma\frac{dx(t)}{dt} + \omega_0^2 x(t) = -\frac{e}{m}E(x,t) \tag{4}$$

where, ω_0, is the resonant frequency[8] and, γ, is the damping constant. The elementary charge is given by $e = 1.602176565(35)\times10^{-19}$ C. Inserting the applied optical field from Equation 1 the solution is given by:

$$x(t) = \frac{-e}{m}E_0\frac{e^{i(kr-\omega t)}}{\omega_0^2 - 2i\gamma\omega - \omega^2} + c.c \tag{5}$$

This solution gives the displacement, $x(t)$, as a linear function of the electric field $E(t)$. Using N electrons the macroscopic polarization, $P(t)$, is given by $P(t) = -Nex(t)$ which leads, along with Equation 3, to the linear susceptibility:

$$\chi^{(1)}(\omega) = \frac{Ne^2}{\epsilon_0 m}\frac{1}{\omega_0^2 - 2i\gamma\omega - w^2} \tag{6}$$

The real and the imaginary parts describe refraction and absorption respectively[9]:

$$Re\left[\chi^{(1)}(\omega)\right] = \chi'(\omega) = \frac{Ne^2}{\epsilon_0 m}\frac{\omega_0^2 - \omega^2}{(\omega^2-\omega_0^2)^2 + (2\gamma\omega)^2} \tag{7}$$

$$Im\left[\chi^{(1)}(\omega)\right] = \chi''(\omega) = \frac{Ne^2}{\epsilon_0 m}\frac{2\gamma\omega}{(\omega^2-\omega_0^2)^2 + (2\gamma\omega)^2} \tag{8}$$

The real part as well as the imaginary part are plotted in Figure 1. It can be seen, that at the resonant frequency, ω_0, the absorption of, $\chi^{(1)}$, has it's maximum (the imaginary part is maximal) and for the real part a full π dephasing occurs.

In anisotropic materials, where the polarization is not parallel to the applied electric field, the linear susceptibility must be treated as a matrix (tensor of rank 2 with 9 components) and is thus given by:

$$P_i = \sum \varepsilon_0 \chi_{ij}^{(1)} E_j \tag{9}$$

Here for example, the material can be polarized in the y-direction by applying an electric field in the z-direction. For an isotropic medium

---

[8] ω_0 is given by the "spring constant" k and the mass m: $\omega_0 = \sqrt{\frac{k}{m}}$.

[9] $\frac{Ne^2}{\epsilon_0 m_e} = \omega_p^2$ is often referred to as the plasma frequency (see Section 1.5.2).

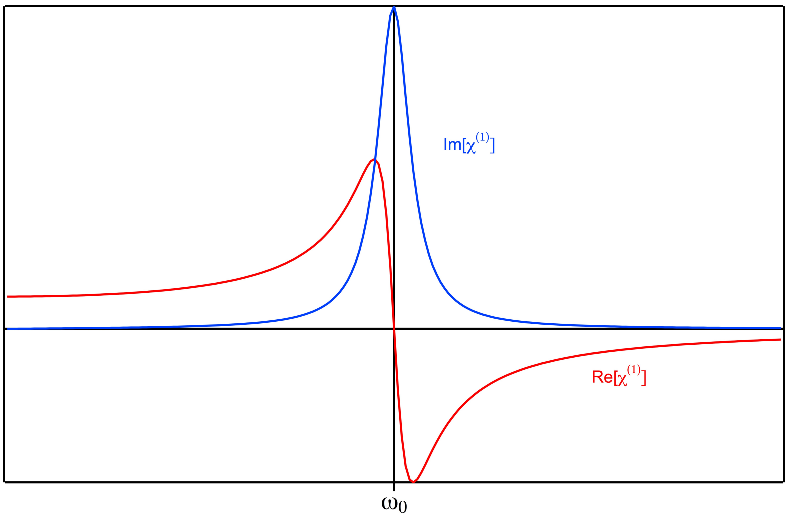

Figure 1: Real and imaginary part of the linear susceptibility, $\chi^{(1)}$, at resonance frequency ω_0. The resonance function is given by the imaginary part (blue line) and the dispersion function is given by the real part (red line).

only 3 components remain which are equal. Equation 9 is then given by:

$$\begin{bmatrix} P_x^{(1)} \\ P_y^{(1)} \\ P_z^{(21)} \end{bmatrix} = \begin{bmatrix} \chi_{xx}^{(1)} & 0 & 0 \\ 0 & \chi_{yy}^{(1)} & 0 \\ 0 & 0 & \chi_{zz}^{(1)} \end{bmatrix} \begin{bmatrix} E_x \\ E_y \\ E_z \end{bmatrix} \tag{10}$$

The remaining components are $\chi_{xx}^{(1)}=\chi_{yy}^{(1)}=\chi_{zz}^{(1)}$. Hence in isotropic media the linear susceptibility can be treated as a scalar.

1.1.2 *Chirality in Linear Optics*

There are two well known techniques in linear optics to measure chirality: Optical-Rotatory-Dispersion (ORD) and Circular-Dichroism (CD) spectroscopy. In linear optics, where the applied electric field is weak compared to internuclear atomic fields, measurements of CD and ORD are techniques often used to probe chiral molecules in solution or in gas phase [47, 48, 49]. ORD describes the phenomenon that the plane of linear polarized light is rotated about the direction of motion while passing through a chiral material. These materials are referred to as "optically active". This effect can easily be understood on the macroscopic level by replacing the linear polarized light by two circular-polarized beams rotating clockwise and anti clockwise respectively. As the optically active medium exhibits different properties for right-circular-polarized light and left-circular-polarized light (i.e. index of refraction) one beam will lag behind the other. Representing the two circular polarized waves by a plane polarized wave after passing the medium, leads to a rotation of the polarization compared to it's original orientation. The relation between the rotation and the difference in refraction indices is given by:

$$\delta = \frac{\pi \nu z}{c}(n_l - n_r) \tag{11}$$

where δ is the angle by which the plane polarized light has been rotated (see Figure 2). It can be seen that the rotation is caused by the difference in refraction $(n_l - n_r)$ of the optically active medium where the amount of rotation of the polarization depends on the thickness z (path-length) of the medium. In Circular-Dichroism however, the difference between the absorption of two circular polarized beams which travel through the optically active medium is measured.

For a deeper theoretical description of Optical-Rotatory-Dispersion and Circular-Dichroism the linear polarization must be expressed by the first order linear susceptibility, $\chi_e^{(1)}$, as well as the first order linear magnetic susceptibility $\chi_m^{(1)}$. The polarization, $\vec{P}^{(1)}$, is then induced by the electric field, $\vec{E}$, as well as by the magnetic induction field, $\vec{B}$, of the incoming light:

$$\vec{P}^{(1)}(\omega) = \chi_{ee}^{(1)}\vec{E}(\omega) + \chi_{em}^{(1)}\vec{B}(\omega) \tag{12}$$

$$\vec{M}^{(1)}(\omega) = \chi_{me}^{(1)}\vec{E}(\omega) \tag{13}$$

$\vec{M}^{(1)}(\omega)$ is the induced magnetization, $\chi_{ee}^{(1)}$, denotes the linear electric susceptibility and $\chi_{em}^{(1)}$ and $\chi_{me}^{(1)}$ the linear magnetic susceptibilities respectively[10]. It can be shown that the presence of a magnetic susceptibility explains the difference in refractive index for left- and right-polarized light. $\chi_{em}^{(1)}$ and $\chi_{me}^{(1)}$ change signs between enantiomers and vanish in achiral or racemic materials. In fact molecules must possess both, an electric and a magnetic allowed dipole transition, of approximately the same magnitude, in order to show optical activity such as ORD and CD in linear optics [50]. It will be shown later, that this is a big difference to a nonlinear optically active medium. The refractive indices for left- and right polarized light are given by:

$$n_{l,r} = \sqrt{1 + 4\pi\chi_{ee}^{(1)} \mp 8i\pi\chi_{em}^{(1)}}$$

---

[10] The subscript "e" refers to an electric-dipole transition and the superscript "m" refers to a magnetic-dipole transition. For example, "*em*" refers to an interaction where a photon is annihilated through a magnetic-dipole interaction and a photon is being created through an electric-dipole interaction. The two first-order magnetic susceptibilities can be related to each other: $\chi_{me}^{(1)} = -\chi_{em}^{(1)}$ [40].

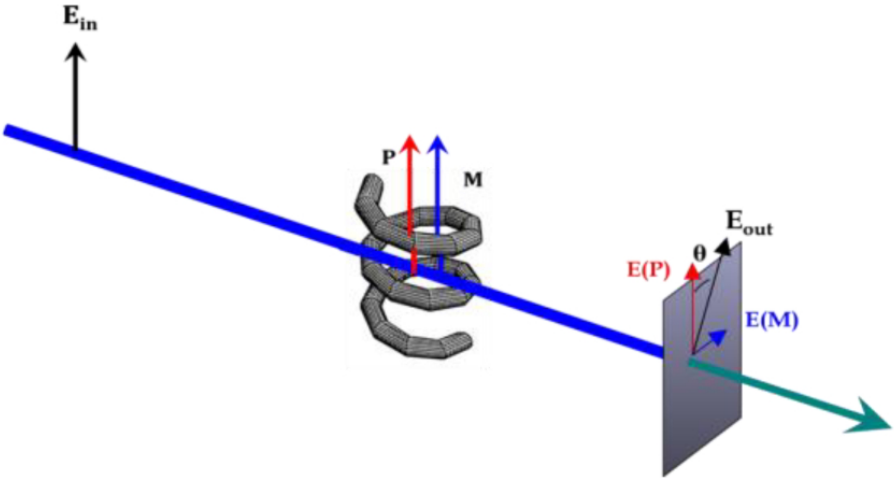

Figure 2: Schematic of the optical activity in a chiral helical molecule. The rotation of the plane of the polarization is shown [51]. The polarization (red) and magnetization (blue) act as an new source of radiation. The induced fields are perpendicular to each other, hence the polarization of the corresponding total field is rotated.

1.1.3 *Nonlinear Optical Interaction of Light and Matter*

In the previous section the relation between the polarization, $\vec{P}(\omega)$, and the applied electric field, $\vec{E}(\omega)$, was introduced for sufficiently low light intensities and thus for a harmonic potential approximation. The linear relation, however no longer holds for high light intensities $\vec{E}(\omega)$, which are comparable to internuclear atomic field strengths and in the range of $10^5 \frac{V}{m} - 10^8 \frac{V}{m}$. This is given for example by a pulsed laser [52]. In the following the nonlinear susceptibility, $\chi^{(2)}$, is introduced. For strong applied electric fields the relation between polarization, $\vec{P}$, and electric field, $\vec{E}$, is no longer linear and can be expanded in a Taylor series:

$$P_i = \varepsilon_0 \left(\sum_j \chi_{ij}^{(1)} E_j + \sum_{jk} \chi_{ijk}^{(2)} E_j E_k + \sum_{jkl} \chi_{ijkl}^{(3)} E_j E_k E_l + ... \right) \tag{14}$$

and accordingly:

$$\vec{P} = \varepsilon_0 \left(\chi^{(1)} \vec{E} + \chi^{(2)} \vec{E}\vec{E} + \chi^{(3)} \vec{E}\vec{E}\vec{E} + ... \right) \tag{15}$$

$\chi^{(2)}$ and $\chi^{(3)}$ are the second- and third-order susceptibilities, which describe the nonlinear optical response of the medium. As $\chi^{(3)}$ is magnitudes of orders smaller than $\chi^{(2)}$, it is sufficient to concentrate on the nonlinear susceptibility, $\chi^{(2)}$, for the measurements shown in this thesis and neglect higher order contributions [42][11]. The second order polarizability is given by:

---

[11] For solids the following estimation is approximately valid: $\chi^{(1)} \approx 1$, $\chi^{(2)} \approx 10^{-12} \frac{V}{m}$, $\chi^{(3)} \approx 10^{-21} \frac{V^2}{m^2}$ [53].

$$\vec{P}^{(2)} = \varepsilon_0 \chi^{(2)} \vec{E}\vec{E} \tag{16}$$

$\chi^{(2)}$ is of special interest in this thesis leading to second-harmonic-generation and nonlinear chiral effects which are essential for the experimental data presented later in this work. This can easily be seen by combining Equation 16 with the expression of the electric field from Equation 1[12]:

$$\begin{aligned}\vec{P}^{(2)} &= \varepsilon_0 \chi^{(2)} \vec{E}_0 (e^{i(\vec{k}\vec{r}-wt)} + c.c) \vec{E}_0 (e^{i(\vec{k}\vec{r}-wt)} + c.c) \\ &= \varepsilon_0 E_0^2 \chi^{(2)} \left(2 + (e^{i(\vec{2k}\vec{r}-2wt)} + c.c)\right)\end{aligned} \tag{17}$$

Here an additional term $2\varepsilon_0 E_0^2 \chi^{(2)}$ as well as a term with double frequency $(2\omega t)$ arises. The former is called optical rectification (OR) and the latter is responsible for Second-Harmonic-Generation (SHG)[13]. Similar to Equation 2 the second-order induced dipole moment for an individual particle can be written as:

$$\vec{\mu}^{(2)} = \alpha^{(2)} \vec{E}\vec{E} \tag{18}$$

For a system composed of N noninteracting particles the relation between the second order susceptibility and the induced dipole moments, $\alpha^{(2)}$, is given by:

$$\chi^{(2)} = N f \alpha^{(2)}$$

where, f, describes a local field factor which accounts for the effects of dipoles induced in the dielectric medium through electronic polarization. The nonlinear optical response of dielectric materials can be described using an anharmonic potential as an approximation for the motion of the bound electrons. This is given by the equation:

$$\frac{d^2x(t)}{dt^2} + 2\gamma \frac{dx(t)}{dt} + \omega_0^2 x + a x^2(t) = -\frac{e}{m} E(t) \tag{19}$$

where, $x(t)$, describes the position of the electron as a function of time, γ, the damping constant introduced previously, ω_0, is the resonance frequency, e the electron charge, and m the mass of the electron. a is a parameter that characterizes the strength of the nonlinearity. No general solution for this equation is known. However, it can be solved for a monochromatic exciting wave in the form of Equation 1 using perturbation theory, provided that the applied field is sufficiently weak [42]. Then the nonlinear susceptibility for second harmonic generation can be written as:

$$\chi^{(2)} = \frac{Ne^3 a}{\epsilon_0 m^2} \frac{1}{\left(\omega_0^2 - 4\omega^2 - 4i\omega\gamma\right)} \frac{1}{\left(\omega_0^2 - \omega^2 - 2i\omega\gamma\right)^2}$$

---

[12] Here, three dimensionality is used.

[13] For input waves with different frequencies, effects such as Sum-Frequency-Generation (SFG) and Difference-Frequency-Generation (DFG) occur.

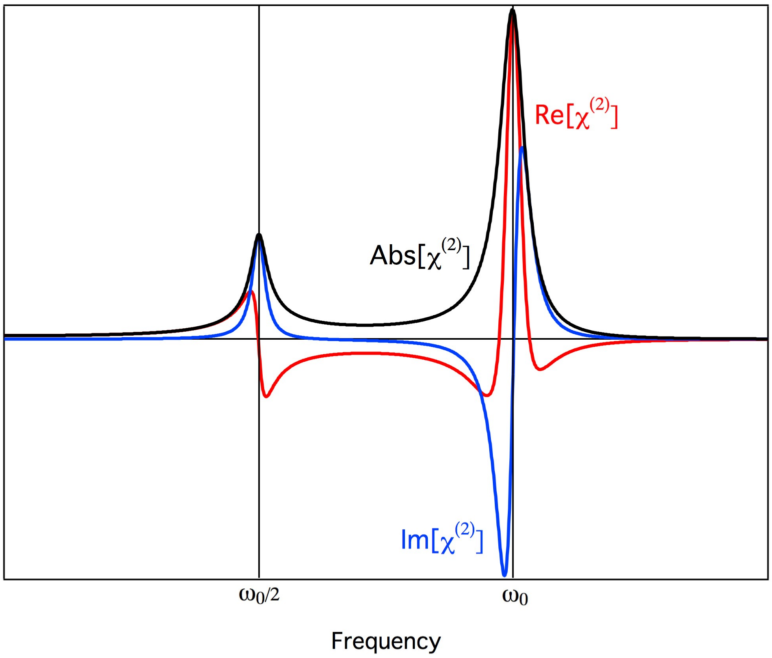

Figure 3: Real-, imaginary and absolute part of the nonlinear susceptibility $\chi^{(2)}$.

The signal intensity is proportional to $\left|\chi^{(2)}\right|^2$ and therefore

$$\left|\chi^{(2)}\right|^2 = \left(\frac{Ne^3a}{\epsilon_0 m^2}\right)^2 \frac{1}{\left(\left(\omega_0^2-4\omega^2\right)^2+\left(4\gamma\omega\right)^2\right)} \frac{1}{\left(\left(\omega_0^2-\omega^2\right)^2+\left(2\omega\gamma\right)^2\right)^2}$$

The nonlinear susceptibility possesses some distinct symmetry properties which are described in the following. $\left|\chi^{(2)}\right|^2$ is maximum whenever the denominator is small. This is the case for ω=ω_0 and $\omega = \frac{\omega_0}{2}$. Therefore $\chi^{(2)}$ has two resonance frequencies (in contrast to the linear susceptibility $\chi^{(1)}$). In Figure 3 the real- and imaginary part, as well as the square (black line) of the second order susceptibility tensor are plotted as a function of excitation energy. Two peaks at ω_0 and at $\frac{\omega_0}{2}$ can be observed.

1.1.4 *Properties of the Nonlinear Susceptibility Tensor* $\chi^{(2)}$

As described previously, the nonlinear polarization $\vec{P}^{(2)}$ is given by:

$$P_i^{(2)} = \sum_{j,k} \varepsilon_0 \chi_{ijk}^{(2)} E_j E_k \tag{20}$$

where $P_i^{(2)}$ is a component of the polarization vector, $E_{j,k}$ are components of the electric field vector and $\chi_{ijk}^{(2)}$ is a component of the nonlinear susceptibility tensor. $\chi^{(2)}$ is a third rank tensor[14] and therefore contains 27 components. Thus it is a $3 \times 3 \times 3$ matrix but can be written as a 9×3 matrix:

$$\chi^{(2)} = \begin{bmatrix} \chi^{(2)}_{xxx} & \chi^{(2)}_{xyy} & \chi^{(2)}_{xzz} & \chi^{(2)}_{xyz} & \chi^{(2)}_{xzy} & \chi^{(2)}_{xzx} & \chi^{(2)}_{xxz} & \chi^{(2)}_{xxy} & \chi^{(2)}_{xyx} \\ \chi^{(2)}_{yxx} & \chi^{(2)}_{yyy} & \chi^{(2)}_{yzz} & \chi^{(2)}_{yyz} & \chi^{(2)}_{yzy} & \chi^{(2)}_{yzx} & \chi^{(2)}_{yxz} & \chi^{(2)}_{yxy} & \chi^{(2)}_{yyx} \\ \chi^{(2)}_{zxx} & \chi^{(2)}_{zyy} & \chi^{(2)}_{zzz} & \chi^{(2)}_{zyz} & \chi^{(2)}_{zzy} & \chi^{(2)}_{zyx} & \chi^{(2)}_{zxz} & \chi^{(2)}_{zxy} & \chi^{(2)}_{zyx} \end{bmatrix} \tag{21}$$

One can then rewrite Equation 20 to[15]

$$\begin{bmatrix} P^{(2)}_x \\ P^{(2)}_y \\ P^{(2)}_z \end{bmatrix} = \begin{bmatrix} \chi^{(2)}_{xxx} & \chi^{(2)}_{xyy} & \cdot & \cdot & \cdot & \cdot & \cdot & \chi^{(2)}_{xxy} & \chi^{(2)}_{xyx} \\ \chi^{(2)}_{yxx} & \chi^{(2)}_{yyy} & \cdot & \cdot & \cdot & \cdot & \cdot & \chi^{(2)}_{yxy} & \chi^{(2)}_{yyx} \\ \chi^{(2)}_{zxx} & \chi^{(2)}_{zyy} & \cdot & \cdot & \cdot & \cdot & \cdot & \chi^{(2)}_{zxy} & \chi^{(2)}_{zyx} \end{bmatrix} \begin{bmatrix} E_x^2 \\ E_y^2 \\ E_z^2 \\ E_y E_z \\ E_z E_y \\ E_z E_x \\ E_x E_z \\ E_x E_y \\ E_y E_x \end{bmatrix} \tag{22}$$

Fortunately, the large number of tensor components can be reduced by symmetry considerations leading to less independent non vanishing components. For centrosymmetric materials all tensor components are zero, thus $\chi^{(2)} = 0$. This can easily be shown by the principle of Neuman which states that under symmetry operations on the system the sign and the magnitude of physical properties remain unchanged. Under inversion the electric field and the polarization transforms as $\vec{E} \rightarrow -\vec{E}$ and $\vec{P} \rightarrow -\vec{P}$ for centrosymmetric systems (see Figure 4). Therefore

$$-\vec{P}^{(2)} = \chi^{(2)}(-\vec{E})(-\vec{E}) = \chi^{(2)}(\vec{E})(\vec{E}) \tag{23}$$

$$\Rightarrow \vec{P}^{(2)} = -\chi^{(2)}(\vec{E})(\vec{E}) \tag{24}$$

This with Equation 16 is only valid when $\chi^{(2)} = 0$. Thus no second harmonic light is generated by centrosymmetric systems (sys-

---

[14] $\chi^{(2)}$ is a third rank tensor because susceptibility and polarizability connect the product of two field vectors with the polarization vector.

[15] This is the general notation for non-degenerate excitations such as SFG and DFG. For SHG however, a contracted notation is often used, where the nonlinear susceptibility tensor $\chi^{(2)}$ is expressed by a 6×3 tensor and the electric field $\vec{E}\vec{E}$ by a 6 (instead of 9) dimensional vector. For reasons of simplicity however, the more general notation is used in this thesis.

tems with inversion symmetry)[16]. For anharmonic asymmetric potentials, where the property of centrosymmetry is broken, the nonlinear susceptibility is nonzero, and therefore second harmonic generation might occur. Frequency doubling crystals found in lasersystems are an example based on this technique.

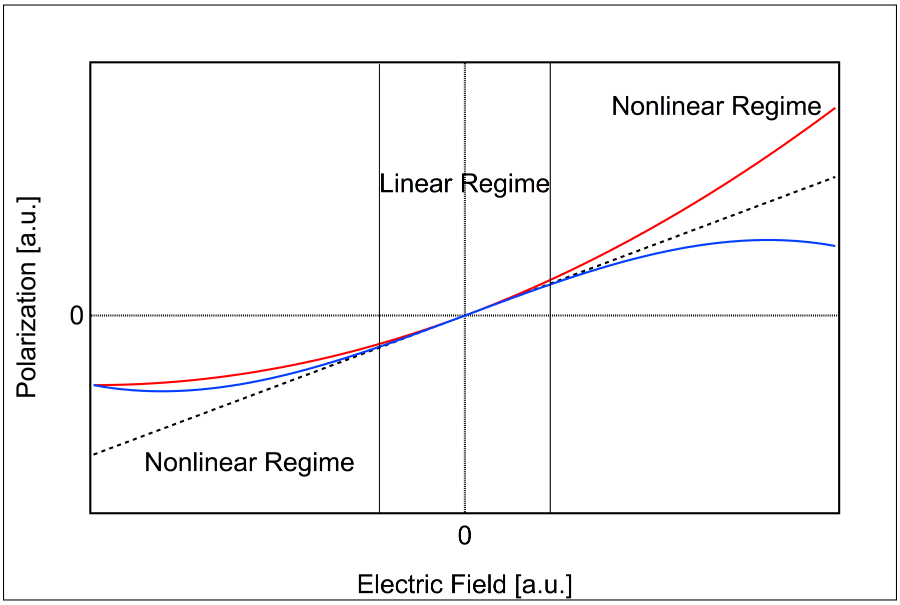

Figure 4: Polarization plotted as a function of the applied electric field for three different potentials. Harmonic potential: dashed black line. Anharmonic centrosymmetric potential: blue line. Anharmonic asymmetric potential: red line. Only an anharmonic asymmetric potential leads to second harmonic generation. It can also be seen that for small electric fields the harmonic approximation is valid [25].

In media with inversion symmetry (such as materials with amorphous structures) no polarization component is induced at twice the fundamental energy. Only in regions where the centrosymmetry is broken can a nonlinear polarization be generated. This is the basic idea of S-SHG spectroscopy. Inside homogeneous bulk media (which are used in this thesis) no nonlinear polarization can be induced and henceforth second harmonic generation occurs exclusively at the surfaces where the symmetry is broken. This fact can be used to achieve great interface or surface sensitivity for centrosymmetric or randomly ordered systems, since at their surfaces centrosymmetry is always broken.

Another aspect of noncentrosymmetry is given in the following. Chirality comes into play here because chiral systems are inherently noncentrosymmetric. Even a random distribution of enantiomerically

---

[16] As shown later, this condition is fulfilled for the substrate of the data presented in this work and is a crucial condition for surface Second-Harmonic-Generation (S-SHG) as well as for Second-Harmonic-Generation Optical-Rotatory-Dispersion (SHG-ORD).

pure chiral molecules will never lead to systems with inversion symmetry. Therefore nonlinear optical processes e.g. "Sum-Frequency-Generation" are possible in solutions (where molecules are randomly distributed) with enantiomerically pure molecules [40, 54][17]. For a noncentrosymmetric system, however, the number of non-vanishing tensor components can be reduced using symmetry considerations (see Section 1.3.1)[18].

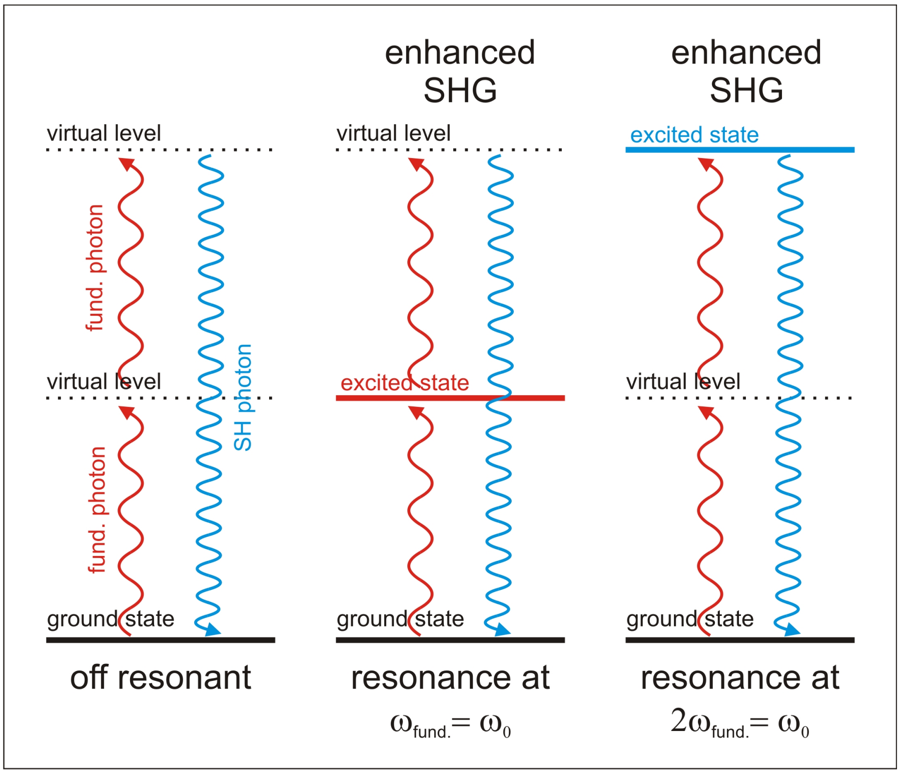

Figure 5: Polarization plotted as a function of the applied electrical field for 3 different potentials [25].

The nonlinear processes were classically described by electric waves so far. Another important aspect can be seen by using a photonic picture of light for the second harmonic generation of a system. In Figure 5 three examples of an SHG-process are shown. The system absorbs two photons with equal energy, and emits one photon with double the energy. For a coherent fundamental excitation the emitted energy (photon) is also coherent, which is advantageous for the subsequent detection (see Section 2.5). Three different possible examples of transitions are drawn. In the first example no excited state matches the photon energy, thus it exhibits two virtual levels. In the second and third transition examples an excited state matches either the fundamental resonant energy or it's double resonant energy.

---

[17] Noncentrosymmetry is no longer a strict requirement for nonlinear processes, if magnetic dipole and electric quadrupole interactions are included.

[18] In reference [41] many examples for different symmetries for the nonlinear susceptibility tensor $\chi^{(2)}$ are shown.

The transition probability of this three photon process is given by the product of the transition probabilities of each single transition. Thus the second and third transitions are consequently enhanced, because an excited state is located at fundamental resonant energy or double resonant energy. However, it is important to note that by detecting the emitted SHG photon it can not unambiguously be told, which excitation scheme is the origin for this emission.

1.2 SURFACE SECOND HARMONIC GENERATION (S-SHG) SPECTROSCOPY

As mentioned before, Second-Harmonic-Generation is only allowed in noncentrosymmetric systems. At surfaces or interfaces centrosymmetry is always broken. For this reason S-SHG is a surface-specific and sensitive technique for interfaces between two centrosymmetric media, such as liquid/liquid, solid/liquid, air/liquid and solid/air interfaces. It allows for the investigation of adsorbates on surfaces with submonolayer sensitivity [55]. Therefore S-SHG is a very powerful tool for the investigation of surfaces or adsorbates on surfaces.

The intensity of S-SHG radiation generated at interfaces between two isotropic media can be described by the following Equation [56, 57, 58, 59]:

$$I(2\omega) = \frac{32\pi^3\omega^2}{c^3}\sec^2(\theta)\left|\hat{E}(2\omega)\cdot\chi^{(2)}\times\hat{E}(\omega)\hat{E}(\omega)\right|^2 I(\omega)^2 \qquad (25)$$

where, θ, is the angle of incidence (see Figure 7) and, $I(\omega)$, the intensity of the exciting field. $\hat{E}(\omega)$ and $\hat{E}(2\omega)$ are the polarization vectors of the incident photons and the emitted photons respectively. The polarization vectors depend on the geometry used and polarization involved[19]. The measured nonlinear intensity, $I(2\omega)$, is therefore also proportional to the angle of incidence:

$$I(2\omega) \sim \sec^2(\theta) \qquad (26)$$

Here, it can already be seen that at an incident angle of 0 degree no second-harmonic-generation occurs. This is an important finding for the data presented later in this work.

1.3 SHG OPTICAL-ROTATORY-DISPERSION SPECTROSCOPY

Magnetic interactions are weaker than electric dipole interactions by a factor given by the fine-structure constant ($\approx \frac{1}{137}$) and are therefore completely neglected in this theoretical description. However, depending on the investigated system, some experiments indicate that

---

[19] The interested reader may refer to these publications: [56, 57, 58, 59].

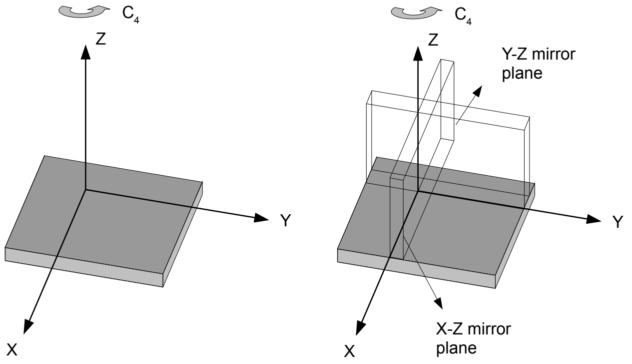

(a) Chiral surface with $C_4(C_\infty)$ symmetry (b) Achiral surface with C_{4v} $(C_{\infty v})$ symmetry

Figure 6: Main symmetry operations for a chiral and an achiral isotropic surface with C_{4v} and C_4 symmetry [40].

magnetic contributions are necessary to accurately explain nonlinear optical activity. In that case irradiating the sample will induce nonlinear polarization and magnetization which both act as a source of second harmonic generation [41, 60, 61, 62]. For increasing field intensities also higher order, e.g. cubic or quadratic contributions were observed [63].

The investigated systems can be well described neglecting magnetic or higher order contributions, therefore a deeper consideration of the theoretical description will not be given in this thesis.

1.3.1 *Chirality in Second-Order Nonlinear Optics (Symmetry Consideration of $\chi^{(2)}$)*

As mentioned previously, the number of non-vanishing tensor components of the susceptibility tensor $\chi^{(2)}$ is directly linked to the symmetry of the sample. As chirality is a symmetry property, one can expect different susceptibility components for chiral and achiral (racemic) surfaces within the electric dipole approximation.

It is useful to consider two symmetries for the theoretical investigation of $\chi^{(2)}$: C_∞ for a chiral isotropic surface with in-plane isotropy, hence the only symmetry operation is an arbitrary rotation about the surface normal, and $C_{\infty,v}$ for an achiral (racemic) isotropic surface with in-plane isotropy. Here the reflection in a plane containing the surface normal is also a symmetry operation [60]. The symmetries can be reduced to C_4 and $C_{4,v}$-symmetries, because a higher order symmetry introduces no further simplification of the susceptibility tensor (see Figure 6).

As shown in detail in reference [40] the number of independent components of the second order susceptibility tensor $\chi^{(2)}$ that describe the second-harmonic-signal, which is generated on a chiral isotropic surface[20], can be reduced to four[21]. An achiral surface can be described by three independent components. Both, chiral and achiral tensor components are shown in Table 1. The tensor components $xyz = -yxz = -yzx = xzy$ are only allowed for chiral isotropic surfaces and are therefore called chiral tensor components, whereas those allowed for both chiral and achiral surfaces, are called achiral tensor components.

CHIRAL C_∞ SYMMETRY
$\chi_1^{(2)} = \chi_{zzz}^{(2)}$
$\chi_2^{(2)} = \chi_{zxx}^{(2)} = \chi_{zyy}^{(2)}$
$\chi_3^{(2)} = \chi_{xxz}^{(2)} = \chi_{yyz}^{(2)} = \chi_{yzy}^{(2)} = \chi_{xzx}^{(2)}$
$\chi_4^{(2)} = \chi_{xyz}^{(2)} = -\chi_{yxz}^{(2)} = -\chi_{yzx}^{(2)} = \chi_{xzy}^{(2)}$
ACHIRAL $C_{\infty,v}$ SYMMETRY
$\chi_1^{(2)} = \chi_{zzz}^{(2)}$
$\chi_2^{(2)} = \chi_{zxx}^{(2)} = \chi_{zyy}^{(2)}$
$\chi_3^{(2)} = \chi_{xxz}^{(2)} = \chi_{yyz}^{(2)} = \chi_{yzy}^{(2)} = \chi_{xzx}^{(2)}$

Table 1: Non vanishing components of the second-order susceptibility tensor $\chi^{(2)}$ neglecting magnetic dipole contributions.

During this work only transmitted SHG light, which was generated at the surface of the sample, was measured. For completeness however, this theoretical description includes both transmission and reflection geometries. The experimental configuration is shown in Figure 7.

A linearly polarized laser beam with frequency ω is shone on a chiral surface with C_∞ symmetry. The symmetry is broken in the z-direction but rotation about the surface normal remains a symmetry operation. For an achiral surface, reflection at a plane through the surface normal is an additional symmetry operation. Second-harmonic light (2ω) is generated at the thin film or surface of the substrate because centrosymmetry is broken. The SHG-light is reflected and transmitted through the sample after which the intensity and polarization are measured[22].

---

[20] This consideration is done within the electric dipole approximation and neglects magnetic and quadruple interactions.

[21] This is done by different symmetry considerations: First, all tensor components, whose signs change under reflection (principle of Neumann) cancel out. This leads to the elimination of 14 components. Two more components cancel out because of permutation symmetry. As the remaining 11 components are not independent, 4 independent components remain.

[22] Analogous theoretical considerations are valid for an experimental setup where the direction of the laser beam is inverted.

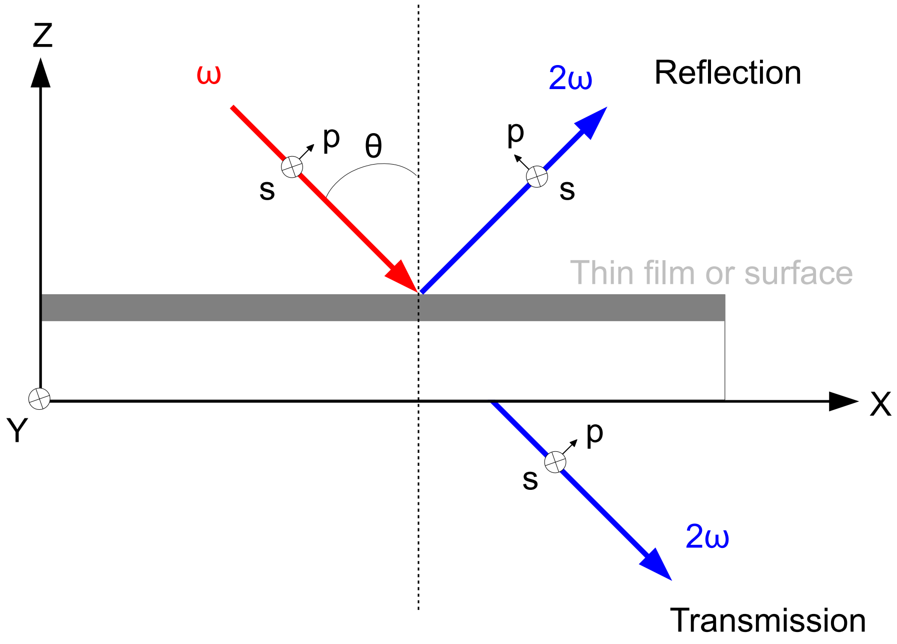

Figure 7: Geometry of second-harmonic generation of a thin film or surface. The thin film or surface is irradiated by fundamental light ω at an angle of incidence θ. SHG light with frequency 2ω is generated at the surface in reflection and transmission direction.

For an isotropic chiral surface, which is invariant to rotations about the z-axis (C_∞ symmetry), and irradiated by p-polarized light ($E_y = 0$) the polarization can be written:

$$\begin{bmatrix} P_x^{(2)} \\ P_y^{(2)} \\ P_z^{(2)} \end{bmatrix} = \begin{bmatrix} 0 & 0 & 0 & \chi_4^{(2)} & \chi_4^{(2)} & \chi_3^{(2)} & \chi_3^{(2)} & 0 & 0 \\ 0 & 0 & 0 & \chi_3^{(2)} & \chi_3^{(2)} & -\chi_4^{(2)} & -\chi_4^{(2)} & 0 & 0 \\ \chi_2^{(2)} & \chi_2^{(2)} & \chi_1^{(2)} & 0 & 0 & 0 & 0 & 0 & 0 \end{bmatrix} \begin{bmatrix} E_x^2 \\ 0 \\ E_z^2 \\ 0 \\ 0 \\ E_z E_x \\ E_x E_z \\ 0 \\ 0 \end{bmatrix} \tag{27}$$

The components can be deduced by comparing Equation 27 with Equation 22. The chiral tensor elements are marked in blue. It can be seen, that for p-polarized incident light and an achiral surface (blue elements $= 0$) the generated SHG signal is completely p-polarized

($P_y^{(2)} = 0$), whereas for chiral molecules (including blue marked tensor elements) the SHG signal has p- and s- components ($P_y^{(2)} \neq 0$). Therefore, a quick test whether a surface is chiral or achiral is to use p-polarized input light and measure s-polarized SHG light. If s-polarized SHG light is measurable, this indicates that the chiral tensor element $\chi^{(2)}_{xyz}$ is measurable and hence the surface is chiral. If only the s-polarized part is measured, only two tensor elements (the chiral tensor element $x^{(2)}_{xyz}$ and the achiral tensor element $\chi^{(2)}_{xxz}$) contribute to the measured SHG-signal (see Equation 27) [64].

The nonlinear polarization, $P^{(2)}(\omega)$, acts as a source of second harmonic generation. One can write the second-harmonic-generated field as [65]:

$$E_i(2\omega) = f_i E_p^2(\omega) + g_i E_i^2(\omega) + h_i E_p(\omega) E_s(\omega) \tag{28}$$

where f_i, g_i and h_i are parameters of a linear combination of the components of $\chi^{(2)}$. These parameters simplify the further theoretical description. For a film or surface with C_∞ symmetry the parameters are given by:

$$\begin{aligned}
f_{Ts}^{Rs} &= \sin\theta(-2\chi_{xyz}^{eee}\cos\theta - 2\chi_{xzx}^{eem} + \chi_{zzz}^{mee}\sin^2\theta) \\
&\quad + \chi_{zxx}^{mee}\cos^2\theta \mp 2\chi_{xxz}^{mee}\cos^2\theta) \\
g_{Ts}^{Rs} &= \sin\theta\,(\chi_{xxz}^{eem} + \chi_{zxx}^{mee}) \\
h_{Ts}^{Rs} &= \sin\theta(2\chi_{xxz}^{eee} - (\chi_{xzy}^{eem} + \chi_{xyz}^{eem})\cos\theta \mp 2\chi_{xyz}^{mee}\cos\theta \\
f_{Tp}^{Rp} &= \sin\theta(\chi_{zzz}^{eee}\sin^2\theta + \chi_{zxx}^{eee}\cos^2\theta \mp 2\chi_{xxz}^{eee}\cos^2\theta) \\
&\quad - \chi_{zxy}^{eem}\cos\theta \pm \chi_{xzy}^{eem}\cos\theta + 2\chi_{xyz}^{mee}\cos\theta \\
g_{Tp}^{Rp} &= \sin\theta(\chi_{zxx}^{eee} - \chi_{zxy}^{eem}\cos\theta \mp \chi_{xyz}^{eem}\cos\theta) \\
h_{Tp}^{Rp} &= \sin\theta(\mp 2\chi_{xyz}^{eee}\cos\theta + (\chi_{zzz}^{eem} - \chi_{zxx}^{eem})\sin^2\theta \\
&\quad \mp (\chi_{xzx}^{eem} + \chi_{xxz}^{eem})\cos^2\theta - 2\chi_{xxz}^{mee})
\end{aligned} \tag{29}$$

where the indices R and T refer to second-harmonic light generated in reflection (R) or transmission (T). The parameters s and p refer to the polarization of the detected signal and θ is the angle of incidence (see Figure 7). The coefficients f_p, g_p and h_s only depend on achiral components, whereas f_s, g_s and h_p only depend on chiral components. A table of chiral and achiral components can be found in literature [41].

1.3.2 *SHG-ORD*

Second-harmonic-generation optical-rotatory-dispersion (SHG-ORD) describes the rotation of the polarization of the emitted S-SHG light in comparison to the polarization of the fundamental excitation light. It can be considered as the nonlinear analogue of linear optical rotation.

An advantage of SHG-ORD (in contrast to SHG-CD) is that it can also occur under non-resonant conditions[23]. It is surface-sensitive, chiral-selective but not constrained to resonant wavelengths. The idea of SHG-ORD is to use linearly polarized fundamental light and measure the polarization of the emitted SHG-light of the surface. Therefore the angle between the (p-polarized) fundamental light and the emitted SHG signal is defined as the rotation angle ϕ. It can also be expressed as the amount of rotation between the polarization of the signal from an enantiomeric pure surface and a racemic mixture (which will be p-polarized for an isotropic surface). The rotation angle, ϕ, can be defined as

$$\tan\phi = R(2\omega) \tag{30}$$

where $R(2\omega)$ is the ratio of the s- and the p-polarized components of the second harmonic generated field:

$$R(2\omega) = \frac{E_s(2\omega)}{E_P(2\omega)} = \frac{f_s E_p^2(\omega) + g_s E_s^2(\omega) + h_s E_p(\omega) E_s(\omega)}{f_p E_p^2(\omega) + g_p E_s^2(\omega) + h_p E_p(\omega) E_s(\omega)} \tag{31}$$

using p-polarized fundamental light, the expression is simplified to (compare Equation 27 and 29):

$$R(2\omega) = \frac{f_s}{f_p} \tag{32}$$

and the rotation angle, ϕ, is given in transmission mode by:

$$\begin{aligned}
\Rightarrow \phi &= \tan^{-1}\left(\frac{f_s}{f_p}\right) \\
&= \tan^{-1}\left(\frac{-\sin\theta(-2\chi_{xyz}^{eee}\cos\theta)}{\sin\theta(\chi_{zzz}^{eee}\sin^2\theta + \chi_{zxx}^{eee}\cos^2\theta + 2\chi_{xxz}^{eee}\cos^2\theta)}\right) \\
&= \tan^{-1}\left(\frac{2\chi_{xyz}^{eee}\cos\theta}{\chi_{zzz}\sin^2\theta + (\chi_{zxx}^{eee} + 2\chi_{xxz}^{eee})\cos^2\theta}\right)
\end{aligned} \tag{33}$$

It can be seen that f_s reverses sign between two enantiomers because it includes the chiral component χ_{xyz}^{eee}. f_p, in contrast, does not change between enantiomers because it includes only achiral components $(\chi_{zzz}^{eee}, \chi_{zxx}^{eee}, \chi_{xxz}^{eee})$. As a consequence the rotation angle, ϕ, changes sign between two different enantiomers of a chiral molecule. Therefore, different enantiomers of chiral molecules can be distinguished by the sign of the SHG-ORD rotation angle. The magnitude of the

---

[23] In SHG-CD a circular polarized fundamental beam is used and the intensity of p-polarized or s-polarized SHG light is detected. No light will be detected for an achiral surface. However, the lack of an SHG-CD-effect cannot be used to conclude that the material is achiral. Because SHG-CD is a resonance technique, it can be useful to probe the SHG-CD response as a function of the SH wavelength to gain information about the probed species [40].

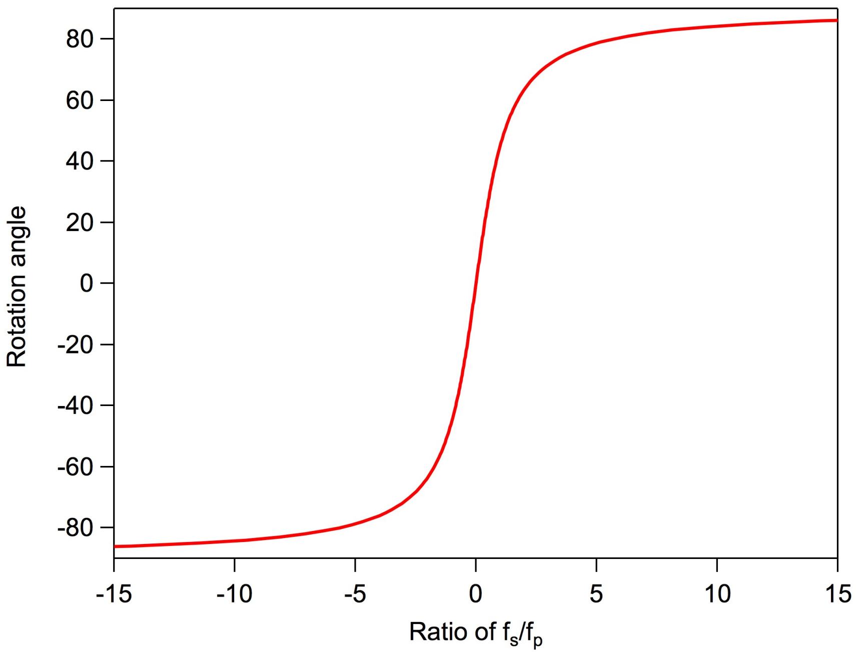

Figure 8: Rotation angle ϕ as a function of the ratio between the chiral and achiral susceptibility components f_s and f_p. It is limited to $\phi = \pm 90°$.

SHG-ORD effect depends on the ratio between the components f_s and f_p as shown in Figure 8. It can be seen that the rotation angle is limited to $\phi = \pm 90°$ and that for $\frac{f_S}{f_p} = 0$ no rotation occurs. The rotation angle, ϕ, will be large when the chiral component $\chi^{(2)}_{xyz}$ given by f_s is large compared to the achiral components given by f_p.

In conclusion, SHG-ORD is an outstanding spectroscopic method for the chiral-sensitive investigation of adsorbates on surfaces. It is hence a perfect tool for the chiral-selective investigation of adsorbates under UHV conditions undertaken in this work. The differences between linear and nonlinear ORD are depicted in Table 2.

PROPERTY	LINEAR ORD	NONLINEAR ORD
path-length	Increase of rotation angle	no dependency on rotation angle
light intensity	no influence on rotation angle	no influence on rotation angle
elect. or magn. contributions	$\chi_m^{(1)}$ needed	$\chi_e^{(2)}$ sufficient
intensity	1	up to 10^6

Table 2: Differences between linear and nonlinear ORD.

1.4 $2,2'$-DIHYDROXY-$1,1'$BINAPHTHYL (BINOL)

$2,2'$-dihydroxy-$1,1'$binaphthyl (Binol) is one of the most experimentally studied chiral molecules in nonlinear optics. The first nonlinear chiral effects were measured with Binol by Hicks and coworkers [66, 67, 64]. By spectroscopic investigation of enantiomerically pure Binol molecules at fused silica and liquid interfaces they showed that nonlinear effects such as second-harmonic-generation-circular dichroism (SHG-CD), as well as second-harmonic-generation optical-rotatory-dispersion (SHG-ORD) are very sensitive tools to probe chiral molecules on surfaces. Using Binol as a reference system they could demonstrate that these nonlinear effects are up to 6 orders of magnitude larger than their linear analogue [68]. Through good agreement between their calculations and observed experimental data they concluded that the observed nonlinear effects are predominantly electric dipole allowed [64].

Two classical models were used to calculate S-SHG signals for different molecules; a "one-electron mechanism" and a "coupled oscillator" mechanism. The first describes an asymmetric environment in a chromophore where the electric- and the magnetic transitions are mixed. The second describes two separate chromophores where the electric dipole allowed transitions are asymmetrically coupled [63]. Hache et al. showed that for the first model the dominant chiral susceptibilities have a magnetic origin whereas for the second model the electric contributions dominate [50]. Because Binol shows a coupled oscillator chirality it is sufficient to use only electric dipole allowed contributions and neglect magnetic transitions for the theoretical description.

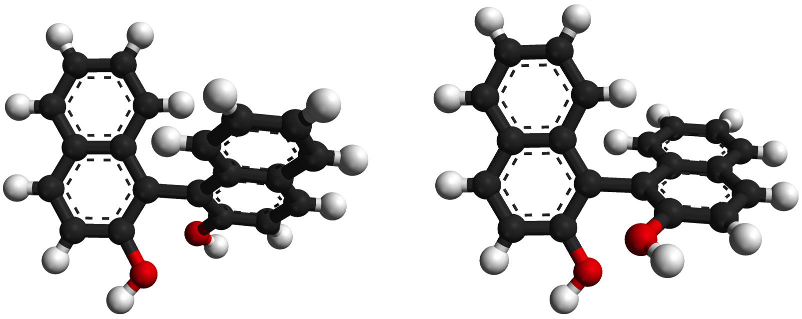
(a) S-Binol. (b) R-Binol.

Figure 9: Drawing of both enantiomers of the Binol molecule [69].

1.4.1 *Optical Properties of Binol*

In the following the aforementioned more general description of the SHG-ORD effect is referred to the investigated system of this thesis. For p-polarized input light and by considering only electric dipole allowed transitions the parameters in Equation 29 reduce for the transmission mode to:

$$\begin{aligned} f_s &= \sin\theta(2\chi_{xyz}\cos\theta) \\ g_s &= 0 \\ h_s &= \sin\theta(2\chi_{xxz}) \\ f_p &= \sin\theta(\chi_{zzz}\sin^2\theta + \chi_{zxx}\cos^2\theta + 2\chi_{xxz}\cos^2\theta) \\ g_p &= \sin\theta\chi_{zxx} \\ h_p &= -\sin\theta(+2\chi_{xyz}\cos\theta) \end{aligned} \tag{34}$$

For p-polarized incident light $E_p(2\omega)$ and $E_s(2\omega)$ are therefore given by (see Equation 28):

$$\begin{aligned} E_p(2\omega) &= f_p E_p^2(\omega) \\ &= \sin\theta(\chi_{zzz}\sin^2\theta + \chi_{zxx}\cos^2\theta + 2\chi_{xxz}\cos^2\theta)E_p^2(\omega) \\ E_s(2\omega) &= f_s E_s^2(\omega) = \sin\theta(2\chi_{xyz}\cos\theta)E_s^2(\omega) \end{aligned} \tag{35}$$

and the rotation angle, ϕ, is given by:

$$\phi = \tan^{-1}\left(\frac{f_s}{f_p}\right) = \tan^{-1}\left(\frac{2\chi_{xyz}\cos\theta}{\chi_{zzz}\sin^2\theta + (\chi_{zxx} + 2\chi_{xxz})\cos^2\theta}\right) \tag{36}$$

$$\phi = \tan^{-1}\left(\frac{2\chi_{xyz}\cos\theta}{\chi_{zzz}\sin^2\theta + (\chi_{zxx} + 2\chi_{xxz})\cos^2\theta}\right) \tag{37}$$

$$\phi = \tan^{-1}\left(\frac{2\chi_4\cos\theta}{\chi_1\sin^2\theta + (\chi_2 + 2\chi_3)\cos^2\theta}\right) \tag{38}$$

As described previously the chirality of the sample is given by the chiral susceptibility component $\chi_4 = \chi_{xyz}$. The other components are referred to as achiral. Therefore the ratio $\frac{f_s}{f_p}$ of chiral to achiral tensor components can be calculated by knowing the rotation angle of the investigated system.

1.4.2 *Symmetry Considerations of Supported Binol*

In the experimental data presented in this work different quantities of enantiomeric pure Binol molecules were evaporated onto a borosilicate substrate. Since the rotation angle depends on the orientation of the molecules on the surface a short theoretical background of the orientation of the molecules is given here. The macroscopic response of the given surface depends on the macroscopic nonlinear susceptibility $\chi^{(2)}$. However, looking at symmetries, the microscopic nonlinear polarizability (also referred to as the hyperpolarizability) $\alpha^{(2)}$ is of interest, because it relates to the properties of the individual molecule. For Binol the symmetry allowed $\alpha^{(2)}$ elements are given by [64]:

$$\alpha^{(2)} = \begin{bmatrix} 0 & 0 & 0 & \alpha^{(2)}_{xyz} & \alpha^{(2)}_{xzy} & \alpha^{(2)}_{xzx} & \alpha^{(2)}_{xxz} & 0 & 0 \\ 0 & 0 & 0 & \alpha^{(2)}_{yyz} & \alpha^{(2)}_{yzy} & \alpha^{(2)}_{yzx} & \alpha^{(2)}_{yxz} & 0 & 0 \\ \alpha^{(2)}_{zxx} & \alpha^{(2)}_{zyy} & \alpha^{(2)}_{zzz} & 0 & 0 & 0 & 0 & \alpha^{(2)}_{zxy} & \alpha^{(2)}_{zyx} \end{bmatrix} \tag{39}$$

Byers et al. showed that chirality on a molecular level is necessary to produce chiral $\chi^{(2)}$ elements on isotropic surfaces. The exact relationship between $\alpha^{(2)}$ and $\chi^{(2)}$ requires knowledge of the orientational distribution of the surface molecules. For surfaces consisting of non-interacting molecules (local field corrections are neglected) the macroscopic $\chi^{(2)}$ tensor is given by an averaged sum of the molecular hyperpolarizability tensor elements of $\alpha^{(2)}$:

$$\chi^{(2)}_{xyz} = N_s \sum_{abc} \langle T_{xa} T_{yb} T_{zc} \rangle \, \alpha^{(2)}_{abc} \tag{40}$$

Here, N_s is the number-density of surface molecules and T_{ia} represents the projection of the lab frame coordinates x, y, z onto the molecular coordinates a, b, c. The brackets represent an average over all orientations of the surface molecules. In order to find $T_{xa} T_{yb} T_{zc}$ the knowledgment of both the nonlinear susceptibility, $\chi^{(2)}_{ijk}$, and the nonlinear polarizability, $\alpha^{(2)}$, is required. $\chi^{(2)}_{ijk}$ is often easy to measure by the surface SHG, whereas $\alpha^{(2)}$ is usually difficult to obtain. Therefore, it is difficult to determine the average orientation of the molecules on the surface [43, 67, 64, 59]. The exact relation between the molecular hyperpolarizability $\alpha^{(2)}$ and the macroscopic nonlinear susceptibility $\chi^{(2)}$ requires the knowledge of the orientation distribution of the surface molecules (see Equation 40). Hence, the macroscopic susceptibil-

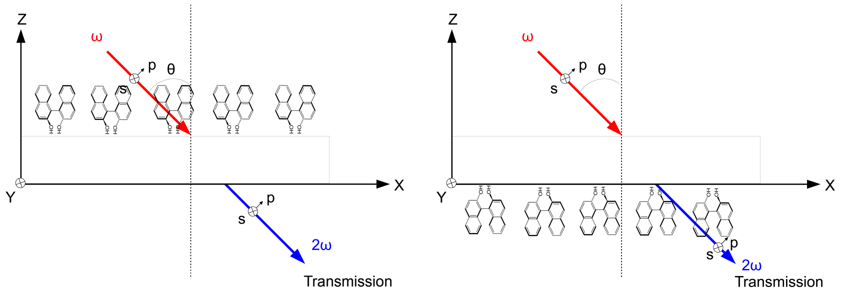

(a) Supported s-Binol. Transmission mode A.

(b) Supported s-Binol. Transmission mode B.

Figure 10: Different transmission modi of s-Binol on substrate. The molecules are presumed to be oriented with their hydroxyl groups towards the surface.

ity tensor, $\chi^{(2)}$, changes whenever the orientation distribution of the molecules change.

In the presented work, two different geometric alignments were used (see Figure 10). In order to understand the behavior of SHG-ORD effect and the sign of the rotation angle a deeper look into the behavior of the nonlinear susceptibility of $\chi^{(2)}$ for different orientations of molecules on surfaces in respect to the propagating field is useful. As shown before (see Equation 40) the tensor elements of the nonlinear susceptibility tensor, $\chi^{(2)}$, are proportional to the hyperpolarizability tensor $\alpha^{(2)}$. It can be shown that inverting the molecules by a C_{2v} rotation around the x-axis, which is similar to switching from transmission mode A to transmission mode B (see Figure 10), the achiral tensor elements of $\chi_1^{(2)}, \chi_2^{(2)}, \chi_3^{(2)}$ change sign, whereas the chiral tensor element $\chi_4^{(2)}$ does not [66]. This can be clarified by examination of the tensor elements. The transformation of the coordinates and chiral tensor elements for the change of the transmission mode is subsumed in the following:

$$\begin{aligned} x &\rightarrow x \\ y &\rightarrow -y \\ z &\rightarrow -z \end{aligned} \tag{41}$$

$$\begin{aligned} \chi_{xyz}^{(2)} &\rightarrow \chi_{xyz}^{(2)} \\ \chi_{zzz}^{(2)} &\rightarrow -\chi_{zzz}^{(2)} \\ \chi_{zxx}^{(2)} &\rightarrow -\chi_{zxx}^{(2)} \\ \chi_{xxz}^{(2)} &\rightarrow -\chi_{xxz}^{(2)} \end{aligned} \tag{42}$$

Changing the chirality and thus the enantiomer of the molecule for the same transmission mode only effects the chiral tensor element (as mentioned previously) and changes its sign ($\chi_4^{(2)} \rightarrow -\chi_4^{(2)}$).

Thus, it is important to note that in an SHG-ORD experiment the rotation angle, ϕ, changes sign whenever the chirality or the absolute orientation of the surface molecules (thus the transmission mode) changes [66]. This is always true of samples with in-plane isotropy, independent of the orientation of the molecules.

In this theoretical description it was shown, that the SHG-ORD effect depends on the nonlinear susceptibility tensor elements of a given system. This macroscopic response, however, depends on the microscopic hyperpolarizability of the molecules and their orientation on the surface.

These are important findings for the experimental results presented later. Parameters, which are linear combinations of the susceptibility tensor elements, were introduced in order to simplify the theoretical description. It was shown that the value of the ORD-SHG effect depends on the ratio of the achiral to chiral parameters. The Binol molecule was introduced and shown to be a perfect probe molecule for this effect, because it's strong nonlinear chiral response can completely be described within the electric dipole approximation neglecting magnetic contributions.

1.5 METAL CLUSTERS

In the following section the optical properties of metal nanoparticles and clusters are discussed[24]. The theoretical description of this chapter follows the "top-down" approach; from pure bulk metals to size-selected clusters. First, a basic theoretical description of bulk metal materials is derived. The dielectric function is introduced within the "Drude Model" and extended by inter-band transitions. Then, small metal nanoparticles are introduced with a special focus on plasmon oscillations, which are essential for metal nanoparticles in the size regime from 10 nm to approximately 2 nm. It is shown that especially for small nanoparticles their optical properties differ significantly from those of their corresponding bulk materials. Mie theory is introduced and shown to be a good theoretical description for light and particle interactions[25]. However, only a short summary is given, leading to the important insights used for further theoretical description. The limits of Mie Theory are shown and a theoretical description for very small clusters (n = 3 - 100 atoms) is derived and dis-

---

[24] Clusters are often defined as particles composed of a certain number N of atoms between $3 \leq N \lesssim 1000$. In this thesis a composition of metal atoms forming a bigger particle is called "cluster", whenever the exact size, hence the number of associated atoms is known. Particles where this is not the case (e.g. when their size is described by their mean radius) are referred to as "nanoparticles".

[25] Good theoretical descriptions of optical properties of supported metal nanoparticles and clusters can be found in ref. [25, 70, 71, 72]. However, the best summary of the optical properties of metal clusters, both theoretically and experimentally, is given in [28]. Most of this chapter is based on these references.

cussed. In this "quantum size regime" the aforementioned classical approach has to be modified by quantum effects, which are essential for these cluster sizes. At the end cluster-cluster and cluster-substrate interactions are introduced and discussed. Both quantum effects and cluster-substrate, as well as cluster-cluster interactions are phenomena which are important for the interpretation of the data presented in this work.

1.5.1 *Optical Properties of Metals*

The dielectric function[26] $\epsilon(\omega)$ of bulk material is a measure of how an electric field affects a dielectric medium and vice versa. It is related to the linear susceptibility $\chi(\omega)$ (see Section 1.1.1) by[27]:

$$\epsilon(\omega) = 1 + \chi(\omega) \tag{43}$$

For free-electron metals[28] $\epsilon(\omega)$ is mainly given by transitions within the conduction band. For other metals, however, significant interband transitions might occur, from lower lying bands into the conduction band, as well as from the conduction band into higher unoccupied levels. Noble metals for example show both types of transitions.

1.5.2 *Drude-Lorentz-Sommerfeld Model*

The Drude-Lorentz-Sommerfeld[29] model is a good approximation and simple classical approach for the optical properties of free electron metals. It assumes the conducting electrons to act in phase upon a perturbation (i.e. coherent electromagnetic field), without any local field corrections and other restoring forces. The response of the free electron is given by the susceptibility of the solution for an harmonic oscillator (see Section 1.1.1):

$$\chi^{(1)}(\omega) = \frac{\omega_p^2}{\omega_0^2 - 2i\gamma\omega - w^2} \tag{44}$$

Here, ω_p is the material dependent "plasma frequency"[30], which is based on the number density of conduction electrons [38]:

---

[26] The dielectric function is often referred to as "permittivity".

[27] In the following the dielectric function is mainly used (instead of the linear susceptibility) because it simplifies the theoretical description to some extent.

[28] In free electron metals, such as alkali metals, magnesium, aluminum, and to some extent noble metals, most of the electronic and optical properties are due to the conduction electrons alone. These metals have completely filled valence bands and partially filled conduction bands [28].

[29] Named after Paul Drude [1863 – 1906], Hendrik Antoon Lorentz [1853 – 1928] and Arnold Sommerfeld [1868 – 1951]. In 1900 it was introduced by Paul Drude [73] and extended in 1905 by Hendrik Antoon Lorentz and in 1933 by Arnold Sommerfeld by the results of the quantum theory.

[30] Often called "Drude plasma frequency".

$$\omega_p = \sqrt{\frac{Ne^2}{\epsilon_0 m_e}} \tag{45}$$

where, N, is the number of free electrons per unit volume, e the electron charge, ϵ_0 the dielectric constant[31] and, m_e, the mass of the electron. The "plasma oscillation" can be understood as a Coulomb-force driven rapid oscillation (which followed a displacement) of the electron density in conducting media, e.g in plasmas or metals. It only depends on physical constants as well as on the electron density and is henceforth a material property. The damping constant, γ_{bulk}, can be related to the Fermi velocity, v_F[32], and the mean free path, l[33], by [28]:

$$\gamma_{bulk} = \frac{v_F}{l} \tag{46}$$

The optical response of a collection of free electrons can be obtained from the harmonic oscillator (see Equation 4) by simply setting the spring constant k to zero [72]. With Equation 43 the dielectric function for a system of N free electrons is then given by

$$\epsilon(\omega) = 1 - \frac{\omega_p^2}{\omega^2 + 2i\gamma\omega} \tag{47}$$

This is the Drude model of bulk metals. The real and imaginary part of the dielectric function, describing polarization and the energy dissipation respectively, are given by:

$$\epsilon'(\omega) = 1 - \frac{\omega_p^2}{\omega^2 + 4\gamma^2} \tag{48}$$

$$\epsilon''(\omega) = \frac{2\omega_p^2\gamma}{\omega(\omega^2 + 4\gamma^2)} \tag{49}$$

As described previously, only the free conduction electrons are described within this model. All other electrons (core electrons) are neglected, but might also contribute to the dielectric function. It can be shown that for silver the calculated real part of the dielectric function matches well for small photon energies with measured data, but deviates for larger energies. The imaginary part of the calculated Drude function differs strongly from the measured data. It holds for smaller energies and converges to zero, whereas the measured data show a strong increase to higher values at about $3,8$ eV. This increase can be attributed to inter-band transitions which are not covered by the Drude model.

---

[31] Often referred to as "permittivity of free space"

[32] The Fermi velocity is the velocity that corresponds to a kinetic energy which equals the Fermi energy.

[33] The mean free path is the average distance for moving particles before collision occurs.

A common way to solve this failing of the Drude model for certain metals is to introduce a coupling to possible inter-band transitions by adding the complex term $\chi^{IB}(\omega) = \chi_1^{IB} + i\chi_2^{IB}$ to the dielectric function [74, 28]. The overall dielectric function incorporating all optical material properties is then given by:

$$\epsilon(\omega) = 1 + \chi^{IB}(\omega) + \chi^{D}(\omega) \tag{50}$$

Here $\chi^{D}(\omega)$ is the "Drude" susceptibility used before. Then the real and imaginary part of the overall dielectric function are given by:

$$\epsilon'(\omega) = 1 - \frac{\omega_p^2}{\omega^2 + 4\gamma^2} + \chi_1^{IB}(\omega) \tag{51}$$

$$\epsilon''(\omega) = \frac{2\omega_p^2\gamma}{\omega(\omega^2 + 4\gamma^2)} + \chi_2^{IB}(\omega) \tag{52}$$

This overall dielectric function was measured and calculated by different groups and turned out to be a good approach for noble metals [75, 76]. Especially the dielectric function of silver exhibits a superposition of a free electron behavior and a bound electron component.

1.5.3 *Plasmon Oscillation*

Optical properties of nanoparticles and clusters can differ significantly from those of their corresponding bulk materials. The positive charges inside the particle are assumed to be immobile whereas the electrons are allowed to move or oscillate under the influence of an external electric field. However, they are no longer free (in contrast to bulk materials) when hitting the particle surface. Here they are backscattered after penetrating into the surface potential barrier by a restoring coulomb force. Because of their high density and interaction all conduction electrons within the particle act collectively when experiencing an incident electric field. The restoring forces lead to the typical excitation of collective motion, called the plasma oscillation shown in Figure 11 [70].

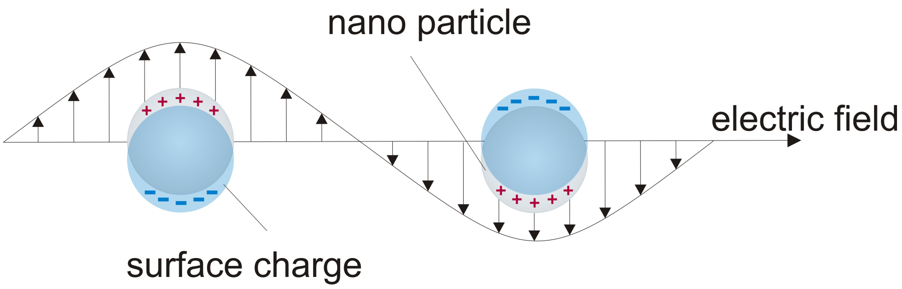

Figure 11: Excited plasmon oscillations by an external varying electric field [77].

1.5.3.1 *Classical Mie Theory: Nanoparticles*

A theoretical approach for the interaction of light with small particles is given in the following description.

The first general solution for the absorption and scattering of light at spherical particles which are embedded in a homogeneous surroundings, was presented by Gustav Mie in 1908 [78]. He solved the Maxwell equations for spherical particles with appropriate boundary conditions for a given dielectric function[34]. Although a completely classical approach, Mie's theory is even today a common model for these specific resonances of nanoparticles [70]. It's importance can not be underestimated. However, even being an exact solution of the Maxwell equations (within it's boundary conditions chosen by Mie) it does not apply for all different effects found in nature[35]. In the following a solution of Mie's theory is presented and applied to silver nanoparticles. Size effects and deviations are introduced and discussed. The theoretical description is valid for particle sizes within the quasi static regime where phase retardation effects and higher multipoles can be neglected. This critical size is approximately ≤ 15 nm for Ag particles [70] and therefore by far fulfilled for clusters of interest in this thesis. Although Mie's theory involves only spherical particles with homogneous surroundings a big advantage is the possibility to expand it's results by introducing a phenomenological dielectric function $\epsilon(\omega, R)$ which considers different effects, such as "spill-out" or intrinsic effects, particle-substrate or particle-particle interactions. These may be taken from experiment [75] or theory.

The dielectric function $\epsilon(\omega, R)$ is the quantity that determines the position and the shape of the recorded spectrum and varies as a function of particle size. For even smaller metal clusters where collective resonances as well as single electron excitations may occur, quantum mechanical methods have to be applied [28].

The wide applicability of Mie theory for metal nanoparticles nowadays is actually based on these phenomenological expansions. Within Mie theory the extinction cross section of a spherical particle in the quasi static regime (R $\ll \lambda$) is given by [28]:

$$\sigma_{ext} = 9\frac{\omega}{c_0}\epsilon_m^{\frac{3}{2}} V_0 \frac{\epsilon''(\omega)}{[\epsilon'(\omega) + 2\epsilon_m]^2 + \epsilon''(\omega)^2} \qquad (53)$$

Here, $V_0 = \left(\frac{4\pi}{3}\right) R^3$ denotes the particles volume. $\epsilon'(\omega)$ and $\epsilon''(\omega)$ are the real- and imaginary parts of the dielectric function respectively, and ϵ_m is the dielectric function of the surrounding medium[36]. In this size region scattering processes can be neglected and therefore the extinction cross section equals the absorption cross section

---

[34] For a more detailed description refer to ref. [28].

[35] A good summary of the limitations of Mie theory can be found in [70].

[36] In this size regime scattering processes and higher multipolar contributions (e.g. quadrupole extinction and scattering) are strongly suppressed.

($\sigma_{ext} = \sigma_{absorb}$) [72]. This simplifies the interpretation of the measured spectra to a great extent. It can easily be seen, that the cross section (Equation 53) is large whenever the denominator has a minimum. This condition is fulfilled for

$$\epsilon'(\omega) = -2\epsilon_m$$

providing that $\epsilon''(\omega)$ is small or does not vary much in the vicinity of the resonance. The frequency where this condition is fulfilled is called "Fröhlich frequency", ω_F, and depends on the surrounding medium[37]. The peak position and width of the Mie resonance is determined by $\epsilon'(\omega)$. However, it may easily be damped away if $\epsilon''(\omega)$ is sufficiently large, which is often the case. Actually only a few materials such as alkalis and noble metals as well as aluminum exhibit sharp Mie-resonances.

1.5.3.2 *Silver*

Ag shows strong deviations from free electron behavior which is e.g. observed for alkalis. The contribution χ'_{IB} of the inter-band transition from the 4d to the 5s band has a significant influence on the energies of the plasmons. The Drude-Plasmon (volume plasmon) shifts from $9,2$ eV to ca. $3,9$ eV when considering inter-band transitions. The associated Mie resonance (surface plasmon) shifts from the free electron value of ca. $5,6$ eV to $3,5$ eV. The Mie resonance is therefore influenced by both the d- and the conduction electrons [28]. The surface plasmon is shifted beyond the inter-band transition edge of $\sim 3,9$ eV. Below this edge $\epsilon''(\omega)$ is small enough to enable a sharp resonance peak. Other noble metals exhibit different behavior[38]. Taking the experimentally derived dielectric functions of Au, Ag and Co one can calculate the Mie-absorption spectra of these metals (via Equation 53). The results are depicted in Figure 12.

Due to the small $\epsilon''(\omega)$ within the respective spectral region, silver is the only noble metal with a well defined surface plasmon in vacuum ($\epsilon_{vacuum} = 1$)[39]. Therefore it is a perfect noble metal for spectroscopic investigations where the surrounding medium and henceforth ϵ_m does not differ significantly from vacuum.

1.5.3.3 *Size Effects*

The above mentioned approaches are in good agreement with experimental data for particles with diameters above 10 nm. However, for

---

[37] For supported clusters often an averaged effective dielectric function with $1 \leq \epsilon_m \leq \epsilon_{support}$ is taken to account for possible substrate effects. It therefore lies between the vacuum value of 1 and the support value and serves as a good approximation [79, 80, 81, 25, 82].

[38] See ref. [25] for a plot of the imaginary parts of the dielectric function for Ag, Au and Co with its associated Fröhlich frequencies.

[39] Only Al, Hg or Mg show similar pronounced surface plasmons.

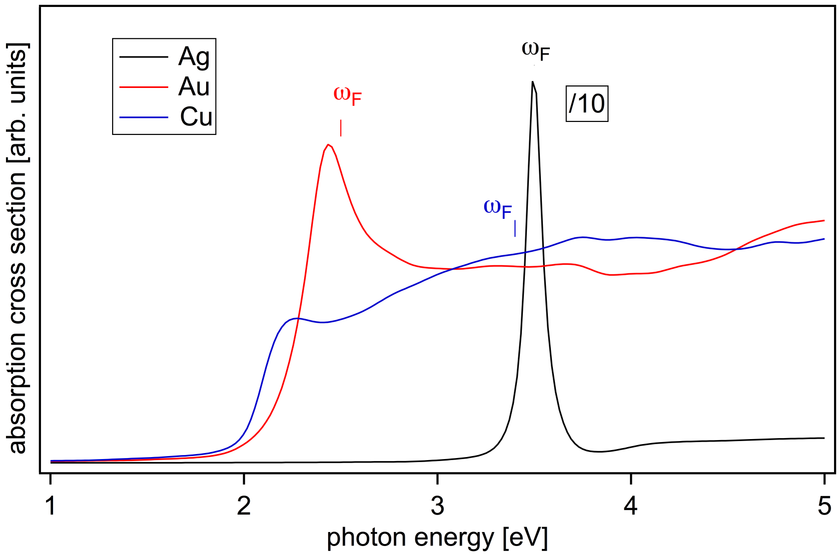

Figure 12: Calculated Mie-absorption spectra of Au, Ag and Co for vacuum ($\epsilon_m = 1$). The Ag spectrum is scaled by $\frac{1}{10}$ with respect to the other spectra [25].

particles of smaller diameter significant deviations occur. Using bulk optical constants for this small size regime, however, is not applicable any more. The dielectric functions for clusters with $R \leq 10$ nm are size dependent $\epsilon(\omega, R)$[40]. Different effects occur for this size regime.

As described previously (see Section 1.5.2) the damping constant, γ (given by interactions with phonons, electrons, impurities and lattice defects) can be expressed by the mean free path, l, and the Fermi velocity, v_F:

$$\gamma_{bulk} = \frac{v_F}{l} \tag{54}$$

For nanoparticles where $R \leq l$ scattering processes may change[41]. For nanoparticles which consist of only a few hundred atoms, increased surface interactions will cause the damping constant, γ, to increase due to the growing number of electron collisions. A common way to account for this change is to introduce an additional term to the damping constant [38]:

$$\gamma(R) = \gamma_{bulk} + \frac{A_{size} v_F}{R} \tag{55}$$

where R is the particle radius and v_F the Fermi velocity (ca. $1,4 \cdot 10^6 \frac{m}{s}$ in silver [83]). The universal $\frac{1}{R}$ dependency reflects the ratio of surface scattering probability and the number of electrons[42]. Thus the surface

---

[40] Often denoted as intrinsic size effects.

[41] The mean free path of silver at room temperature is $l_{Ag} = 52$ nm.

[42] The surface scattering probability is proportional to $4\pi R^2$; the number of electrons proportional to $\frac{4\pi}{3} R^3$. The ratio of both is given by $\frac{1}{R}$.

collision frequency increases with decreasing particle size. The value A is a measure of the dephasing effectiveness of single collisions [70]. It is a fitting constant based on the experimental data in the order of 1 [84]. Considering the size dependent effect of the damping constant the dielectric function for small nanoparticles is is given by [28]:

$$\begin{aligned}\epsilon(\omega, R) = \quad \epsilon_{bulk}(\omega) \quad & +\omega_p^2 \left(\frac{1}{\omega^2 + \gamma_{bulk}^2} - \frac{1}{\omega^2 + \gamma^2(R)} \right) \\ & +i\frac{\omega_p^2}{\omega} \left(\frac{\gamma(R)}{\omega^2 + \gamma^2(R)} - \frac{\gamma_{bulk}}{\omega^2 + \gamma_{bulk}^2} \right) \qquad (56)\end{aligned}$$

This equation can be used to compute optical absorption spectra of very small particles with diameters of 10 nm to 2 nm. The decreased mean path leads to a broadening of the peak width and to a lowering of the peak height of the surface plasmon absorption [72][43]. However, it is important to note that the energy of the resonance maximum is virtually not affected for this size regime using this approach (see Section 1.5.3.4).

1.5.3.4 *Chemical Interface Damping, "spill-out"*

The boundary conditions within the Mie theory, that were introduced previously are usually expressed by electron charge density, which drops from a nonzero value inside the metal to zero outside. However, quantum mechanical calculations show that the change in electron density is not abrupt but takes place over several nanometer [85]. This so called "spill-out" effect can be regarded as a direct consequence of the wave nature of the electron. The influence of the "spill-out" effect obviously increases with decreasing cluster size.

Up to now the optical properties of nanoparticles were derived for free clusters in a homogeneous surrounding without other influences. However, for the results shown in this thesis, other possible influences such as chemical surroundings (adsorbates) and support materials are of great interest. They may lead to additional damping mechanisms and hence affect the optical spectra. Many experiments have indeed shown that these effects might be large. The occupied cluster states might not match the electronic states of the surrounding, which is usually the case for clusters in transparent, dielectric and chemically inert matrices [28].

If occupied states are close to, or coincide in energy with electronic states of the surrounding (e.g. metal clusters in metal matrices) the conduction electrons are transmitted through the interface. This effect is called "chemical interface damping" [86] and leads to a decrease or a complete vanishing of the plasmon. In order to account for this

---

[43] Calculations and plots for different Ag cluster sizes can be found in [25, 28].

effect the A parameter (see Equation 55) is added by an interface contribution $A_{interface}$ [87]:

$$\gamma(R) = \gamma_{bulk} + \left(A_{size} + A_{interface}\right) \frac{v_F}{R} \tag{57}$$

This approach leads to good agreement between theory and observed spectra for clusters in matrices[44]. A further big advantage is the possibility to extend the theory towards metal clusters on surfaces. Here, the $A_{interface}$ parameter is modified or weighted by the ratio between the contact area of the cluster with the substrate and the whole cluster surface. This approach was e.g. chosen previously for supported silver clusters [25, 82] and led to a deeper understanding of the investigated samples.

The aforementioned theoretical description and modification of the damping factor $\gamma(R)$ influences the FWHM, but only slightly the plasmon peak position. It only provides qualitative arguments for understanding the Mie plasmon behavior of small nanoparticles. In fact despite experimental results increasing $\gamma(R)$ leads to a slight red shift of the plasmon resonance with decreasing cluster size [28, 38].

However, distinct blue shifts of the plasmon resonance with decreasing particle size (cluster and nanoparticle) were measured by different groups: Charle et al. measured silver clusters with a mean diameter between $1,5$ nm and 10 nm embedded in different matrices [88]. A qualitative analysis of their spectra revealed that the peak position $\hbar\omega$ of the plasmon resonance and the full width half maximum Γ of the Mie plasmon may be described qualitivley by the same type of formula:

$$\hbar\omega(D) = \hbar\omega_\infty + \frac{a}{D} \tag{58}$$

$$\Gamma(D) = \Gamma_\infty + \frac{b}{D} \tag{59}$$

For Ag clusters embedded in Ar matrices they found values of $a = 0,58$ eVnm. Thus, this $1/D$ behavior not only matches the FWHM but is also found for the blue shift of the resonance position with decreasing particle size. In fact, this qualitative behavior is the reason for the FWHM and peak resonances of clusters and nanoparticles often being plotted as a function of the inverse particle diameter $\frac{1}{D}$[45].

Nilius et al investigated oxide supported silver nanoparticles by means of photon emission spectra stimulated by electron injection from the tip of a scanning tunneling microscope and obtained an a-factor of $a = 0,54$ eVnm [39] (see Section 4.2.2).

---

[44] The $A_{interface}$ parameter is in the range of ≈ 0 eV nm (e.g. Ne matrix) and $\approx 0,65$ eV nm (e.g SiO2 matrix) [86].

[45] This method of plotting has also the advantage that the complete size spectrum, from molecular like clusters ($\frac{1}{D} \gg 0$) to bulk materials ($\frac{1}{D} \approx 0$), can be plotted in one graph.

For Ag clusters in vacuum or embedded in weakly interacting media two a-factors compete with each other for decreasing cluster size. The "spill-out" effect reduces the density of the $5s$ electrons inside the cluster and lowers the frequency of the electron gas. This leads to a red shift of the Mie resonance with decreasing cluster size (the sign of a is negative).

The size-dependent screening efficiency of the Mie plasmon leads to an opposite size effect in the resonance energy of the cluster. The strong depolarization field of the d-bands lowers the plasma frequency inside the cluster. At the cluster surface the screening efficiency of the d-electrons is reduced, because the d-electrons are more strongly localized than inside the cluster. Thus, the electron gas at the surface is less affected by the depolarization field of the 4d-electrons, which enhances the plasma frequency towards the unscreened value. The growing surface to volume ratio for decreasing cluster sizes leads to an increase of the total Mie plasmon energy and counteracts the aforementioned red shift (high positive value of a) [39].

1.5.3.5 *Supported Ag Clusters*[46]

Despite intrinsic cluster effects (such as the "spill-out" effect mentioned before), more physical effects must be considered when nanoparticles or size-selected clusters are deposited on surfaces. As mentioned in Section 1.5.3.1 Mie theory is commonly used to describe the optical properties of metal nanoparticles. However, these Mie plasmons strongly depend on structure, temperature and especially on the surrounding medium, such as matrices, adsorbates or support materials. In the following description, the influence of the latter are described in detail [89].

In this context two models, the static and the dynamic charge transfer were introduced by Kreibig et al. The first one results in an electric double-layer and changed conduction electron density in the cluster, whereas the second reduces, by phase relaxation, the lifetime of the Mie resonance [87, 90]. Static charge transfer from or to the cluster influences the "conduction"-electron density. It might increase or decrease for different surroundings within the particle which leads to a shift of the (Mie) resonance. For decreasing "conduction"-electron density within the cluster the surrounding exhibits a negative charge density which leads to a red shift of the Mie resonance, and vice versa [91]. The "chemical interface damping" introduced in Section 1.5.3.4 is of the same origin[47].

---

[46] A good summary of the interaction of metal clusters with their support material is given in [77].

[47] Static charge transfer and chemical interface damping are of the same physical origin. The first name is usually used for nanoparticles embedded in matrices, whereas the second is used for nanoparticles where the charge transfer is due to a chemical compound, e.g through oxidation or reduction of the nanoparticles.

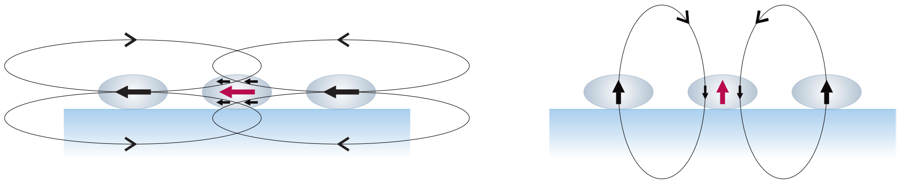

Figure 13: Schematic of the different interaction for adjacent supported nanoparticles. Both excitation schemes are shown (see text) [77].

A well known and widely observed phenomenon is the broadening of the Mie plasmon resonance when nanoparticles are embedded in matrices or deposited on surfaces (described in Section 1.5.3.4). This broadening can be interpreted by the dynamic charge transfer [91, 92, 93]. It takes place via tunneling between cluster states and adsorbate levels [94, 90]. The excited collective motion (phase coherence) of the conduction electrons is disturbed by the statistically disordered tunneling process. Thus, the tunneling electrons do not contribute to the collective oscillation, which in turn leads to a dephasing relaxation process. Therefore the collective Mie excitation in the cluster fades away. This effect increases for decreasing particle radius.

For larger supported nanoparticles local field corrections must be considered in order to understand their optical response. These are mainly induced by two different effects described in the following.

The so far described properties of the Mie resonance are only valid for non-interacting nanoparticles. However, when nanoparticles are deposited on surfaces this assumption is only valid for small coverages, where dipole-dipole interactions can be neglected. For higher coverages the particles might interact through their induced electromagnetic fields [95, 96, 97]. The dipole-dipole interaction between the nanoparticles influences the Mie-plasmon resonance [98, 99]. Here two different excitation schemes must be distinguished. If nanoparticles are excited parallel to the surface, the dipole-dipole interaction is constructive leading to a red shift of the Mie resonance. For an excitation normal to the surface the dipole-dipole interaction is destructive leading to a blue shift of the Mie-plasmon. Both excitation schemes and corresponding interactions are depicted in Figure 13.

Another support effect towards supported nanoparticles was described by Yamaguchi et al. and Royer et al. [100, 101]. They stated, that the Mie resonance induces an image dipole in the substrate which influences the Mie plasmon. Both excitations parallel and orthogonal to the surface are constructive, thus lead to a red shift of the Mie resonance compared to gas-phase spectra shown in Figure 14. However, this effect does not depend on the coverage[48].

---

[48] A more detailed description on local field effects can be found in literature [25].

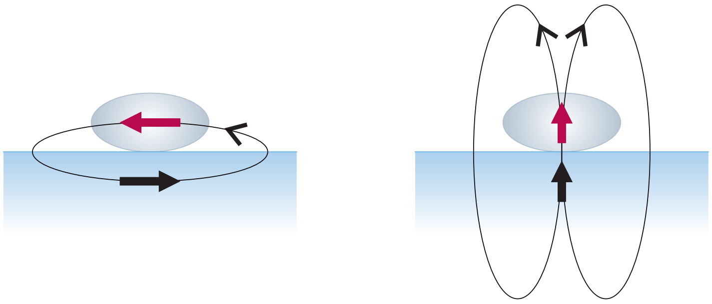

Figure 14: Image dipoles of supported spherical nanoparticles (see text) [77].

1.5.3.6 *Shape Factors*

The Mie resonance is a solution of the Maxwell equation for spherical particles and given boundary conditions. Supported nanoparticles might, however, exhibit non-spherical shape. This deviation from spherical shape leads to a splitting of the plasmon modes which depends on the orientation of excitation. For oblate particles the plasmon splits into two modes corresponding to an oscillation parallel $(1,1$ mode) and orthogonal $(1,0$ mode) to the support surface (see Figure 15). These two Mie resonances strongly depend on the shape of the cluster and can be probed by direction dependent excitation [101, 102].

For supported oblate nanoparticles the parallel mode is red shifted, whereas the orthogonal mode is blue shifted compared to the Mie resonance of a spherical nanoparticle. This plasmon splitting has been observed for silver nanoparticles in the author's group [25, 82]. Probing both plasmon resonances is a powerful way of determining the ratio of the orthogonal and parallel axes of the Mie plasmon and thus the shape of the cluster. Note that S-SHG spectroscopy can only be used to probe modes perpendicular to the surface (see Figure 15)[49].

To account for this plasmon splitting the Mie theory is often expanded by shape factors, L_i, where the index, i, represents one of three principle axis of the particle. It can be shown, that for an oblate particle[50] within the Mie theory the extension cross section of the i-th axis is given by [102]:

$$\sigma_{i,ext} = \frac{\omega}{c_0}\epsilon_m^{\frac{3}{2}} V_0 \frac{\epsilon''(\omega)}{\left[\left(\epsilon'(\omega) - \epsilon_m\right) L_i + \epsilon_m\right]^2 + \epsilon''(\omega)^2 L_i} \tag{60}$$

This modified Mie resonance can be used to describe the strong plasmon splitting, which has been observed for supported nanoparticles with $D \geq 2$ nm [102].

---

[49] The parallel mode $(1,1)$ exhibits a harmonic potential and can thus not be probed by SHG spectroscopy.

[50] For an oblate shape the shape factors are given by $L_c < L_a = L_b$, where a, b and c represent the three principal axes.

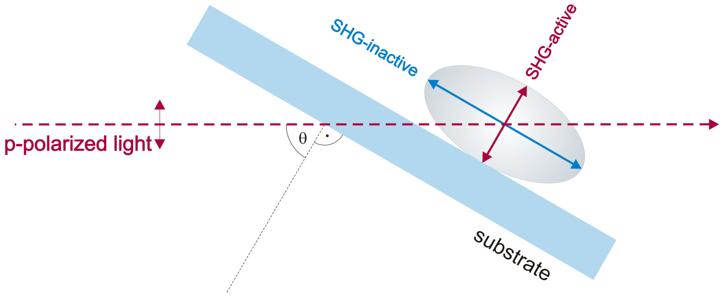

Figure 15: Two plasmon modes of an oblate supported nanoparticle. Only the orthogonal mode is embedded in an asymmetric potential and is thus SHG active [77].

1.5.3.7 *Size-Selected Clusters*

Up to now the optical properties of metal nanoparticles were described classically within the (modified) Mie theory. This rather simple approach leads to a good understanding of the different spectroscopic effects observed for nanoparticles ($D \gtrsim 2$ nm). It also gives a great insight into the different physical forces inside the cluster, and due to it's possible extensions mentioned in the preliminary sections, it is a great theoretical description for plasmons in metal nanoparticles.

However, for even smaller clusters the collective plasmon osscilation might split into discrete energy levels, making the theoretical description within the classical Mie theory obsolete to some extent. To account for this process different theoretical approaches have been suggested in literature[51].

One famous model for small (size-selected) cluster adopted from nuclear shell theory was introduced by Knight et al. in 1984 [103]. It was shown that large peaks in mass spectra of size-selected sodium gas phase clusters can be understood in terms of an one electron shell model in which independent delocalized 3s electrons are bound in a spherically symmetric potential (jellium model) [104]. They solved the one electron Schrödinger equation for a particle inside a sphere constrained to move under the influence of an attractive central potential [1]. Consequently, the electron eigenfunctions are labeled by the quantum number n, l, m_l known from atoms[52]. Closed shell clusters arise due to the complete filling of the "jellium orbitals": $1s(2), 1p(6), 1d(10), 2s(2), 1f(14), 2p(6), 1g(18)$,... leading to the "electronic magic numbers" shown in Table 3. Clusters of these sizes are expected to be particularly stable. Increasing the cluster size by one atom leads to an opening of a new shell which makes the cluster relatively unstable. The shell model is applicable to clusters of nearly

---

[51] A good summary of different theoretical approaches can be found in [28].

[52] Unlike in the model for atoms, where l must be smaller than n, there is no restriction on the relevant values of l and n here because the corresponding potential is not of coulomb form [105].

free electron metals. The noble metals Co, Ag and Au exhibit the same magic numbers [106]. These magic numbers can be probed by electron impact measurements, e.g. for silver ($2 \leq n \leq 36$) [107].

Also, an often observed even-odd pattern in the ionization potential can be attributed to the binding energies of the electrons within the shells. Unpaired electrons can be removed more easily and thus their corresponding clusters are less stable than clusters with paired electrons. This effect is called the even-odd effect [108]. Both the stable shells as well as the even-odd alteration can be seen in the mass spectra of Ag clusters later presented in this work. Another effect of (geometric) magic numbers results from the structure of rare gas clusters. Mass spectra e.g. of positively charged Xe clusters show distinct intensity anomalies [109, 110]. These can be explained by especially stable icosahedral shells[53] with multiple five-fold symmetry for the numbers shown in Table 3 [1, 112].

NUMBER OF ATOMIC SHELLS	GEOMETRIC MAGIC NUMBER	ELECTRONIC MAGIC NUMBER
0	1	2
1	13	8
2	55	18
3	147	20
4	309	34
5	561	40
6	923	58

Table 3: Geometric and electronic magic numbers of metal clusters with spherical symmetry.

1.5.3.8 *Size-Selected Silver Clusters*

A short summary of vital measurements on size-selected silver clusters is given in the following paragraphs.

Tiggesbäumker et al. measured size-selected silver clusters ($n = 5, 7, 9, 21, ..., \langle 70 \rangle$) by photo-depletion spectroscopy in gas phase. They found a clear blue shift of the Mie-resonance for closed shell clusters with decreasing cluster size[54] [31, 113]. Clusters with partially filled shells showed a splitting of the Mie-resonance into several components, however their resonance frequencies were averaged for better

---

[53] Often referred to as Mackay Icosahedral [111].

[54] $\omega(Ag_5) \approx 4,35$, $\omega(Ag_7) \approx 4,17$, $\omega(Ag_8) \approx 3,97$, $\omega(Ag_9) \approx 4,02$, $\omega(Ag_{11}) \approx 3,98$, $\omega(Ag_{13}) \approx 3,95$, $\omega(Ag_{15}) \approx 4$, $\omega(Ag_{17}) \approx 3,96$, $\omega(Ag_{19}) \approx 3,97$, $\omega(Ag_{21}) \approx 3,84$, $\omega(Ag_{<50>}) \approx 3,8$, $\omega(Ag_{<70>}) \approx 3,77$.

comparison. Doing so, they found a strong blue shift of approximately $0,6$ eV for this size regime and attributed it to the reduced s-d screening interaction in the outer regions of the Ag particles.

Several experiments were also conducted in inert cold matrices. Harbich et al. investigated size-selected silver clusters $(n = 8 - 39)$ embedded in solid Ar, Kr and Xe matrices by absorption spectroscopy [114, 33, 36]. They found 1 - 3 strong absorption peaks between 3 and $4,5$ eV depending on the cluster size. For clusters with n $\geq$ 12 predominantly only one peak was observed and attributed to the collective oscillation of the s-electrons. The observed blue shift was explained by the size dependent "spill-out" effect. The matrix induced red shift was estimated to be $0,24$ eV. The high resolution and hence small width of these peaks was attributed to the low temperature of the matrices. The authors stated that the absorption cross section scaled with the number of valence electrons.

Great progress in the field of (supported) size-selected cluster was also achieved by many theoretical approaches. Some are summarized in the following description:

Kasperovich et al. calculated the photo absorption cross-section within the two region model[55] for spherical small (Ag_9 toAg_{40}), isolated, positively and negatively charged silver and gold nanoparticles. They predicted, amongst other results, a blue shift for Ag cations and anions with decreasing cluster size which was explained by an interplay between the d-electron screening and a valence electron "spill-out" [32].

Yabana et al. applied the time-dependent local-density approximation (TDLDA) to the optical response of very small silver clusters (Ag_2, Ag_3, Ag_8 and Ag_9^+) [115]. With this approach they found good agreement to the empirical spectra by Tiggesbäumker mentioned previously [113].

Bonacic-Koutecky et al. calculated absorption spectra for the most stable structures as well as for other isomers of Ag_5 to Ag_8 in the gas-phase and at zero temperature[56]. They found distinct transition energies, however also a strong dependency on the isomeric forms. Starting at Ag_5 the spectra are dominated by one dominant peak which is located in the energy interval between $3,5$ eV and $4,1$ eV. Addition of a single atom leads to a blue shift of the resonance by $0,2$ eV[57][116].

---

[55] In this model a spherical cluster is divided into an inner and an outer region where a bulk- and a Drude-like dielectric function of the valence electrons is used respectively. This accounts for the effect that in the the outer region d-electron screening is ineffective.

[56] An 11-electron relativistic effective core potential was used where 11 electrons per Ag-atom are included in the theoretical treatment.

[57] This is in contrast to our and other mentioned measurements, however might be attributed to the amount of very sharp peaks as well as to the strong dependency of the conformation.

Aikens et al. employed time-dependent density functional theory TDDFT calculations to calculate the optical absorption spectra of silver tetrahedral Ag_n $(n = 10, 20, 35, 56, 84, 120)$ clusters. They found good agreement to experimental results and showed the evolution from molecular-like to plasmon-like transitions with increasing n [37].

1.5.3.9 *Reactivity and Reaction of Metal Clusters*

Nanoparticles or clusters which are deposited on support materials exhibit free uncontaminated surface regions, where the deposition or adsorption of reactive gases can initiate surface chemical reactions [1, 70].

In general, different types of interactions between supported clusters and molecules might occur. The simplest interaction is adsorption. Here, the molecule remains bound to the cluster rather than being incorporated into the cluster.

This is often the case for low temperatures where molecules physisorb on the cluster via very weak van der Waals interactions. The describing mechanism is an interaction between instantaneous dipoles which are generated in the cluster and adsorbate because of quantum mechanical fluctuations of their electron clouds [45]. However, at slightly higher energies molecules might chemisorb and are hence covalently bonded to the cluster[58]. In that case two distinct situations are possible which depend on the activation barriers to bond braking, the energy state of the cluster and reactant molecule and the binding between the molecule and the cluster. In "dissociative adsorption" the molecule AB breaks up into A and B which are bound to the surface of the cluster. In "non dissociative adsorption" the molecule remains intact, however this process might lead to heating which may in turn lead to dissociation of the molecule [1].

1.5.3.10 *Oxidation*[59]

An often described mechanism for the oxygen-silver surface interaction is characterized by the physisorption of O_2 at low temperature. It is followed by warming by a molecularly chemisorbed state, explained by an electron transfer from the metal to the O anti-bonding π^* orbital which is precursor state for dissociation. Additional heating transfers this superoxide O_2^- to the peroxide molecule O_2^{2-} which is unstable and dissociates [118, 119].

However, not much is known about the oxidation of supported size selected silver clusters. Some groups investigated the oxidation of sil-

---

[58] In heterogeneous catalysis for example, chemisorbed molecules react with each other via the formation of chemisorbed intermediates. After formation the product may desorb from the surface.

[59] A good but obviously incomplete literature review about the oxidation of silver clusters is given by [117]. The following summary is partially based on that source.

ver nanoparticles in solution, in gas phase or on support materials in the past ∼ 30 years. As the oxidation of silver clusters is of special interest for the data later presented in this work some extensive examples of measurements are described in the following. Here, examples of the oxidation of nanoparticles in the gas phase, in solution as well as on support materials are summarized.

Götz et al. investigated supported sodium nanoparticles with diameters between 1 and 200 nm by means of S-SHG spectroscopy in the mid nineties[60] [120]. They performed oxidation measurements (with an O_2 background pressure of $p = 10^{-8}$ mbar) for supported sodium nanoparticles with a diameter of ∼ 40 nm. The exposure to oxygen led to a rapid decrease (within approximately 100 s) of the SHG intensity before the signal saturated at about 15 % of it's original intensity. They attributed this observation to the chemisorption of oxygen onto the nanoparticles and concluded that the SHG signal almost exclusively originates from the surface of the clean nanoparticle, and that higher order bulk contributions are negligible.

Gas phase studies on the oxidation of small silver clusters were performed by Bernhardt et al. in the beginning of the last decade [121, 122]. Positively charged silver dimers were exposed to O_2 at different temperatures in an ion trap and the reaction kinetics were analysed[61]. They proposed a reaction mechanism from $Ag_2{}^+$ + O_2 leading via intermediate states to $Ag_2O_3{}^+$ where the chemisorbed O_2 molecule dissociates. Further experiments with cluster sizes up to Ag_{13}^- were performed [123]. A strong size-dependent reaction behavior of CO and O_2 on free silver cluster anions was found. A good summary of these experiments is given in ref. [124].

Schmidt et al studied the physi- and chemisorption of oxygen on small silver particles in the gas-phase [118]. They performed temperature dependent gas phase experiments of silver clusters with oxygen. The authors stated that oxygen species physisorb on the clusters at temperatures below 77 K, but chemisorb where the valence electron is extracted from the cluster above 77 K. Here, the oxygen molecule takes one electron from the delocalized valence electrons of the nanoparticle. For temperatures above 105 K the chemisorption turns into permanent oxidation, where the O reaches the oxidation state of −2 which inturn leads to dissociation. Then one highly reactive oxygen atom is ejected from the cluster and the residual metallic silver cluster can undergo further oxidation, until the cluster is completely oxidized.

Experiments on the oxidation of supported silver cluster were performed by Kreibig et al. They investigated the oxidation of small (2 nm) deposited Ag-clusters by means of fast optical extinction mea-

---

[60] The experimental setup has some similarity to the one described in this thesis, but the experiments are performed at one wavelength (532 nm).

[61] Neutral silver dimers are unreactive towards O_2 at ambient conditions.

surements [70, 87]. By observing the changes of the peak position and intensity (ca. 10 %) and the band width of the Mie resonance increasing with time they could prove that the Mie resonance is a highly sensitive sensor for chemical surface reactions including kinetics providing they are slow. However, in the case of oxygen[62], the effects in the Mie spectra remained small, even at highest pressure (at $4 \cdot 10^{-4}$ mbar). They claimed that this is due to weak saturating reactions limited to the surface[63], and attributed the observed small changes in the Mie spectra to weak surface oxidation of the silver clusters. For the reaction with sulfur (at 10^{-6} mbar) however, they observed a fast decrease in intensity leading to a complete vanishing of the Mie plasmon at room temperature. They interpreted this behavior by the formation of silver sulfides, which begins at the surface and in contrast to oxygen proceeds through the whole particle. The silver sulfide is a dielectric and does not exhibit a Mie plasmon-resonance, hence the peak disappears.

Hillenkamp et al. investigated the stability of silver nanoparticles with a diameter of $3 \lesssim D \lesssim 5$ nm in silica matrices under ambient conditions [125]. The Mie-plasmon resonance decreased over a timescale of days and was accompanied by a red shift of the resonance until it vanished completely. They attributed this behavior to a complete (volume) oxidation of the whole cluster.

Kim et al. studied the oxidation of Ag nanoparticles on HOPG by means of XPS [126]. They found a particle size dependent oxidation: small particles with a diameter of 1 nm oxidize faster than bigger particles.

Dai et al. performed SHG spectroscopy to monitor the interaction of wet chemically synthesized silver nanoparticles (80 nm diameter) with sulfides [127, 128]. They claimed that the SHG signal arises mainly from the surface, and observed a quenching via thiol addition. The SHG intensity did not vanish completely but saturated at about 50 % of the original intensity. This was assigned to localized bonds of the sulfur to the silver atom.

By the above mentioned examples from literature it can be seen that silver nanoparticles oxidize under certain conditions. Mie resonance of silver clusters can be used to probe cluster-surface reactions, since it should be influenced by chemisorbed species. However, for supported silver nanoparticles only weak surface oxidation was observed by spectroscopy. To the best of the author's knowledge no experiments on the oxidation of supported size-selected clusters have been reported yet.

---

[62] and in contrast to the oxidation measurements shown in this thesis.

[63] Planar silver surfaces at room temperature only bind oxygen chemically at imperfections like steps.

1.6 SUMMARY

In this chapter the theoretical spectroscopic background for the results presented in this work was introduced and discussed. First, a classical description of the linear interaction of light and matter was given which led to a short survey of chirality in linear optics. It could be shown that "linear" materials only exhibit chirality in spectroscopy when magnetic contributions are incorporated. Based on these findings the nonlinear interaction of light and matter was introduced and a detailed description of the nonlinear susceptibility tensor $\chi^{(2)}$ was given within the electric dipole approximation. The properties of this 3rd rank tensor were shown to be of fundamental importance for both spectroscopic techniques used in this thesis. The nonlinear response of charges which are embedded in an anharmonic asymmetric potential leads to an emission of light, at the exciting fundamental, and twice the fundamental frequency. This was shown to be the fundamental reason for the outstanding surface sensitivity of S-SHG spectroscopy.

The chiroptical response of nonlinear materials could be derived from further symmetry considerations of the nonlinear susceptibility tensor $\chi^{(2)}$. Here, magnetic contributions are not mandatory. For a chiral isotropic surface the 27 tensor elements were shown to be dependent and were reduced to 4 independent elements. Parameters, which are linear combinations of these elements were introduced in order to simplify the theoretical description. The SHG-ORD effect was deduced from these considerations and shown to be material (tensor elements, orientation) as well as incident-angle dependent. The probe molecule of interest (Binol) was described and it was shown that it's nonlinear chiral response can be described by including only electric dipole transitions.

In the second part of this chapter the optical properties of metal nanoparticles were presented. The Drude model was derived from the fundamental interaction of light and metal bulk materials. On this basis plasmon oscillations were explained as a collective motion of electrons within a nanoparticle, which lead to distinct optical properties different to their corresponding bulk materials. In this context Mie theory was presented and the advantage as well as the limits of the theory were discussed. Silver was shown to be the perfect material for the spectroscopic investigation of small nanoparticles because of it's distinct and pronounced plasmon oscillation. In order to fit the experimental results Mie theory was qualitatively extended by effects, such as "spill-out", substrate interaction and shape factors.

The optical properties of very small (size-selected) clusters were discussed and shown to contradict Mie theory to some extent. Qualitative mathematical expansions to Mie theory were deduced from theoretical considerations in order to fit experimental results. At the end the interaction (physisorption, chemisorption and oxidation) of nanoparticles with adsorbates were discussed and a literature review of similar experiments was given.

Part III

EXPERIMENT

2

EXPERIMENTAL SECTION

The experimental setup is described in this chapter. All of the data presented in this thesis, were measured with this setup. Some parts of the experiment have been described before [29, 25, 129, 117] and thus only a short description will be given here. Nevertheless a brief description of the entire experimental setup is given to ensure an adequate overview. Firstly, a summary of the different vacuum chambers and their corresponding features is given. The core components including the cluster source, the bender chamber and the analysis chamber are described. The transfer chamber containing the HV evaporator and the quartz micro balance (QMB) as well as the gas line were implemented during the work for this thesis and are hence described in greater detail.

In the second part a description of the spectroscopic setup that was used in this work is provided. It was implemented during this work to allow S-SHG measurements[1], as well as chiral-sensitive measurements of adsorbates by SHG-ORD spectroscopy. Both spectroscopic methods can readily be switched without the need for re-alignment.

Following this the electron source is described, which was modified and characterized. Finally an example of the measuring procedure as well as of the data treatment is given.

2.1 OVERVIEW OF THE CHAMBER

A true to scale sketch of the different vacuum chambers is depicted in Figure 16. The whole chamber functions using the differential pumping principle. Pure helium (He 6.0 Air Liquid) is used as a buffer gas to form metal clusters (see Section 2.2). The helium background pressure, which is $\gtrsim 10^{-3}$ mbar in the source chamber is consecutively reduced to $\sim 10^{-6}$ mbar in the analysis chamber during deposition[2]. The clusters are prepared by laser ablation using a cluster source similar to the one described by Heiz et al. [29, 130]. The source chamber is pumped by a roots pump (Pfeiffer WKP 500A) for sufficient gas load. A skimmer between the "source chamber" and the following octopole chamber acts as a first cation filter [3]. The "octopole chamber" is pumped by a turbo pump (Pfeiffer TPU 1201 P) to remove helium and decrease the water and oxygen partial pressure that would pre-

---

[1] Before this work mostly linear absorption spectroscopy (cavity ring-down spectroscopy) was performed with this experimental setup.

[2] Note, that for spectroscopic measurements the valve between the analysis chamber and the bender chamber is closed providing a background pressure of $\sim 10^{-10}$ mbar.

[3] In principle it could also act as a anions filter.

vent cluster formation. The octopole is operated by a RF transceiver (Kenwood, TS-570S) with an AC potential to guide the ions through the octopole chamber with high transmission. The formed (silver) clusters are guided through the octopole towards the bender chamber. Here the cations are separated from the residual anions and neutral clusters by a quadrupole deflector. This chamber is pumped by a turbo pump (Pfeiffer TPU 510) and can also be separated via gate valves from the other chambers. Afterwards, the cationic clusters enter the analysis chamber and are guided through a quadrupole mass spectrometer (Extrel 5500). Here, the mass selection takes place. Cations of a particular mass to charge ratio can be selected by the corresponding software (Extrel, Merlin 3.0)[4].

The complete guidance of the cation clusters is performed by 7 different Einzel lenses, shown in Figure 16. The applied voltages must be optimized for different metals and adapted to different cluster sizes. The last pair of Einzel lenses after the QMS focus the clusters onto the substrate. Before deposition the substrate has to be brought into the analysis chamber and fixed onto the electron source. This enables the transfer of the substrate into the chamber without breaking UHV conditions in the analysis chamber.

The cleaned substrate is mounted onto a sample holder which is attached to a movable long transfer rod within the transfer chamber. In addition the evaporator and the quartz-micro-balance are also mounted within this chamber which allow for monitored evaporation of molecules from the solid phase. Once the pressure in the transfer chamber underruns a critical value the gate valve between the transfer chamber and the analysis chamber is opened and the substrate holder is fixed onto the electron source. A detailed description of the different chambers is given in the following sections.

2.2 CLUSTER SOURCE

The used cluster source is similar to the one described by Heiz et. al. [131] and is well described in ref. [29]. The round metal target (silver) is mounted onto a motor which drives in a hypocycloidal motion during operation. A frequency doubled Nd:YAG laser (Innolas Spitlight DPSS, 532 nm, 100 Hz repetition rate, 70 mJ/pulse, 11 ns puls width) is focussed onto the metal target in order to ablate the material from the target. A piezo valve is installed at the nozzle. Using this valve helium pulses (He 6.0, Air Liquide) are dosed, triggered by the laser (100 Hz). The length, amplitude and timing of the gas pulse and the backing pressure of helium on the piezo valve are factors influencing the size distribution of the generated clusters. The helium atoms ther-

---

[4] For "unselected silver clusters" (Ag_x) RF-only modus is chosen. Then the applied DC current is switched off leading to a mass filter where only masses which are greater than 7/9th of the chosen value pass the filter (see Section 2.4.1).

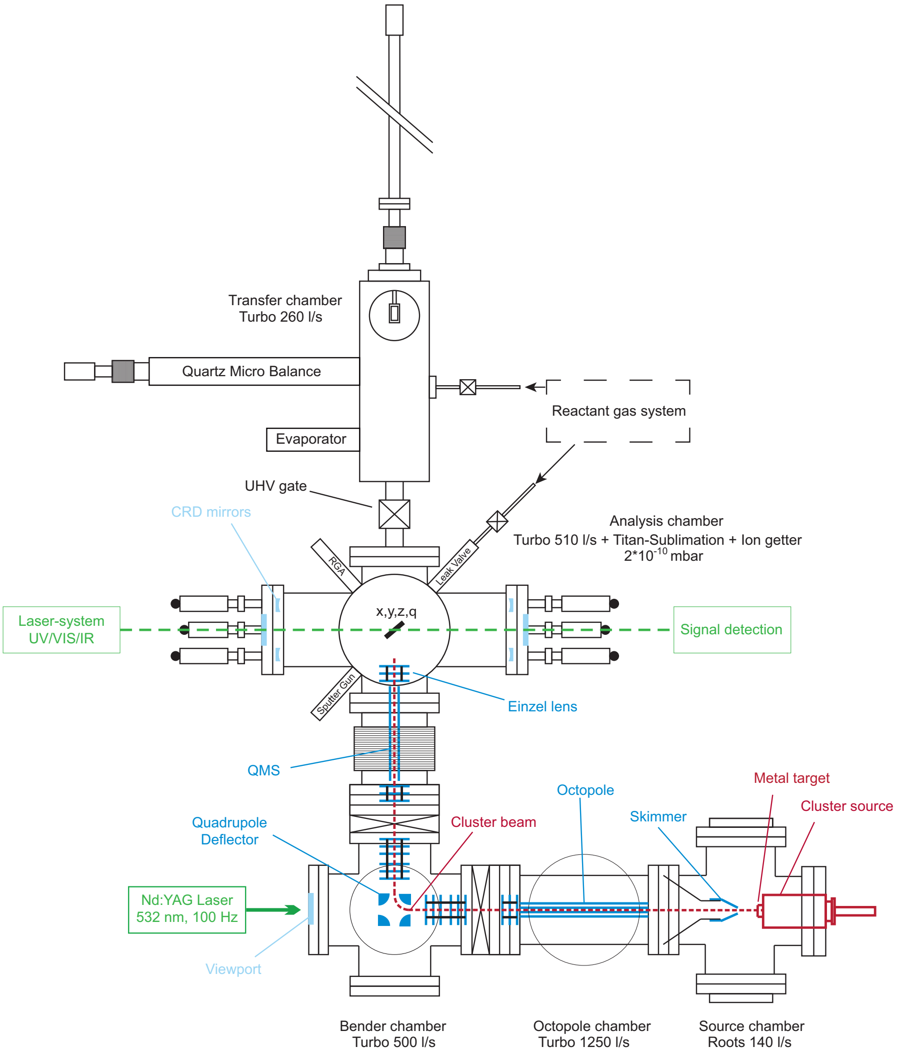

Figure 16: Scheme of the complete cluster source and UHV setup. The vacuum chambers are shown in black. The pathway of the cluster cations from production to deposition is shown in red and the ion optics, which guide the beam, are shown in blue. The pathways of the ablation laser and the ps-laser are shown in green [117].

malize the evaporated metal atoms via collisions and thereby larger clusters are formed, which are further cooled by a supersonic expansion and subsequently guided through the chambers.

2.3 TRANSFER-CHAMBER

A new transfer chamber was built during this work[5]. It is connected to the analysis chamber via a gate valve which allows for the transfer of the sample into the analysis chamber without breaking UHV conditions. The chamber is pumped by a turbo pump (Pfeiffer HiPace 300). The substrate (BK7) is mounted onto the substrate holder via four springs and subsequently fixed onto a long transfer rod via a fast entry lock which is mounted on top of the transfer chamber. Afterwards, the fast entry lock is closed and the transfer chamber is pumped until a background pressure of ca. 10^{-7} mbar is reached. This takes approximately 20 minutes. Subsequently the sample holder is transferred by the long rod into the analysis chamber. This working procedure allows the transfer of the substrate from ambient conditions into the analysis chamber without breaking UHV conditions there. A home built evaporator is connected at the bottom of the transfer chamber for evaporating organic molecules (see Section 2.3.1). A quartz microbalance is connected by a linear UHV stage to the transfer chamber and allows for maximum control of the deposition (see Section 2.3.2). The transfer chamber also facilitates the pumping of the gasline which is described in Section 2.3.3.

2.3.1 *Evaporator*

An evaporator of in-house design was built and connected to the bottom of the transfer chamber. This turned out to be a crucial addition to ensure constant evaporation currents. It was used to evaporate (organic chiral) molecules onto the substrate under HV conditions. Three different cups can be filled by materials of interest and heated up separately. This allows for three different measurements before the evaporator has to be refilled. All SHG-ORD measurements of evaporated molecules (Binol) presented here were performed using this evaporator. For the evaporation of Binol molecules a constant current of $1,25$ A was chosen for heating.

2.3.2 *Quartz Micro Balance (QMB)*

A quartz microbalance (INFICON SL-A1E40) was attached to the transfer chamber to monitor the evaporation process (see Figure 17). It is mounted onto a linear manipulator which allows for the adjust-

---

[5] The transfer chamber was mainly developed by Dr. Kartouzian.

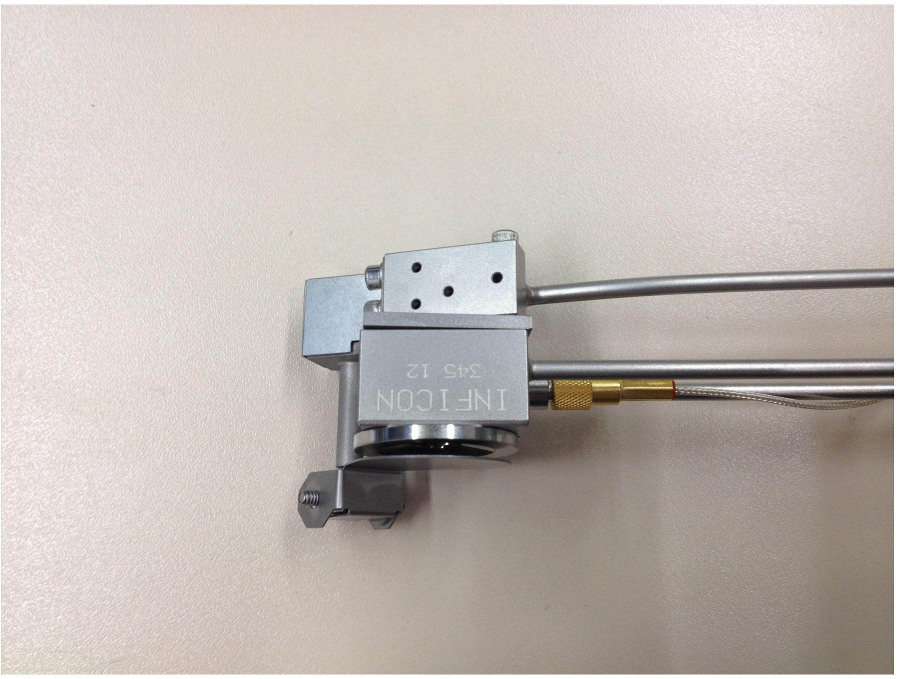

Figure 17: Picture of the Quartz-Micro-Balance. A shutter allows for minute control of the deposition. The crystal is cooled by a chilled water flow.

ment of the position of the QMB above the evaporator in order to accurately monitor the evaporating process. A QMB is a simple and very powerful tool for measuring ultrathin evaporated films [132]. It measures a deposited mass increase by recording the resonance frequency decrease of an underlying quartz crystal[6]. In this work the "Sauerbrey equation" [134] was used to calculate the amount of evaporated molecules on the surface - often called "Sauerbrey thickness". The equation is derived by treating the evaporated mass as though it were an extension of the underlying crystal. For a film with the same acoustic properties as the crystal the correlation between the frequency difference $\triangle f$ and the increase in mass $\triangle m$ [132] is predicted as:

$$\frac{\triangle f}{f_o} = -\frac{\triangle d}{d} = -\frac{\triangle m_f}{m_q} \tag{61}$$

with f_0 representing the frequency of the unloaded crystal, d the thickness and $\triangle d$ an infinitesimal change of the crystal thickness. $\triangle m_f$ is the infinitesimal amount of deposited mass and m_q the mass of the crystal. The negative sign signals that an increase in the thickness of the quartz crystal causes a decrease of it's resonant frequency. With the assumption that for small mass changes the addition of foreign mass can be treated as an equivalent mass change of the quartz crystal itself Equation 61 leads to:

---

[6] Most of the description and theory can be found elsewhere in greater detail [133].

$$\triangle f = -\frac{2f_0^2}{A\sqrt{\rho_q \mu_q}}\triangle m \tag{62}$$

where A is the active crystal area, $\rho_q = 2,648\frac{g}{cm^3}$ is the density of the quartz crystal and $\mu_q = 2,947 \cdot 10^{11}\frac{g}{cms^2}$ is the shear modulus of quartz. This equation was used for calculation of the amount of molecules deposited by evaporation on the substrate. It is common to use Sauerbrey's equation when the difference in frequency between the loaded and unloaded crystal is smaller than 2% which was the case for all evaporations performed in this work [135].

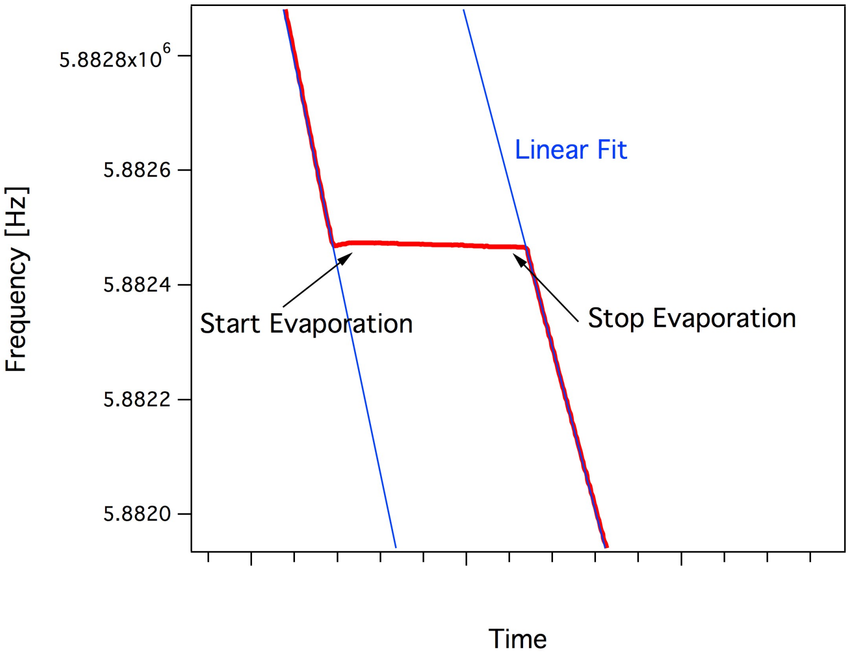

Figure 18: Recorded data from the QMB of an evaporation process. The deposition rates before and after deposition are linearly fitted.

The QMB can be moved above the evaporator for measurement of the exact deposition current at the position where the subsequent deposition of organic molecules on the substrate takes place. Coverage-dependent measurements were performed as follows: Before deposition the deposition-current is measured and recorded until it is constant. During deposition the QMB is moved away and the cooled substrate is moved above the evaporator (at the position where the QMB previously measured the deposition current). After deposition the QMB is again moved above the evaporator and the deposition current is recorded again. This method allows for minute deposition control without the need of any correction-factors[7]. The deposition rate before and after deposition is recorded and subsequently linearly

---

[7] Often a fixed sensor is used which is located beside the substrate. Then a tooling factor must be calibrated in order to calculate the actual deposition rate at the position of the substrate.

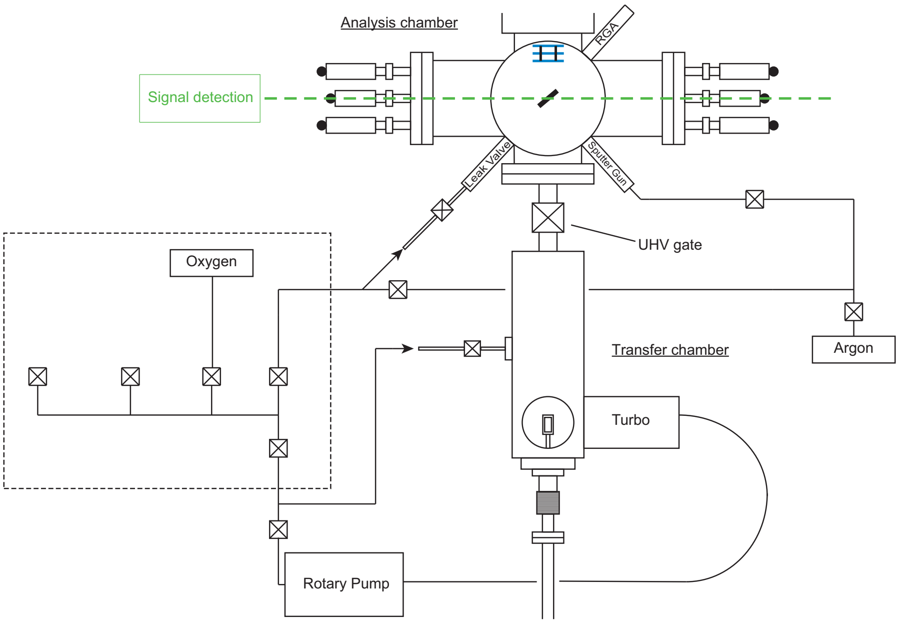

Figure 19: Schematic of the gas line setup. A certain background pressure can be applied to the analysis chamber using a leak valve. It is possible to pump the gas line with a rotary pump and the turbo pump of the transfer chamber [117].

fitted. The deposition rate during deposition is assumed to be the arithmetic average of both slopes of the linear fits. With the slopes of the fit the deposited mass during deposition can be calculated using Equation 62. One recorded evaporation process including the two linear fits is shown in Figure 18.

2.3.3 *Gas Line*

A new gas line was built and attached to the experimental setup during this thesis. A scheme is shown in Figure 19. It allows for the performance of gas-background pressure-dependent measurements inside the analysis chamber. In principle any gas can be introduced through the gas line. It is connected to both the transfer chamber and the analysis chamber. The gas line is pumped via the connection to the transfer chamber. Once pumped the gas line can be filled with the gas of interest, which subsequently can be leaked into the analysis chamber via a leak valve.

Additionally, the gas line is connected to an argon (Westfalen AG, 4.6) line that provides Ar gas for the sputter gun[8]. Using these connections the line of the sputter gun can also be cleaned. To clean the gas line it is flushed with Ar or He and pumped a few times. In the

---

[8] A sputter gun(EX03 Ion Gun System-Thermo VG Scientific) is connected in the analysis chamber in order to allow cleaning of substrates.

data presented in this work oxygen and hydrogen were connected to the gasline and leaked into the analysis chamber.

2.4 ANALYSIS-CHAMBER

The analysis chamber is the main part of the experimental setup. Here the deposition of the clusters onto the cleaned substrate takes place as well as the subsequent spectroscopic investigation (see Figure 16).

2.4.1 *Quadrupole Mass Spectrometer*

The quadrupole mass spectrometer (Extrel, 5500 series) acts as a mass filter for the positively charged clusters. It is composed of four rods where a superposition of a DC and an RF electric field leads to a mass-filter where charged particles of only one specific mass are guided through the quadrupole. All other masses do not pass the filter. The selected masses can be changed by adjusting the DC and RF currents via the corresponding software (Extrel, Merlin 3.0). Here, the voltages of the entry and exit Einzel lenses can also be adjusted in order to optimize the cluster current which passes the QMS. In Figure 20 a mass spectrum of silver clusters is shown[9]. Some effects can be observed here. The voltages of the Einzel lenses in the source- and bender chambers as well as the currents and voltages at the quadrupole were adjusted in order to optimize the Ag_{21} cluster current. This leads to a maximum of Ag_{21} clusters in the mass spectrum. The resolution decreases for larger masses, thus it has to be adjusted for every cluster size. Also an even/odd pattern was observed which can be attributed to the binding energies within the electronic shells of the cluster. This effect is described in Section 1.5.3.7.

The QMS can also be operated in the "RF-only mode". In this mode the applied DC current is switched off leading to a mass filter where only masses which are greater than 7/9th of the chosen value pass the filter. This is a very powerful and important feature and was always used for the deposition of "unselected" clusters (Ag_x).

2.4.2 *Electron Source*

The electron source is shown in Figure 21. The basic operating principle of the electron source is the production of electrons by a hot tantalum filament which is wound around a ceramic rod. The ejected electrons have a kinetic energy between 0 eV and 12 eV and are guided through two charged metal meshes leaving the source in a down-

---

[9] The clusters were deposited on a metal plate which was connected to a picoamperemeter for the recording of the cluster current.

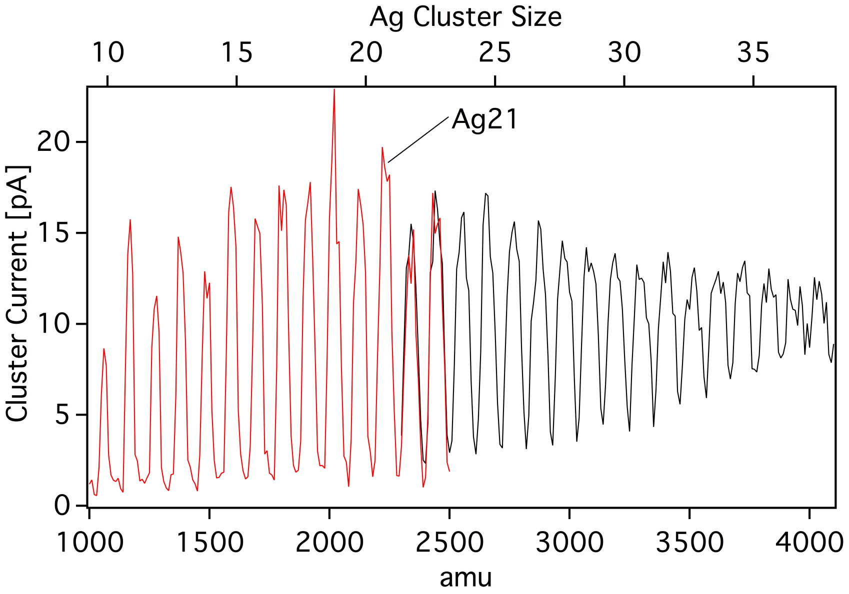

Figure 20: Mass spectrum of silver clusters. The cluster source was optimized on Ag_{21}. Two spectra were overlaid (red and black). The even/odd pattern (for ($n \lesssim 28$) as well as the optimization on Ag_{21} can be seen.

wards direction to the substrate where the clusters are deposited. During the deposition the positively charged clusters are neutralized through the electrons. The principle of operation of the electron source is well described in ref. [29, 25]. However, it was modified during this thesis in order to optimize the cooling of the substrate. Characterization and temperature-dependent measurements were performed and are well described in reference [136].

2.4.3 *Substrate Holder*

The substrate holder was built with the transfer chamber to allow substrate changes without breaking UHV conditions in the analysis chamber. Once the substrate is cleaned with spectroscopy grade acetone, it is mounted onto the substrate holder and transferred via the transfer chamber into the analysis chamber. Here, it is attached to the liquid nitrogen cooled electron source (see Figure 17 and Figure 22).

During deposition, the substrate, which is attached to the electron source, is located near the last Einzel lens of the QMS (see Figure 16). Hence, the voltage on the last Einzel lens influences the electric field in the vicinity of the substrate which guides the emitted electrons. In order to measure this dependency of Einzel lens to substrate holder for different distances the electron current on the substrate was measured via a metal plate attached to the substrate (see Figure 22). The result of the measurement is depicted in Figure 23. It can be seen that the electron current on the substrate strongly depends on the distance

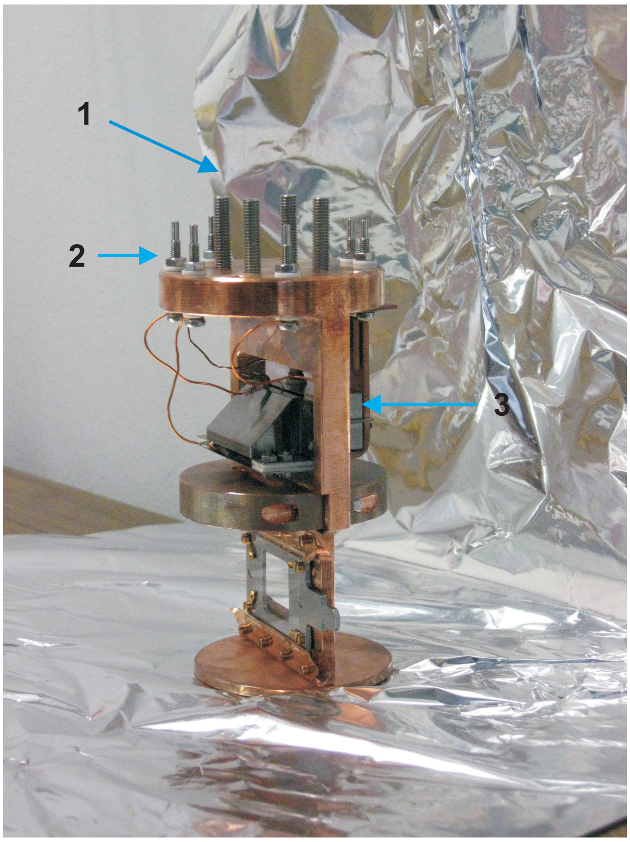

Figure 21: Picture of the modified electron source. 1) The electron source is mounted by 4 screws to the liquid nitrogen cooled mount of the manipulator. 2) The voltages are also connected to cables mounted to the manipulator leading to an external power supply. 3) Here, the electrons are produced by a hot tantalum filament.

between the substrate holder to the last Einzel lens as well as on the applied voltage of the Einzel lens. The electron current on the substrate should be maximal in order to achieve best neutralization of the cationic clusters. Thus, these values have to be optimized[10].

2.5 SPECTROSCOPIC SETUP

The spectroscopic setup was built during this thesis. It allows for the performance of S-SHG as well as SHG-ORD measurements of adsorbates on transparent substrates under UHV conditions[11]. A sketch is depicted in Figure 24. The picosecond laser beam is guided through the chamber as shown in Figure 16 and Figure 24. A photodiode is connected to a 4-channel oscilloscope and records the intensity of every laser pulse.

---

[10] Note, that the applied voltages of the last Einzel lens also influence the spatial distribution of the clusters on the substrate.

[11] Linear absorption spectroscopy by cavity ring-down measurements can also be performed with this setup [25].

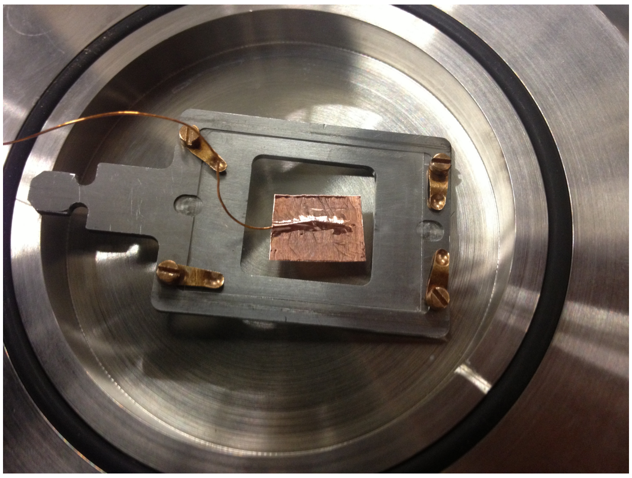

Figure 22: A photograph of the substrate holder and the substrate. A current collector made of copper is fixed onto the substrate and it is connected with a copper wiring. The wire is connected to the picoamperemeter via a feedthrough in the transfer chamber.

2.5.1 *SHG-ORD*

SHG-ORD measurements are performed at a constant wavelength. The ps-laserbeam[12] is reflected by mirrors on the laser table to ensure a straight p-polarized beam through the chamber. It passes a UV filter (Schott, GG435)[13] before it is focussed by a lens onto the substrate[14]. The substrate is mounted onto the electron source, which is in turn mounted onto a moveable and rotatable x,y,z manipulator in the UHV chamber[15]. It is cooled by liquid nitrogen to ensure a cool and stable temperature. SHG signal is generated at the adsorbates on the surface of the substrate. Both the SHG signal of the adsorbates on the substrate and the fundamental laser beam exit the chamber[16] and pass through a rotatable fresnel rhomb (B. Halle $214 - 450$ nm) and a polarizer (Glan-Taylor Prism) before being spatially separated by two rotatable Pellin-Broca prisms[17]. In order to suppress the residual fundamental light further wavelength selection is performed by a monochromator (LOT-Oriel, Omni-λ 300). The remaining SHG photons are detected by a photomultiplier tube (PMT: Hamamatsu, $H9305 - 03$) and recorded by a 4-channel oscilloscope (LeCroy, Waverunner 6051). The fresnel rhomb can be rotated by a stepper motor (Newport AG-PR100P) from 0 to 340 degrees. A home-made Lab-

---

[12] Refer to Section B for detailed description of the ps-lasersystem.

[13] The filter eliminates all residual components of the light with double frequency which might be generated at every optical component.

[14] The laser spot on the sample is $\sim 0,8$ mm^2.

[15] Compare Figure 21.

[16] The beam is recollimated by a lens behind the chamber.

[17] A detailed description of the spectroscopic properties of fresnel rhomb, Pellin-Broca prisms and the polarizer can be found in ref. [129, 137].

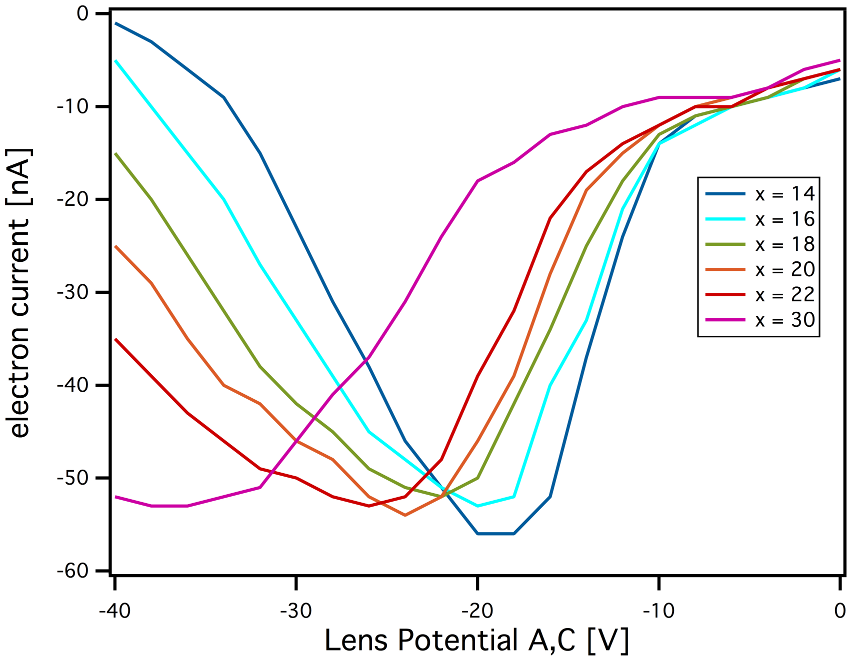

Figure 23: Electron current on the substrate as a function of lens potential (applied voltage) for different distances between substrate and Einzel lens (see text).

VIEW program allows for fully automated SHG-ORD measurements as well as for fully automated SHG-wavelength scans[18]. The Pellin-Broca prisms, the monochromator and the laser are all synchronized. The SHG-ORD measurements are performed by rotating the fresnel rhomb from 0 to 340 degrees whilst recording the intensity of the SHG signal. This rotation of the Fresnel rhomb causes the polarization of the incoming SHG signal to rotate from 0 to 680 degrees. The polarizer splits the SHG light into p- and s-polarized light and only p-polarized light is passed. To measure an SHG-ORD spectrum, 50 to 100 pulses are recorded and averaged at each angle in order to reduce noise. The angle between p-polarized light and the emitted SHG light (rotation angle ϕ) can then be determined by analyzing the resulting intensity curve.

2.5.2 *S-SHG*

For the performance of S-SHG measurements (such as nonlinear spectra of adsorbates or supported clusters) the fresnel rhomb as well as the polarizer are removed from the beam path (see Figure 24). The SHG-intensity is recorded as a function of wavelength by a 4-channel oscilloscope. This is connected to a lab computer where the ps-laser, the Pellin-Broca prisms, the monochromator as well as the oscillo-

---

[18] A new LabVIEW program was written. Refer to Section A.2.2 for a detailed description.

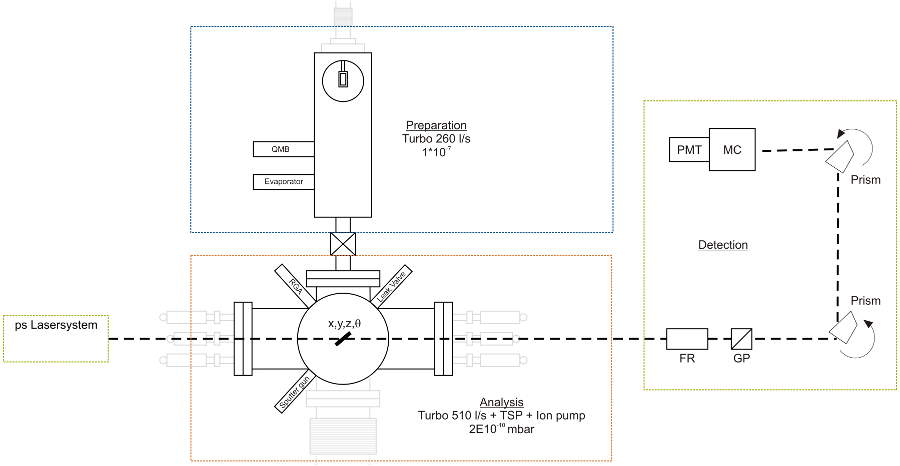

Figure 24: Schematic view of the spectroscopic setup. The beam paths for the fundamental light (red) as well as for the S-SHG light (blue) are depicted.

scope are all synchronized by the LabVIEW program allowing for fully automated scans (see Section A.1 and Section A.2.2).

2.6 MEASUREMENT PROCEDURE

2.6.1 *Support Material*

The support material is of great importance for the spectroscopic investigation of deposited molecules and clusters and must fulfill the following requirements: It must be highly transparent in the wavelength range from 400 nm to ca. 1000 nm[19] in order to avoid absorption losses. In this wavelength range only insulators fulfill this requirement. This, however, leads to the necessity for neutralization of the clusters during deposition. The substrate also needs to be very thin to avoid linear displacement of the beam path when passing through the substrate.

These requirements are fulfilled by the borosilicate glass slides (BK7) which were used in this work. The exact characterization of these slides can be found elsewhere [25].

2.6.2 *Substrate Preparation*

Amorphous BK7 glass (VWR International, BK7) with a thickness of 150 μm is used as a substrate. It fulfills several requirements, such as highest transparency (small scattering loss), parallelism of both sides, flatness and thickness. The surface roughness was measures by an AFM microscope and is below 1,8 nm [25]. All measurements in

---

[19] The wavelength range for which the support material must be transparent strongly depends on the investigated system.

this thesis were performed with this substrate. It is transparent between 300 nm and 2000 nm, thus transmission mode measurements can be performed. Since BK7 glass possesses an amorphous structure the SH generation is limited to the surface of the silde where symmetry is broken (see Section 1.1 and Section 2.7). Before use the substrate is mechanically cleaned using wipes (ThorLabs) and spectroscopy grade acetone (UvasolR , Merck). This is repeated until no further dust particles or any residual organic compound is seen with the naked eye. Afterwards, the substrate is attached to the substrate holder and inserted into the transfer chamber. It is then transferred to the sample holder as soon as the pressure in the transfer chamber is lower than 10^{-7} mbar. The substrate is sputtered to remove any residual adsorbates on the glass surface by a sputtergun (Thermo VG Scientific, EX03). The filament of the sputtergun is set to $2,6$ A and the Ar pressure of the sputtergun's leak valve is set to $5 \cdot 10^{-6}$ mbar in the analysis chamber. The high energy Ar cations with a kinetic energy between 300 to 1000 eV are able to remove impurities and displace surface atoms which leads to a roughening of the surface. To neutralize the Ar cations the electron source of the sample holder is operated with ca. $\sim$ 1.15 A ($\sim$ 15.6 V). The sputter process takes 10 minutes. The Ar^+ current was determined by a copper current collector as depicted in Figure 22. In this work the Ar^+ current is optimized by varying the position of the sample holder and the electron energy of the sputtergun.

2.6.3 *Evaporation of Molecules*

For S-SHG or SHG-ORD measurements of evaporated molecules the substrate is transferred back into the transfer chamber after the sputtering process. It is then moved above the evaporator. The deposition current is recorded by the QMB before and after evaporation as described in Section 2.3.2. After evaporation the substrate is transferred back into the UHV chamber where the S-SHG and SHG-ORD measurements are performed.

2.6.4 *Cluster Deposition*

For the deposition of size-selected clusters onto the substrate, the cluster current must first be optimized. The clusters are therefore deposited onto a conducting (metal) target which is connected to a picoamperemeter (Keithley, 6517A). The cluster current is monitored whilst the applied voltages of the Einzel lenses as well as the voltages of the QMS are optimized for the specific cluster size of interest. Also, the helium background pressure as well as the opening- and duration-time of the piezo valve at the nozzle are optimized. For unselected clusters the optimization process is equivalent.

The kinetic energy of unselected clusters ($\mathrm{Ag}_{21,x}$) was measured by retarding field analysis. Here a positive voltage was applied to the metal target which is connected to the picoamperemeter. The cluster current was recorded as a function of applied voltage (see Figure 25). Only masses greater than Ag_{16} pass the QMS (compare ref. [117]). The cluster current is fitted with a sigmoid function and the derivative is taken to determine the kinetic energy distribution. The mean kinetic energy is determined to be $9,95$ eV and the FWHM is $3,62$ V. Therefore even the fastest and smallest clusters possess a kinetic energy of under 1 eV/atom and experiments with a similar cluster source on single crystals show that no fragmentation occurs at these kinetic energies [138, 139].

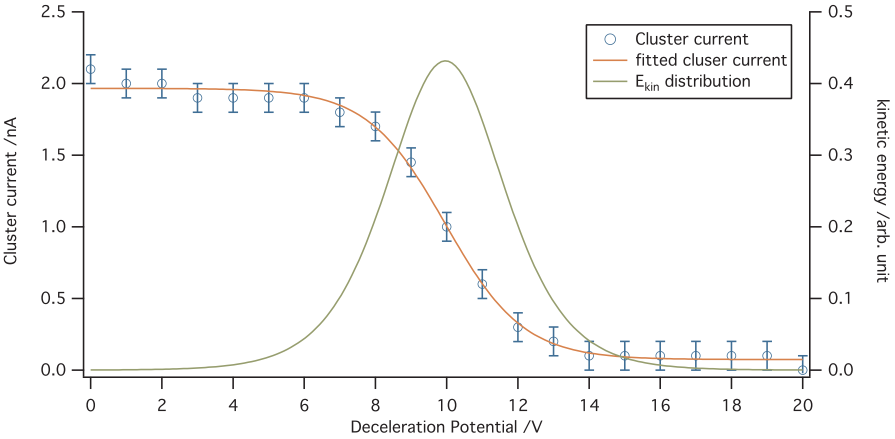

Figure 25: Retarding field analysis for unselected Ag_x clusters measured with the metal plate connected to a picoamperemeter. The cluster current (blue) is measured and an error of $\pm 0,1$ nA is assumed. The kinetic energy distribution, shown in green, is determined by taking the derivative of the fitted cluster current [117].

Once the cluster current is optimized a starting value is recorded before deposition onto the substrate[20]. The electron source is switched on in order to prevent the deposited clusters from charging. For the deposition of unselected clusters, which takes between 2 and 3 hours, the cluster current is recorded every 15 minutes. The coverage after deposition is then calculated with the averaged cluster current.

2.7 DATA TREATMENT

The data treatment is performed after the data are recorded. For an SHG-ORD measurement the recorded polarization data are fitted by a sine-function. The difference in phase between the polarization of

---

[20] Note that the cluster current can not be recorded during deposition because the substrate is not conducting.

the SHG light and p-polarized light then leads to the rotation angle, ϕ, which is the quantity of interest (see Section 1.3).

The data treatment for wavelegth-dependent measurements is of great importance and a sophisticated reference method has to be applied[21]. This is necessary since the obtained raw data are a combination of the spectral response of the sample and the spectral properties of the setup. The latter are given by the dispersive properties of the laser, the detector's sensitivity, and the optical elements within the beam path, (such as Pellin-Broca Prisms, monochromator and PMT, etc.). All these elements lead to an additional wavelength dependency of the measured SH intensity. It is favorable to use the same substrate for the reference measurement as is used as support material for the sample of interest (for better comparability of the two measurements). The data treatment is done using the following method:

Firstly, a S-SHG signal of the pure substrate $I(2\omega)_{BK7}$ is recored and used to obtain a reference spectrum. Oscillations occur in the S-SHG spectrum which are a result of the interference of signals from both sides of the substrate. These oscillations only occur for wavelengths which are not absorbed by the substrate. Afterwards the S-SHG spectrum of supported clusters or adsorbates is recorded. It can be shown that the measured spectra can be expressed as [140]:

$$\frac{\left[\frac{I(2\omega)-I(2\omega)_{BK7}}{I_0^2}\right]_{smooth}}{\left[\frac{I(2\omega)_{BK7}}{I_0^2(1+T^2(2\omega))}\right]_{smooth}} \approx \frac{\left(\chi_S^{(2)}\right)^2}{\left(\chi_{BK7}^{(2)}\right)^2} + 2\frac{\chi_S^{(2)}}{\chi_{BK7}^{(2)}}\cos(\phi) \tag{63}$$

Here, $I(2\omega)$ is the SHG signal's intensity from the supported clusters or adsorbates, $I(2\omega)_{BK7}$ the pure substrate's intensity, I_0^2 the fundamental laser light' intensity and $T^2(2\omega)$ is the transparency function of the substrate[22]. $\chi_S^{(2)}$ denotes the nonlinear susceptibility of the investigated adsorbates and $\chi_{BK7}^{(2)}$ the nonlinear susceptibility of the support material. ϕ describes a possible phase shift between the SH contribution of the adsorbates and that of the reverse side of the substrate. For the usual case that $\chi_{BK7}^{(2)} \ll \chi_S^{(2)}$ (valid if resonances of adsorbates are probed) the equation can further be simplified to:

$$\frac{\left[\frac{I(2\omega)_S-I(2\omega)_{BK7}}{I_0^2}\right]_{smooth}}{\left[\frac{I(2\omega)_{BK7}}{I_0^2(1+T^2(2\omega))}\right]_{smooth}} \approx \frac{\left(\chi_S^{(2)}\right)^2}{\left(\chi_{BK7}^{(2)}\right)^2} \tag{64}$$

---

[21] The data treatment, which is described in this section, has been published previously and can be found in great detail there [140]. Thus, only a short summary is given here.

[22] The transparency function of the substrate can be measured by a commercial UV-Vis spectrometer.

$\chi^{(2)}_{BK7}$ can be regarded as nearly constant over the applied wavelength range, thus the upper term is proportional to $\left(\chi^{(2)}_{S}\right)^2$ which is the quantity of interest.

In Figure 26 an example of the data treatment is shown for evaporated Binol molecules. The raw spectrum, the power corrected spectrum as well as the final spectrum are depicted. The good agreement between the measured spectrum and a spectrum of Binol on quartz glass (measured by a commercial UV-Vis spectrometer) confirms the strength of this data treatment method. Another example of the data treatment for supported silver clusters is given in Section C.1.1.

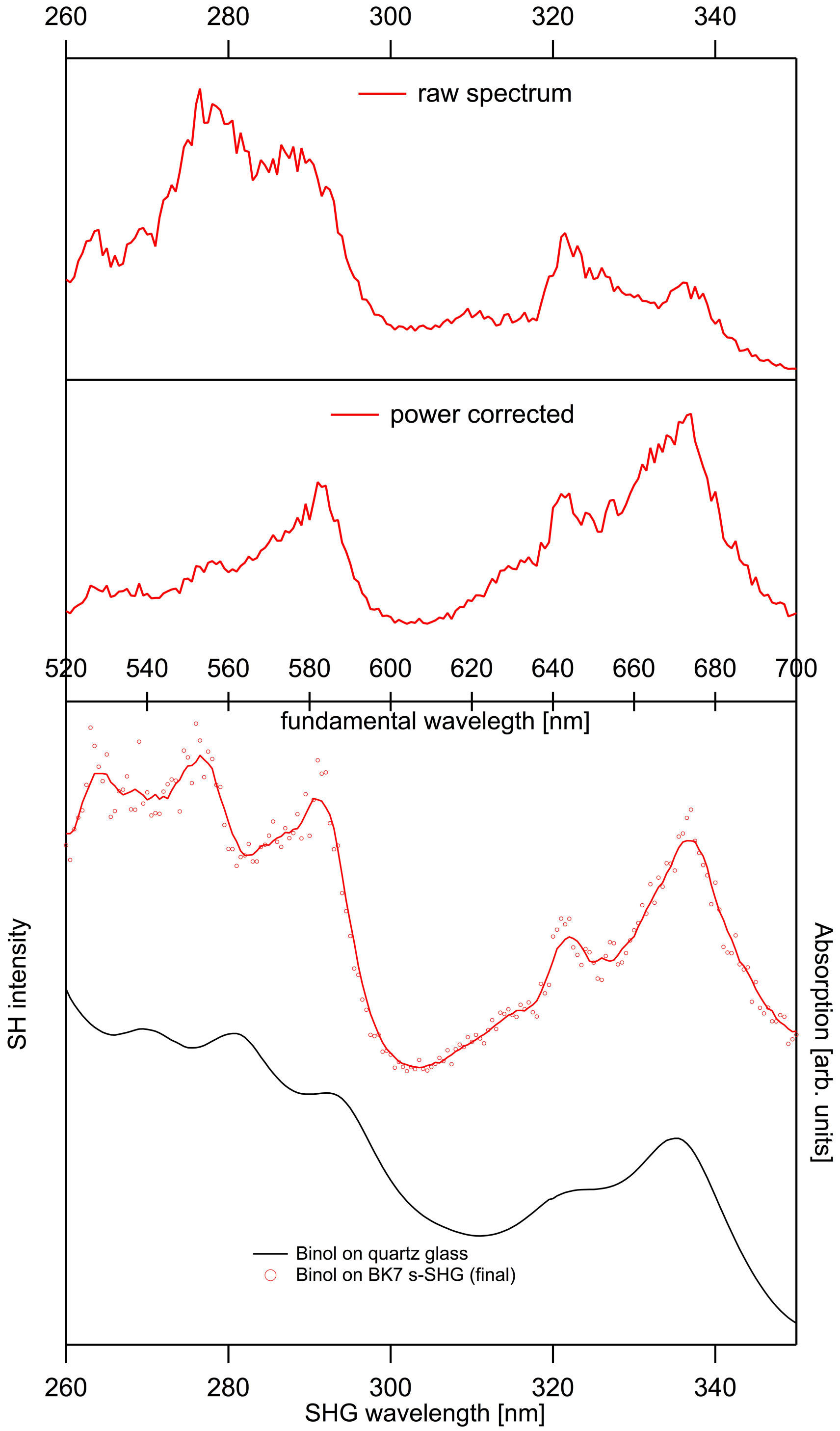

Figure 26: Example of the data treatment for evaporated Binol molecules. The upper panel shows the raw data before any data treatment. The middle panel shows the same data after laser power correction. In the lower panel the red solid curve shows the data after full data treatment including spectrometer function correction. Red circles indicate single data points. The black curve represents the linear absorption spectrum of Binol on quartz glass measured by a commercial UV–Vis spectrometer.

Part IV

RESULTS

3

SUPPORTED CHIRAL BINOL MOLECULES

In this chapter nonlinear spectra of well defined thin molecular films of 2, 2′-dihydroxy-1, 1′binaphthyl (Binol) molecules are shown. They were investigated at coverages between $5 \cdot 10^{15}$ molecules/cm^2 and $5 \cdot 10^{17}$ molecules/cm^2 on thin glass substrates (BK7) under ultra-high-vacuum (UHV) conditions. Second-Harmonic-Generation Optical-Rotatory-Dispersion measurements (SHG-ORD) were performed by using the new spectroscopic setup described in the previous Chapter 2. This allowed for the determination of the rotation angle of the SH-signal of two enantiomers with high chiroptical sensitivity. Coverage dependent orientation evolution of Binol molecular films were revealed by precise monitoring of the surface coverage while performing SHG-ORD experiments[1].

3.1 BINOL

The enantiomeric atropisomers of 2, 2′-dihydroxy-1, 1′ binaphthyl (Binol) are widely used ligands for both stoichiometric and catalytic asymmetric reactions [142]. Binol has also often been used as a chiral probe molecule on surfaces [66, 67, 143, 144]. Furthermore it was indeed shown that nonlinear effects of Binol are dominated by electric dipole transitions [64]. This is typical for those molecules, which are composed of two identical components, spatially arranged in a non-mirror symmetric configuration [50]. In the following the focus is on the second order nonlinear process within the electric dipole approximation (see Section 1.1). This simplifies the theoretical description to a great extent by neglecting magnetic contributions. However, it should be pointed out that this assumption is not valid for all chiral molecules [65, 145, 146]. As described in Section 1.3, SHG-ORD is a very powerful and sensitive tool to probe chiral adsorbates on surfaces. The whole spectroscopic setup was built to perform SHG-ORD measurements, as described in Section 2.5.1. For the following presented data of supported chiral Binol molecules two different geometric alignments and according transmission modes were used (A: substrate/molecules and B: molecules/substrate)[2]. In order to understand the behavior of the SHG-ORD effect and the sign of the rotation angle, ϕ, a deeper look into the properties of the nonlinear susceptibility $\chi^{(2)}$ for different orientations in respect to the propagating electric field (two transmission modes) is useful. As was shown in Section

---

[1] A summary of the following presented results has been published [141].

[2] Compare Figure 10 and Figure 27.

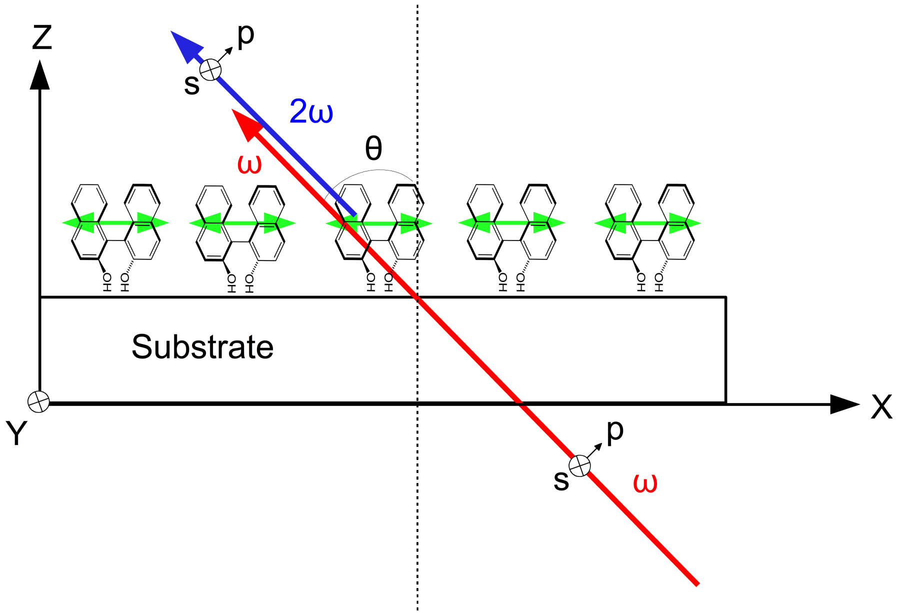

Figure 27: The coordinate system used. Here only transmission mode (A) is shown and molecules are assumed to be oriented with their hydroxyl groups towards the surface. The substrate is exposed by the fundamental light (red) with an incident angle θ. The dipole moment for the transition at 337 nm is drawn in green, the emitted SHG light marked in blue.

1.4.2 changing transmission modus leads to a change in sign for the achiral tensor elements χ_1, χ_2, χ_3, whereas the chiral tensor element χ_4 remains constant. Interchanging enantiomers however, only affects the chiral tensor element and changes its sign ($\chi_4 \rightarrow -\chi_4$). Hence it is important to note, that in an SHG-ORD experiment the rotation angle, ϕ, changes sign, whenever the chirality or the used transmission modus changes. This is always true for samples with in-plane isotropy, independent of the orientation of the molecules.

In Figure 27 the coordinate system of transmission mode A is depicted. The molecules are assumed to be oriented with their hydroxyl groups towards the surface. The molecules are exposed by the pulse of the ps-laser with a fundamental wavelength of 674 nm and embedded in an anharmonic potential. Thus, they emit light with double energy (337 nm) marked in blue.

3.1.1 *SHG-Spectrum*

In the first performed experiments a S-SHG spectrum as well as an incident angle dependent measurement of evaporated racemic Binol molecules were recorded. These measurements led to important insights in order to understand the later presented data.

3.1.1.1 *Wavelength Dependency*

In Figure 28 a SHG-spectrum of Binol molecules evaporated onto BK7 glass is shown[3]. The spectrum was recorded as described in Section 2.6. No shift of the investigated resonance (337 nm) was observed for different coverages. All of the following SHG-ORD measurements were performed at a resonance wavelength of 337 nm (674 nm fundamental wavelength, marked in blue).

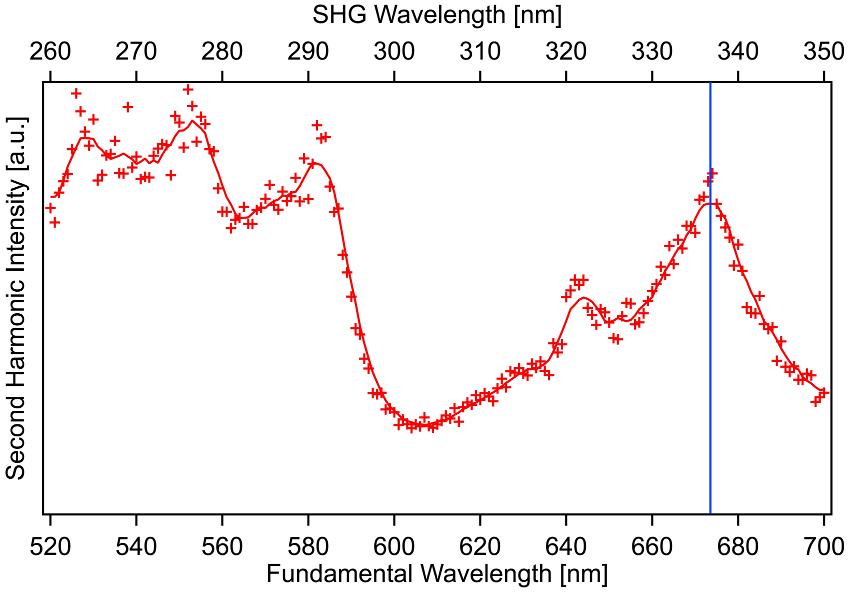

Figure 28: SHG spectrum of evaporated Binol molecules on BK7. Compare Figure 26. The SHG-ORD measurements were performed at fundamental wavelength of 674 nm (marked in blue).

3.1.1.2 *Incident Angle Dependence*

In a second measurement the S-SHG signal from the bare BK7 substrate is recorded as a function of the incident angle at 674 nm fundamental wavelength as shown in Figure 29. Therefore, interference of the SHG signal from front- and backside of the substrate occurs and can be observed (see Section 2.7) [140]. Incident angles of destructive interference slightly shift for different substrates due to slight misalignments of the substrate in the substrate holder (see Section 2.6.2) and due to differences in thickness at different positions on the substrate. For simplicity a polarization scan of the SHG signal of the pure substrate is taken at an angle of constructive interference to define the 0° polarization angle (p-polarization) of the SHG light (there is no SHG-ORD effect of BK7). Note, that racemic Binol showed, as expected, the same results. Afterwards, the substrate is taken into the transfer chamber where enantiomerically pure Binol is evaporated

---

[3] This spectrum was already shown in Figure 26 as a result of the data treatment.

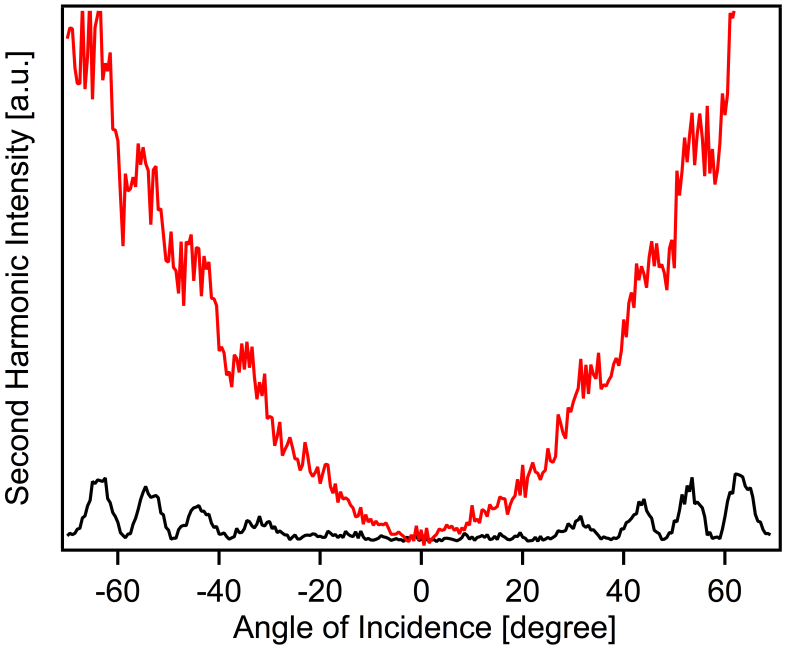

Figure 29: Incident angle measurement for both: pure BK7 substrate (black) and BK7 with Binol molecules (red). No signal was measured at normal incidence.

onto its cooled surface. After evaporation the substrate is transferred back into the UHV chamber and an additional incident angle dependent measurement is performed. The result is depicted in Figure 29. Two points should be mentioned here. First, since only the orthogonal part of the oscillation with respect to the substrate surface is SHG active and the parallel oscillation remains SHG inactive there is no signal at normal incidence. The absence of SHG signal at normal incidence indicates that there are no measurable contributions from the bulk, both for the substrate and for the molecular film [140]. Second, the incident angle scan of the sample with the evaporated molecules additionally shows the interference pattern from the bare substrate. Consequently, great care must be taken to measure polarization scans at angles of destructive interference of the bare substrate in order to suppress any residual SHG light from the pure substrate. At cooled UHV conditions no electric dipole moment orthogonal to the surface is probed, thus molecules do not contribute to the SHG signal. At ambient conditions and room temperature however, molecules form crystal-like structures which lead to a distinct SHG signal at 0 degree[4].

---

[4] Warm (room temperature) Binol samples showed self-assembling effects and formed a crystal-like structures. Interestingly, racemic Binol and enantiomeric pure Binol looked different under the microscope. In ref. [129] two examples of evaporated Binol are shown. The molecules were evaporated on a cooled BK7 substrate under HV conditions and allowed to warm up over a time period of approximatly 12 hours.

3.1.2 *SHG-ORD Measurements*

After the performed S-SHG and incident angle-dependent measurements the fresnel rhomb (with it's corresponding polarization filter) is appended into the spectroscopic setup in order to peform chiroptical (SHG-ORD) measurements at 674 nm fundamental wavelength (see Section 2.5).

3.1.2.1 *Polarization Scans*

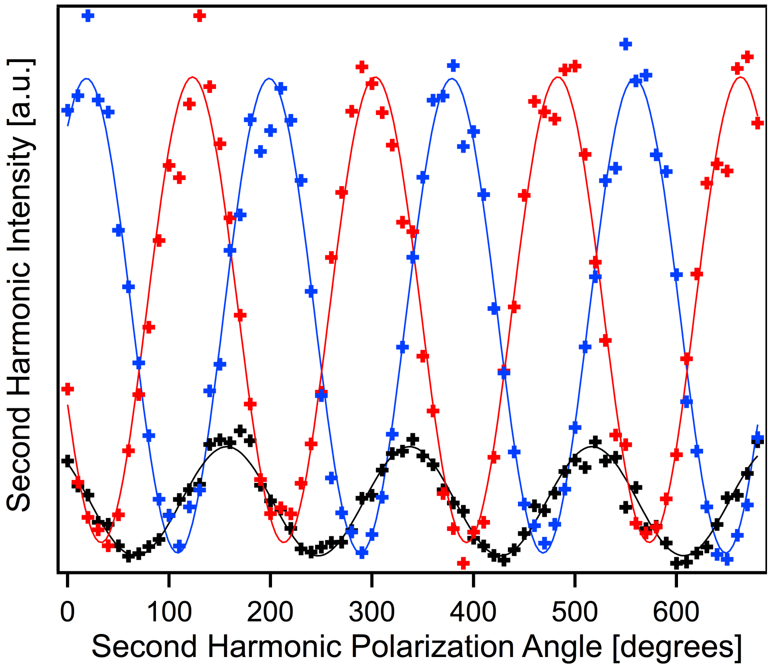

Figure 30: R-Binol (red) and S-Binol (blue) polarization scan and sine-fit. The reference signal is given by the BK7 substrate (black) and thus defines p-polarized light (see text).

The incident angle dependent measurements of thin molecular films of Binol were performed at incident angles of destructive interference[5]. First, both enantiomers were evaporated (with the same coverage) and polarization scans were performed at different incident angles consecutively as described in Section 2.6. The results of an incident angle of approximately 35 degrees are depicted in Figure 30. The second harmonic intensity of both enantiomers is plotted

---

They were afterwards investigated by a commercial microscope under ambient contitions.

The results from a cooperation with Prof. T. Verbiest's group are shown ref. [147]. SHG-microscopy has recently been proposed to determine the point group symmetry of noncentrosymmetric samples [148, 149]. This procedure has been used to extract symmetry information of the investigated crystalized 2, 2′-dihydroxy-1, 1′-binaphthyl films.

[5] An incident angle of constructive interference was taken for the spectra of the pure substrate, in order to gain a p-polarized signal.

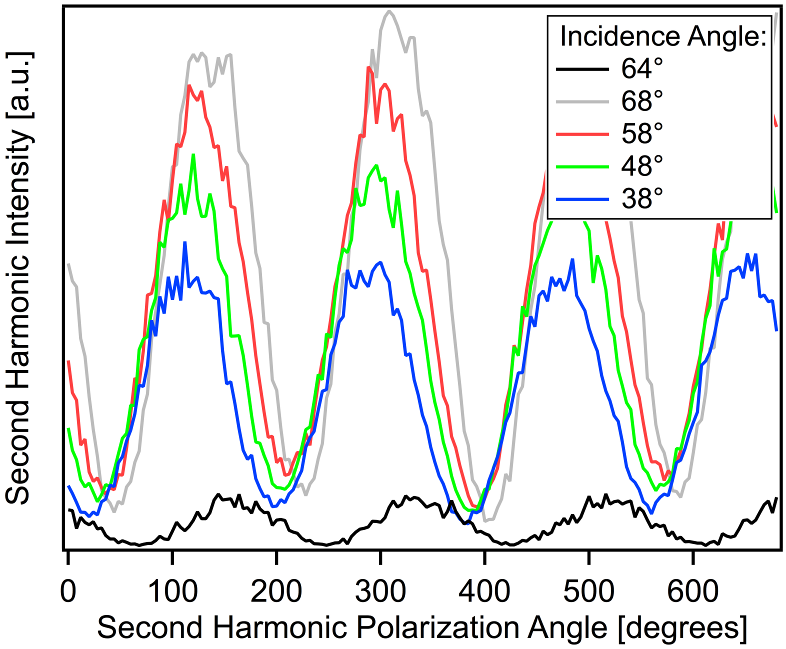

Figure 31: Polarization scans of R-Binol for transmission mode A for different incident angles (see text). The black graph originates from the bare BK7-substrate.

as a function of polarization angle. This SHG-ORD spectrum of the R-Binol and S-Binol enantiomers is marked in blue and red respectively. The reference signal from the pure substrate is also plotted and marked in black. It defines p-polarized light. It can be seen that the phase shift[6] (ca. 33 degrees) is symmetric for both enantiomers which is a strong indication of randomly oriented molecules on the surface (with in-plane isotropy). All results were stable over time and do not appear to be influenced by the laser; neither photobleaching nor photo-degradation could be observed. The measured data are fitted by a sine function (red and blue) and the difference in phase to p-polarized light (black) gives the polarization angle ϕ. The results are well matched by the sinus fit. This reveals the great accuracy of the implemented spectroscopic setup. The big advantage of the use of a Fresnel rhomb in combination with a polarization filter can also be seen here. Possible misalignments of the optical elements within the light pass are compensated by the 680 degree rotation of the polarized SHG signal (see Section 2.5).

Best results were obtained by rotating the Fresnel rhomb over 340°, as shown in Figure 30. Reproducing the results led to an error of rotation angle of less than 2°. The phase difference between the R- and S- enantiomers shows values of up to $(75 \pm 2)^\circ$ at 674 nm. This is

---

[6] The phase shift is the difference in polarization angle, hence the difference between the fit-maxima of R-Binol or S-Binol with respect to p-polarized light, marked in black.

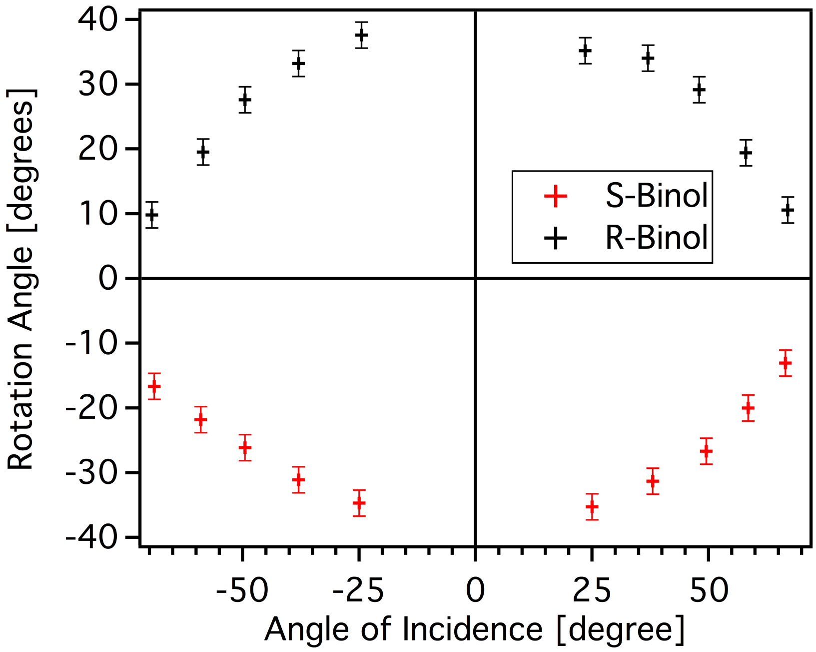

Figure 32: Rotation angle for transmission mode A at different incident angles (see text).

a remarkably high value and thus already shows the high chiroptical sensitivity of this nonlinear technique.

In Figure 31 4 polarization scans of evaporated R-Binol films at different incident angles are shown. The incident angles with their corresponding colors are shown in the inset of the graph. For a better comparison the signal of the bare substrate is also plotted and marked in black. It was taken at an incident angle (64 degrees) of constructive interference in order to define p-polarized light. Two effects can be observed for the signal of molecular film of R-Binol with increasing incident angle. First, the overall SHG intensity increases. This is due to the incident angle dependency of the SHG signal (see Equation 26). Second, the phase difference between the p-polarized reference signal (black) and the measured SHG signal of the molecules (rotation angle ϕ) decreases. This is in perfect agreement with theory. The rotation angle, ϕ, depends on the incident angle, θ, by[7]:

$$\phi = \tan^{-1}\left(\frac{f_s}{f_p}\right) = \tan^{-1}\left(\frac{2\chi_4 \cos\theta}{\chi_1 \sin^2\theta + (\chi_2 + 2\chi_3)\cos^2\theta}\right) \tag{65}$$

Thus, an increase of the angle of incidence, θ, leads to a decrease of the rotation angle, ϕ, of the enantio-pure molecular film. An important effect of SHG-ORD measurements can be observed here: In order to gain a good signal to noise ratio of the rotation angle one must balance the SHG signal's intensity $I(2\omega)$ versus the magnitude

---

[7] Compare Equation 38.

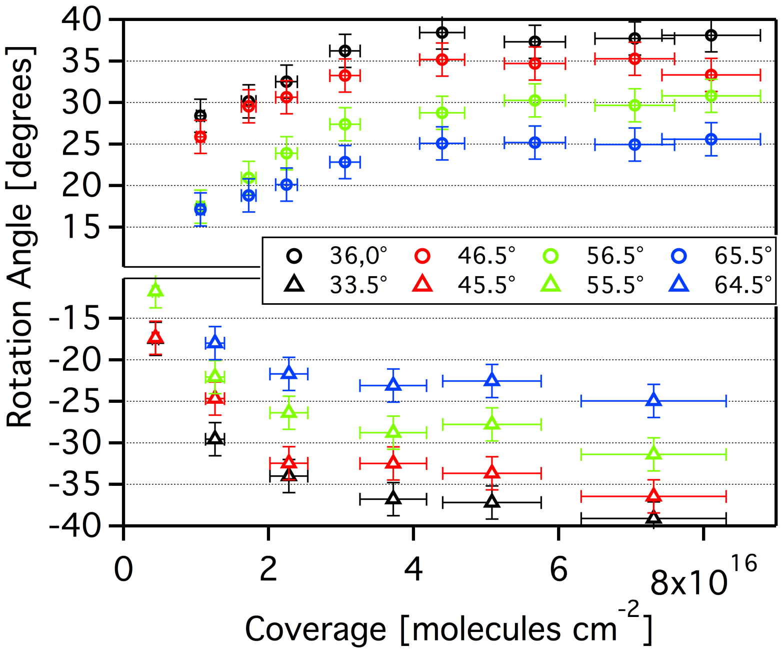

Figure 33: Rotation angle of S-Binol as a function of coverage for different incident angles at 674 nm. Transmission mode B (positive values) as well as transmission mode A (negative values) are shown. A clear increase of the rotation angle as well as a saturation at approximatly $5 \cdot 10^{16}$ molecules/cm^2 can be observed.

of the rotation angle ϕ. Small angle of incidence lead to high rotation angles but small SHG intensities $I(2\omega)$, whereas big angle of incidence lead to small rotation angles, ϕ, but high SHG intensities $I(2\omega)$.

The rotation angle for different incident angles and both enantiomers (with the same coverage) are presented in Figure 32 (for transmission mode A). The rotation angles were measured at incident angles of destructive interference as described in Section 3.1.2.1. The high quality of the measurements is confirmed by the completely symmetric appearance of the rotation angles for the two enantiomers. Positive and negative angles of incidents lead to the same rotation angle, whereas the sign of the rotation angle changes for different enantiomers. Looking at Equation 65 it can be seen that both results are in perfect agreement with theory. Interchanging the enantiomers leads to a change of the sign of the chiral tensor component, χ_4, and henceforth to a change of sign of rotation angle ϕ.

3.1.2.2 *Coverage Dependency*

In the next series of experiments, coverage dependent SHG-ORD measurements of enantio-pure Binol molecular films were performed for both transmission modes mentioned earlier. The evaporation process was monitored by a quartz micro balance described in Section 2.3.2.

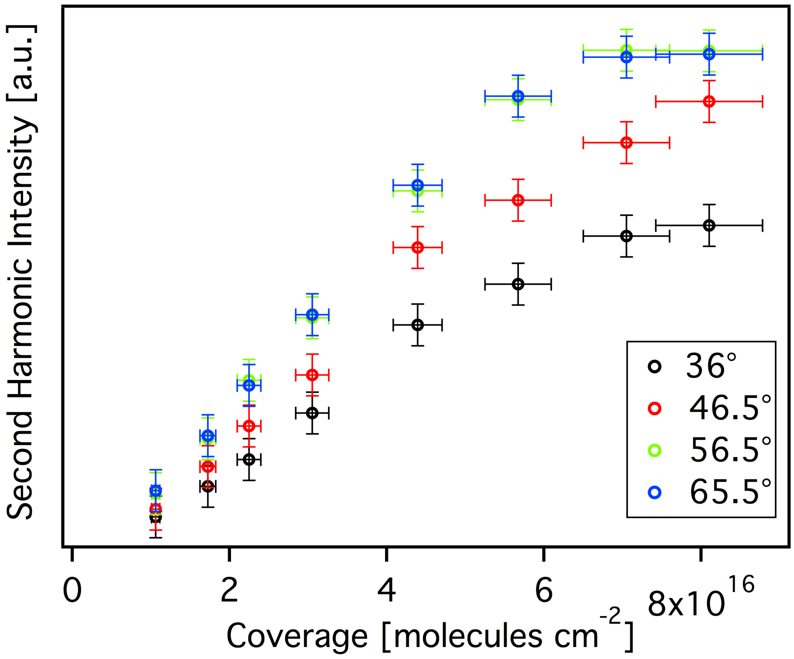

Figure 34: Signal's intensity as a function of coverage for four different angles of incidences (depicted in the inset).

The coverage was afterwards calculated by the Sauerbrey equation (see Equation 61). The results for the rotation angle of S-Binol for different coverages are shown in Figure 33 and Figure 34. The rotation angle varies significantly with the coverage. It increases up to a coverage of approximately $5 \cdot 10^{16}$ molecules/cm^2 and then remains constant.

Taking the amplitude of every fit leads to Figure 34 (for transmission mode B). Here the intensities for different incident angles are plotted as a function of coverage. The higher intensity for a bigger angle of incidence is due to the angle of incidence-dependent SHG signal: $I(2\omega) \sim \sec^2(\theta)$ (compare Equation 25 and 26). A linear increase of the intensity as a function of coverage can be observed. The almost equal intensities for $\theta = 56,5°$ and $\theta = 65,5°$ are of experimental origin[8]. Even at the highest coverage, no signal was observed at an incident angle of 0 degree. Thus, it can be concluded that all molecules contribute to the SHG signal but are randomly oriented with in-plane isotropy. Taking the rotation angle for different incident angles and different coverages, one can estimate the ratio of chiral to achiral tensor components using Equation 65.

---

[8] The same intensities for 56,5 degree and 65,5 are presumably due to the very high angle of incidence of the latter. This high angle presumably leads to a parallel offset of the SHG beam, which decreases the measured intensity. This, however doesn't have any influence on the measured rotation angles and can thus be neglecting when interpreting the measured data.

The calculated data are plotted in Figure 35. It can clearly be seen that the ratio increases with coverage and remains constant at a certain coverage of $5 \cdot 10^{16}$ molecules/cm^2. The reason for this behavior can be attributed to small changes in molecular orientation with increasing surface coverage (see Section 1.4.2). For a SHG signal three conditions must be fulfilled on a molecular level within the electric dipole approximation. First, the energy of the excitation source must be close to the electric dipole transition moment of the molecules. Second, the polarization of the excitation source must match the orientation of the electric dipole transition moment. And third, inversion symmetry must be broken for this transition dipole moment.

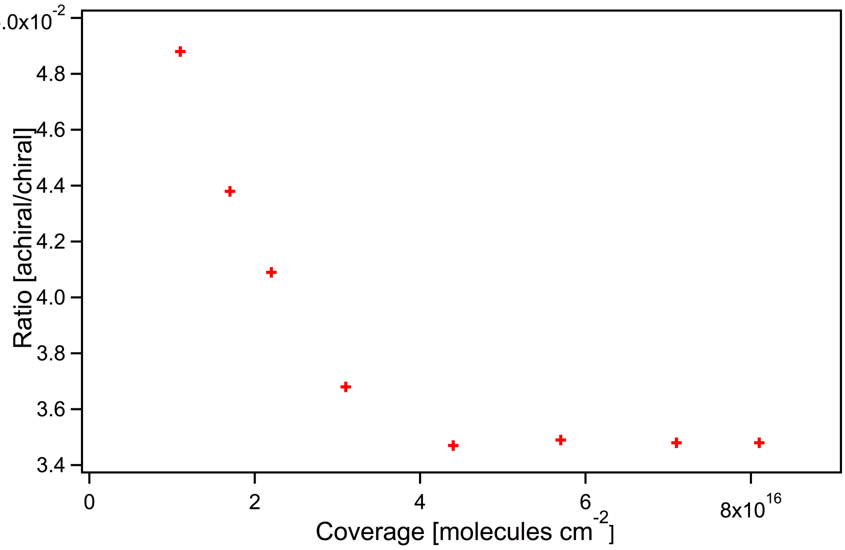

Figure 35: Calculated ratio of achiral to chiral tensor components

3.1.2.3 *Orientation of Molecules on the Surface*

The observed coverage-dependent SHG-ORD behavior can be interpreted as follows. Due to the sample preparation the molecules might adsorb quite strongly (in a covalent fashion), which hinders mobility. The first layer of Binol molecules is probably oriented with the hydroxyl group towards the polar surface of the amorphous BK7 substrate. In this case the electron dipole moment for the transition at 337 nm (674 nm fundamental wavelength) is mainly oriented in the x-y direction parallel to the surface [64]. Therefore, no signal can be observed for this transition since the inversion symmetry is not broken due to the symmetric overall potential. For incident angles unequal to zero however no transition moment perpendicular to the surface can be probed. In conclusion, no signal can be observed for

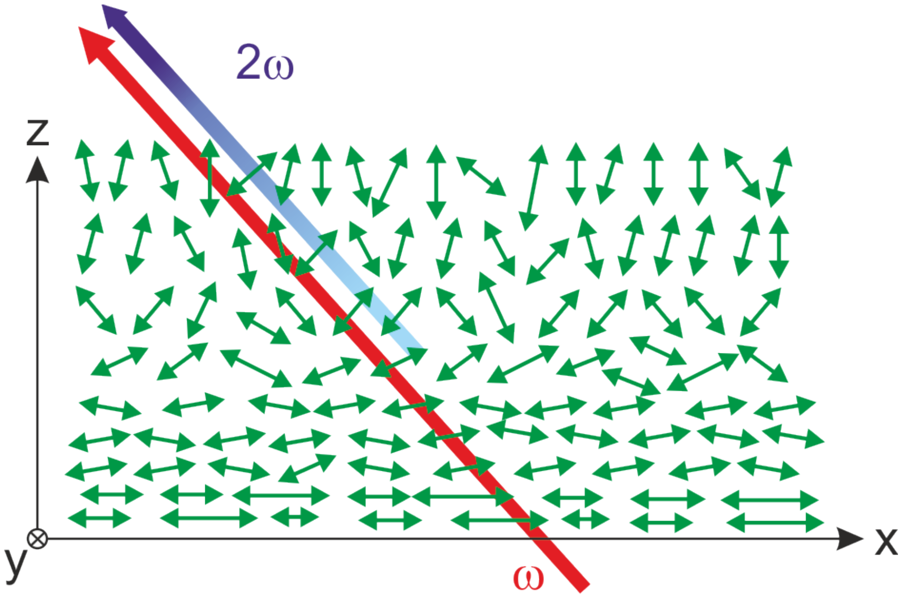

Figure 36: 2-dimensional sketch of the proposed layer model. The dipole moments are oriented parallel to the surface for the first layers. The ordered structure vanishes with increasing coverage.

a small coverage up to approximately $5 \cdot 10^{16}$ molecules/cm^2 [9]. For a higher coverage however the molecules' orientations slightly change and the transition moment at 337 nm can be probed for incident angles unequal to zero. The aforementioned ordered structure for the first layer(s) vanishes with increasing coverage (see Figure 36). Note, that there is always a higher ordered structure towards the surface and a less ordered structure in z-direction for each molecule. Therefore, the molecules are embedded in an anharmonic asymmetric potential in z-direction, which is a crucial condition for the generation of second harmonic light (see Section 1.1.4). The orientation changes by coverage, which leads to an increase of the rotation angle of the SHG-ORD signal until saturation. Because no signal is observed at incident angles of zero degrees, even at highest coverage, in-plane isotropy is still present and there is no bulk contribution to the signal. These results lead to the conclusion that the evaporated Binol molecules reach their final orientation at a coverage above $5 \cdot 10^{16}$ molecules/cm^2. The calculated ratio of f_s to f_p is 0,035 for this coverage.

3.1.3 *Summary and Conlusion*

In this chapter the new experimental and spectroscopic setup was used to investigate the chirality of well-defined molecular films of

---

[9] Assuming Binol molecules of the first layer having a size (projection of the molecules profile onto the surface) of ca. 0,5 nm^2 this film thickness corresponds to ca. 10 monolayers. This is however a raw estimation and strongly depends on the orientation of the molecules.

$2,2'$-dihydroxy-$1,1'$binaphthyl molecules by means of the SHG-ORD effect. The setup allows for the investigation of supported chiral adsorbates on transparent surfaces under UHV condition. Differences in the polarization of up to $\nabla\phi = \phi_R - \phi_S = (75 \pm 2)^\circ$ were measured for different enantiomers and showed the extremely high chiral sensitivity of this nonlinear technique. By reproducing results errors of the rotation angle of less than 2 degree were estimated. The investigated molecules were stable and did not show any self-assembling effects under these conditions. Also, no photo-bleaching or photo-degradation effects could be observed. The shown data strongly confirm the in-plane isotropy for the investigated system of these molecules and thus support the validity of the chosen theoretical description. The rotation angle changes dramatically with coverage until saturation. This behavior was attributed to orientational effects, thus the origin of this effect lies in the different orientations of the molecules' hyperpolarizability $\alpha^{(2)}$ for different coverages. It could be shown, that coverage dependent measurements are crucial in order to understand the chiroptical response of molecular films. The data indicate that the molecules reach their final orientation at approximately $5 \cdot 10^{16}$ molecules/cm^2. The ratio of chiral to achiral tensor components could be calculated and showed to change with coverage.

This observation is extremely important for possible further investigation of molecular films, especially when used as basis for the preparation of chiral metal clusters.

4

SUPPORTED AG-CLUSTERS

In this chapter nonlinear spectra of supported size-selected silver clusters are introduced. Firstly, the spectra of supported unselected (Ag_x) clusters are shown and discussed. The coverage (clusters/cm^2) is calculated and coverage-dependent S-SHG measurements are introduced and interpreted. Secondly, nonlinear spectra of supported size-selected silver clusters (Ag_{15} to Ag_{55}) are presented. The optical properties are interpreted and compared to other publications, both experimental and theoretical. The resonance of the clusters show a distinct blue shift with decreasing cluster size, which is a new finding for supported silver clusters in this size regime. It will be shown, that this in good agreement with other publications of free silver clusters or silver clusters embedded in matrices and can be interpreted by quantum size effects.

In the last part of this chapter the reactions of supported clusters (both unselected and selected) with background gases is detailed. S-SHG spectroscopy is shown to be a highly sensitive method for the investigation of potential reactions, such as oxidation, of supported clusters by other background gases. Here, the focus is on oxygen. However, argon, helium, and hydrogen were also investigated. Possible interpretations of the presented results are given. At the end a conclusion of the spectra shown in this chapter is given leading to a recommendation of possible future measurements.

4.1 UNSELECTED AG-CLUSTERS

The first series of measurements was performed with supported unselected[1] silver clusters (Ag_x). This was the first approach to the investigation of supported size-selected silver clusters because it simplified the executed measurements to a great extent. The deposition, spectroscopic investigation and subsequent data treatment were performed as described in detail in Section 2.6. The cluster currents of unselected clusters are in the range of $2\,\mathrm{nA} - 5\,\mathrm{nA}$ which reduces the deposition time by a factor of ~ 100 compared to size-selected clusters (see following Section 4.2). Also, other values of interest, e.g. the distribution of the deposited clusters or the influence of the coverage on the spectra can easily be determined. These values should not change with cluster size. Therefore, spectra of unselected clusters are of great importance and lead to a better understanding of the investigated system.

---

[1] See Section 2.4.1.

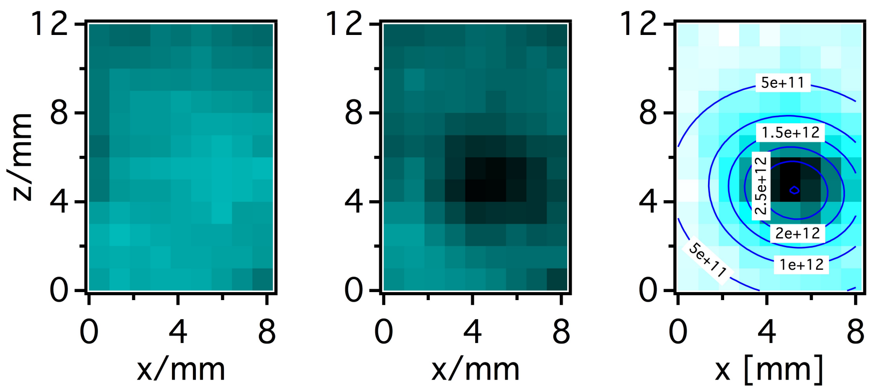

Figure 37: Cavity ring-down mapping of a sample with clusters. A raster for different x (width) and z (hight) positions was measured. The scattering and absorption losses of the bare substrate and the substrate after deposition are shown on the left and in the middle, respectively. The difference of both measurements is shown on the right. The absorption scale goes from 0 ppm (white) to 2500 ppm (black). The cluster spot and its gaussian distribution is well resolved and fitted by a two dimensional gaussian distribution. The corresponding coverage is marked [77].

4.1.1 *Determination of the Coverage*

In order to determine the coverage distribution of supported unselected silver clusters linear absorption measurements were performed [77]. Cavity ring-down spectroscopy was applied to detect the very weak signal of the sample[2]. A surface mapping was performed at 450 nm[3]. First, the losses of the bare substrate (at Brewster's angle) were measured at different positions. This led to the surface mapping shown in Figure 37. Then, unselected clusters were deposited and afterwards a second mapping of the substrate with the clusters was performed. Subtracting the losses of the bare substrate from the losses of the substrate with the clusters led to the distribution of the clusters on the surface, also depicted in Figure 37.

It can be seen, that the deposited clusters have a gaussian distribution. $1 \cdot 10^{12}$ clusters were deposited. The value of the coverage in the middle of the spot is ca. $3 \cdot 10^{12}$ clusters/cm^2. Thus, the coverage in the middle of the spot can be evaluated by multiplying the amount of deposited clusters by a factor of three. This has been done for all following presented spectra. For the unselected clusters a mean clus-

---

[2] Cavity ring-down spectroscopy is a highly sensitive linear absorption spectroscopic method. It is a superior technique for absorption measurements of gases or supported clusters under UHV conditions. A description of the used spectroscopic setup as well as of the associated theory would be beyond the scope of this thesis. It can be found in ref. [29, 150, 25, 82] in great detail.

[3] This wavelength is a good compromise between high linear absorption cross section and scattering losses due of the substrate. See ref. [82].

tersize of $\sim 1,5$ nm is estimated [82]. One monolayer is defined as a surface fully covered with clusters. Then $3 \cdot 10^{12}$ clusters/cm^2 in the middle of the spot correspond to ca. $0,05$ monolayers. This resolution shows the high sensitivity of this linear absorption technique.

4.1.2 *S-SHG Spectrum*

The first nonlinear spectra were collected from unselected supported silver clusters measured by the OPA laser system at Brewster's angle and low temperature (see Section 2). The QMS was operated in RF-only mode (see Section 2.4.1) at a cluster size of Ag_{35}[4]. The size distribution (see Section 2.4.1) of the deposited clusters is estimated to be 55 ± 25, leading to an average cluster diameter of approximately $1,5$ nm. This rough estimation is performed by looking at the mass spectrum of the deposited clusters for the RF-only mode (see Section 2.4.1). The coverage was approximately $6 \cdot 10^{12}$ clusters/cm^2. The result of the measurement is depicted in Figure 38[5]. It can be seen that the applied S-SHG spectroscopy technique is sensitive enough to probe adsorbates of sizes of $\sim 1,5$ nm and coverages of $6 \cdot 10^{12}$ clusters/cm^2. The gap in the spectra between $3,35$ eV (740 nm fundamental wavelength) and $3,64$ eV (680 nm fundamental wavelength) is due to the lasersystem (refer to Section B for a detailed description). The gap leads to inaccuracy in the measured data for the resonance to some extent, however a resonance peak is still well resolved. The spectrum is superimposed on the oscillations of the pure substrate[6]. It is fitted by a lorentzian curve in order to guide the eye and receive a value for the peak position of the spectrum. In this case the peak is located at $(3,76 \pm 0,05)$ eV.

As described in Section 1.1.4 the nonlinear spectrum contains resonance peaks whenever either the fundamental or the second harmonic frequency matches an optical transition of the investigated sample. By comparing linear (cavity ring-down) and nonlinear (S-SHG) spectra it could be shown that the spectrum can undoubtedly be assigned to the the second case [82][7]. Thus, this peak at $(3,76 \pm 0,05)$ eV originates from the resonance of the silver plasmon. For this size distribution the peak maximum can be assigned to a collective oscillation of the 5s electrons. Note, that only the plasmon mode perpendicular to the surface is probed (see Section 1.5.3.5).

On the higher energy side the spectrum does not go to zero, but remains at a certain level. This is expected by theory and can be attributed to inter-band transitions of silver, described in detail in

---

[4] $35 \cdot 107,686\,\text{amu} = 3769$ amu.

[5] The raw data treatment can be found in Section 2.7 and Section C.1.1.

[6] Refer to Section 2.7 for a more detailed description.

[7] These spectra were measured with the same experimental setup but with a different laser system. The technique as well as the spectra are well described in ref. [25, 150, 82].

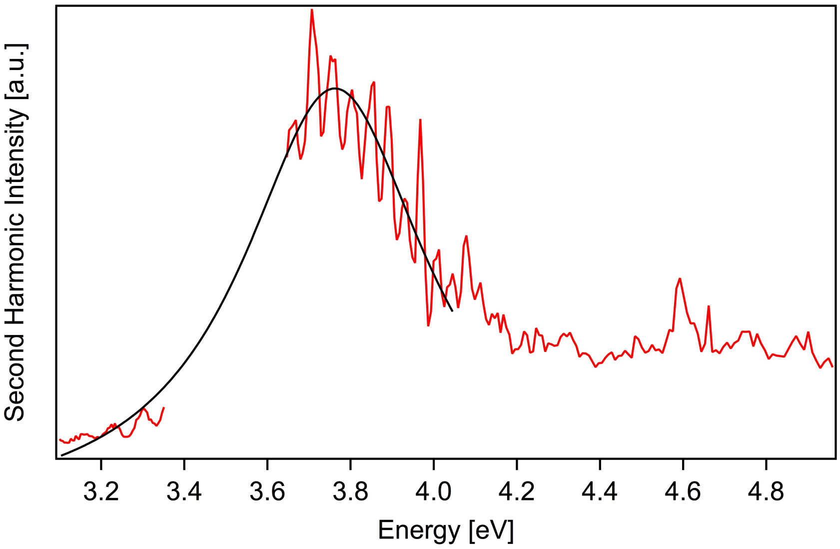

Figure 38: S-SHG spectrum from unselected silver clusters Ag_x. The data are fitted by a lorentzian curve (see text).

Section 1.5.3. The measured peak position is in good agreement to other publications e.g. by Nilius et al. They investigated supported silver nanoparticles from 12 nm down to $1,5$ nm by means of photo emission spectroscopy under UHV conditions [39][8]. They estimated a rescaled[9] peak position of $3,75 \pm 0,50$ eV[10] for this size which matches the measured value of $(3,76 \pm 0,05)$ eV within the experimental errors. However, it should be noted that the peak position and the cluster size of the data from Nilius et al. are arguable. The size was estimated by STM images. Thus, the size distribution for unselected clusters is presumably smaller and better defined than for supported nanoparticles of an STM image. Also, the influence of the tip led to a potential blue shift of the measured peak positions which is in fact subtracted for the scaled data but is hence a further disturbance of the investigated system.

4.1.3 *Coverage Dependency of S-SHG Resonance*

In the next step coverage-dependent measurements were performed. Here, a special interest lay on possible cluster-cluster interactions and how these might influence the measured spectra. There are two possible ways to perform coverage-dependent measurements. First, a very

---

[8] Photo emission of oxide-supported silver clusters was stimulated by the field emission current of a STM, using the tip as a local electron emitter.

[9] The data are rescaled towards the classical Mie limit for better comparison (see Section 4.2.2).

[10] The measured data are corrected by a factor of $0,15$ eV which will be explained in Section 4.2.2.

high coverage (about one monolayer in the cluster spot) is deposited and subsequently S-SHG spectra are recorded for different positions on the substrate; starting from the position with the highest coverage, thus the biggest signal to positions with lower coverage. As the distribution of clusters is approximately of gaussian character (see Section 4.1.1) the coverage at every position can be estimated. This is however only a rough estimation. The second approach is to measure a spectrum after a short deposition and subsequently do another deposition on the same cluster spot and so forth. This approach was chosen here because it leads to more accurate coverages. However, both approaches are constructive as shown in ref. [77].

Unselected Ag_{35} clusters were deposited and spectra were measured for different coverages. Some of the measured spectra are shown in Figure 39[11].

The spectra were fitted by a lorentzian function. The peak maxima of the fit are plotted as a function of coverage in Figure 40. A blue line is also plotted to guide the eye. Some interesting findings can be observed here. The position of the spectral maxima does not change with coverage until a value of approximately $(15 \pm 3) \cdot 10^{12}$ clusters/cm^2. Assuming a cluster size of approximately $1,75$ nm^2 on average, this coverage corresponds to $0,25\%$ of a monolayer. For higher coverages a distinct red shift can be observed. At approximately $60 \cdot 10^{12}$ clusters/cm^2 one monolayer of silver would be reached. The observed red shift might have a number of different origins. In Section 1.5.3.5 different physical effects of supported clusters were discussed. Because the aforementioned red shift corresponds to an increase in coverage, the origin of this effect might be due to the interactions of the supported clusters. For plasmon excitation perpendicular to the surface (which is the case here) possible dipole-dipole interactions of neighboring clusters lead to a potential blue shift [98, 86, 96, 95]. This effect is not observed here but was shown for gold nanoparticles with large diameters (~ 150 nm). Obviously the dipole-dipole interaction of neighboring supported clusters is not the main reason for the observed shift, or at least does not influence the spectra in the expected way. It should depend upon and decrease with decreasing sizes, because the overall dipole interaction decreases. Thus, it might be too small to be observed. A more constructive explanation for the observed red shift with increasing coverage is the coalescence of the clusters leading to bigger cluster sizes. At a coverage of approximately $0,25$ monolayers, the probability of coalescence for further deposition is $\sim 25\,\%$. The cluster sizes will broaden leading to nanoparticles with diameters of a few nm. These clusters are known to show a distinct red shift for increasing cluster size, which has been

---

[11] In order to guarantee a proper presentation, only a few spectra are shown here. The rest of the measured data can be found in C.1.2.

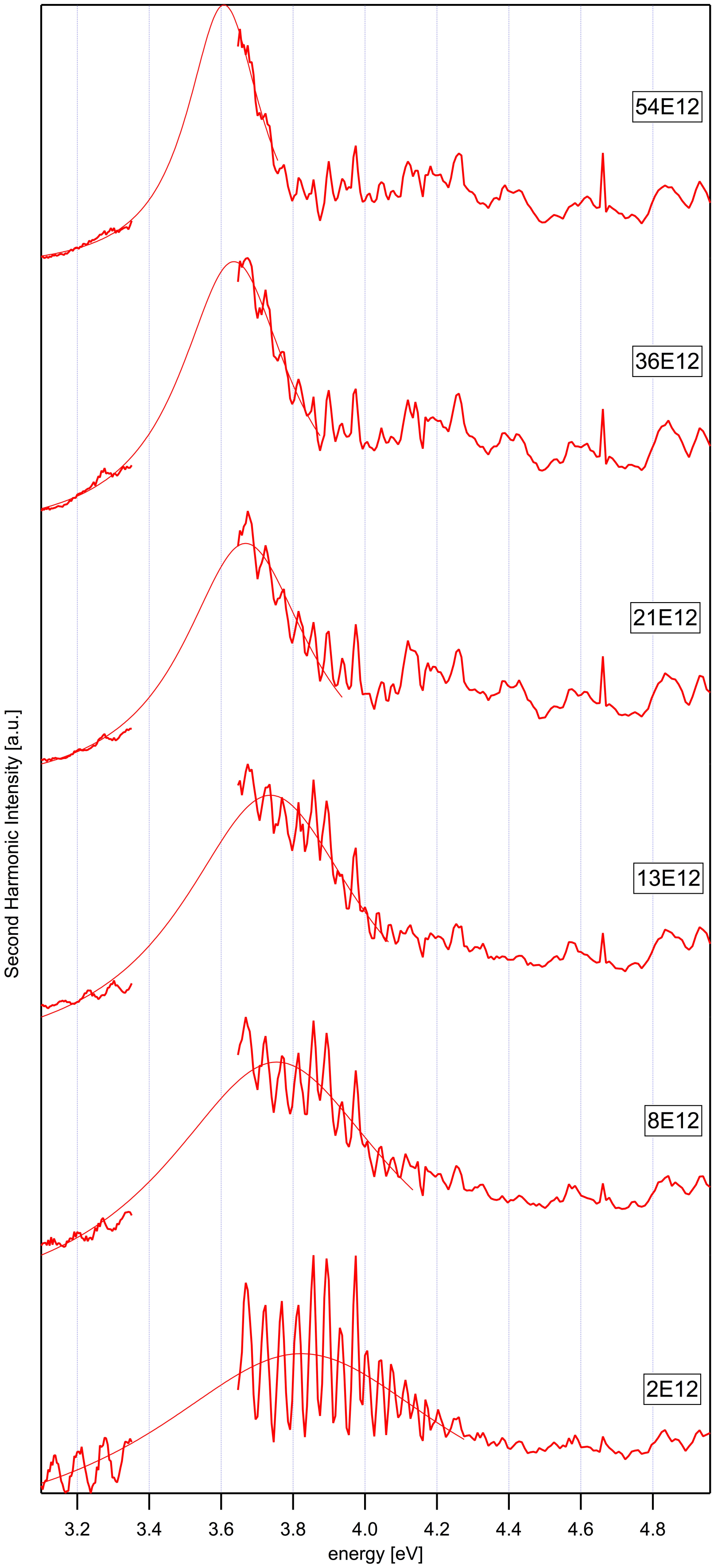

Figure 39: Spectra of unselected Ag_{35} clusters at different coverages.

observed in literature [39, 151] and can be attributed to quantum size effects (see next Section 1.5.3.7).

The observed red shift with increasing coverage can thus presumably be interpreted as a red shift due to increasing particle diameter. This interpretation is supported by further observations.

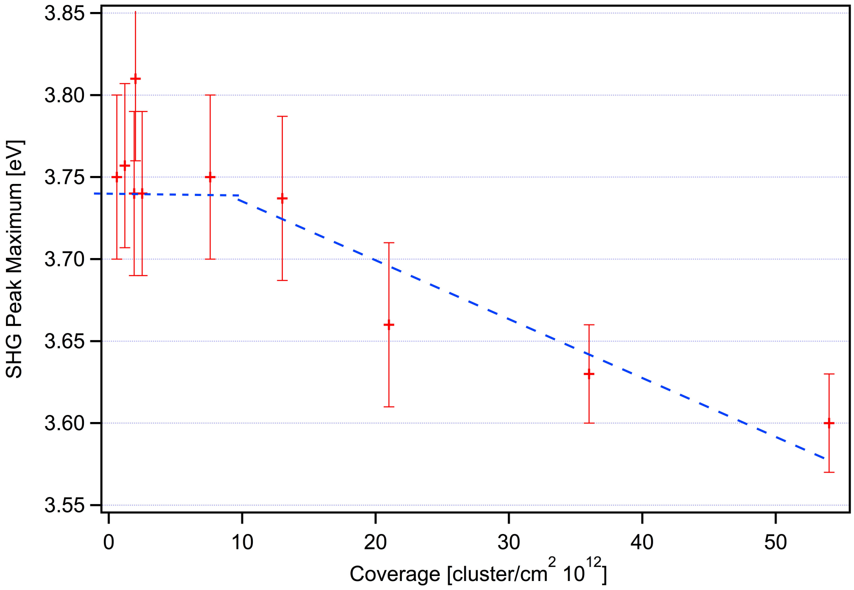

Figure 40: SHG Peak maximum vs. coverage.

In Figure 41 the peak width of the measured spectra is plotted versus the coverage. For small coverages the peak width (FWHM) is about $(0,8 \pm 0,1)$ eV, but it decreases for increasing coverage. This effect can also be assigned to potential coalescence of the deposited clusters. Bigger clusters should possess a narrower peak width due to an decrease of the damping constant described in Section 1.5.3.4 in Equation 57 and Equation 59. It should be noted that the value of the width is imprecise to some extent because the spectrum covers only 50% of the fit (see Figure 39). This is due to the red-shifted plasmon oscillation for bigger clusters, which is not completely covered by the laser system. However, the measured widths are in good agreement to other publications [39, 88].

The intensity of the peak maximum is plotted versus the coverage in Figure 42. The error is assumed to be 15 % of the signal's intensity[12]. Using classical Mie theory the signal intensity should depend linearly on the number of electrons contributing to the signal. This can bee seen by combining Equation 53 from Section 1.5.3.1 and Equation 67 from the following Section 4.2.1.

---

[12] The signal intensity depends on the amount of deposited clusters and the accurate placement of the substrate in the laser beam.

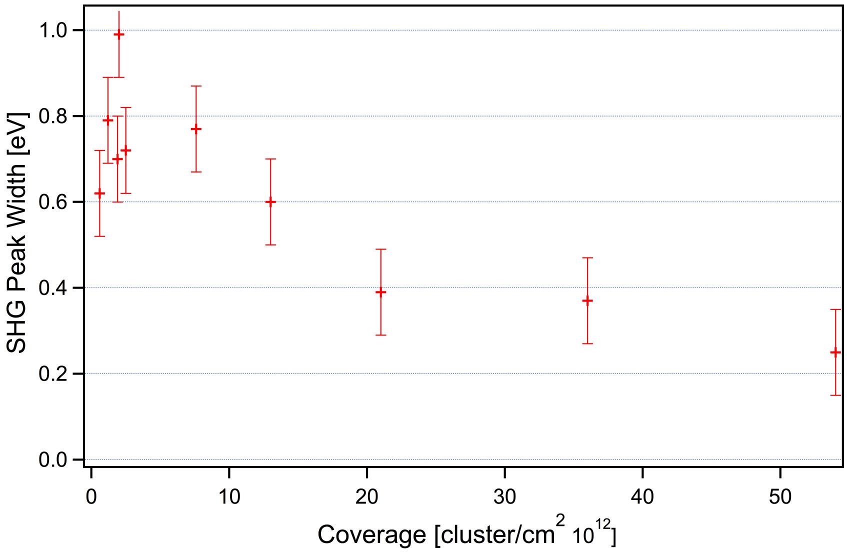

Figure 41: Peak (FWHM) width of the SHG signal for unselected clusters as a function of coverage. A decrease in FWHM with increasing coverage can be observed.

$$\begin{array}{rrcc} & \sigma_{ext} & \sim & V_0 \sim R^3 \\ & D = 2R & \sim & N^{\frac{1}{3}} \\ \Rightarrow & \sigma_{ext} & \sim & N \end{array} \tag{66}$$

As a first approximation the collective oscillations of the 5s electrons contribute to the signal. The signal should increase linearly with the amount of probed clusters. It should, however, also increase linearly with increasing cluster size, as shown in Relation 66[13]. This rule, however, only holds for spherical nanoparticles, which are well described within the (modified) Mie theory. For coverages above $\sim 25\%$ of a monolayer this assumption of spherical nanoparticles is, however, questionable. The increase in the intensity up to a coverage of approximately $15 \cdot 10^{12}$ clusters/cm^2 is a good indication of an increase of the amount of mono-dispersed clusters. Coalescence and accompanying flattening of the clusters is likely to occur above this coverage leading to a nonlinear increase of the signal's intensity.

In conclusion, the coverage-dependent measurements suggest that coalescence of the clusters occurs for coverages higher than $15 \pm 3 \cdot 10^{12}$ clusters/cm^2 for unselected clusters. This assumption is based on the red shift, the peak width and the intensity of the S-SHG signal. Thus, S-SHG measurements of deposited clusters should be performed for coverages smaller than this critical value. This is the case

---

[13] It will be shown later that this is not unrestrictedly the case for deposited size-selected clusters.

for all data of supported size-selected clusters presented in this chapter.

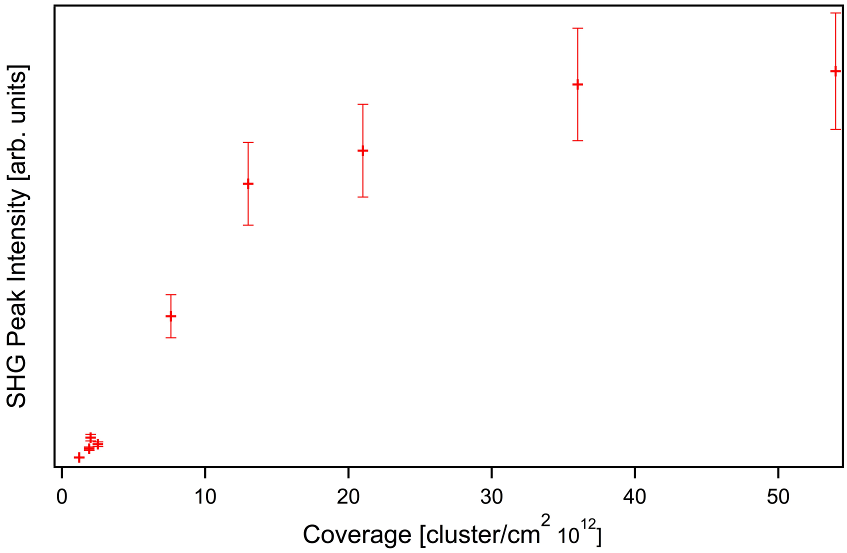

Figure 42: Peak intensity of the S-SHG signal of supported unselected clusters as a function of coverage (see text).

4.2 SIZE-SELECTED AG-CLUSTERS

In this Section S-SHG spectra of supported size-selected Ag-clusters in a size regime between Ag_9 to Ag_{55} are presented. Here the question arises, how the resonance of supported clusters evolves as a function of cluster size and what the physical origin of this potential evolution is. These two questions should be answered independently. The evolution of the resonance with cluster size can be measured experimentally whereas the origin of this evolution is more difficult to discern and clarification with theoretical calculations is required. This, however, is extremely difficult since the system as a whole should be calculated including cluster and amorphous substrate. In the following description the measured data are presented leading to possible explanation of the observed phenomena.

The measurement procedure was similar to the one described in the previous section and in Section 2.6.4. This size regime is of particular interest as it connects the size regime where molecular-like transitions of clusters are expected and were measured [152] to the size regime where clusters or nanoparticles are well described by Mie theory [25, 82].

In this series of experiments size-selected clusters were deposited onto the BK7 substrate in the same way as mentioned before for the unselected clusters. In order to avoid heating during deposition the electron source and hence the sample was cooled by liquid nitrogen.

This is especially crucial for these measurements because the deposition time increases up to 180 minutes due to the much reduced cluster currents (20 pA - 30 pA). The total number of clusters of the spectra presented in the following section was $1 \cdot 10^{12}$. This leads to a coverage of $\sim 3 \cdot 10^{12}$ clusters/cm^2 (see Section 4.1.1) in the cluster spot. As the cluster current was different for different cluster sizes[14] the deposition time was adjusted to ensure equal coverages. The coverage could in principal be increased leading to better signal, thus better spectra. Especially for small cluster sizes the signals arising from a coverage of $3 \cdot 10^{12}$ clusters/cm^2 is very weak. However, the presented data are a compromise between deposition time (not longer than 180 minutes) and reasonable signal-to-noise ratios.

4.2.1 *From Ag_{55} to Ag_9*

Spectra of size-selected clusters on BK7 are depicted in Figure 43. The spectra are not smoothed[15]. The oscillations result from the signal of the substrate (see Section 2.7 and ref. [25]). The lowest plotted spectrum is given by unselected clusters shown in the previous Section. Here, a mean cluster size of 55 atoms is estimated. The other spectra are taken from truly size-selected clusters. The size-selected clusters were all deposited in the same way (see Section 2.6). The coverage was kept constant at $\sim 3 \cdot 10^{12}$ clusters/cm^2 for all sizes. To ensure a clear presentation spectra of five different cluster sizes between $Ag_{<55>}$ and Ag_{15} are depicted. The remaining spectra for other sizes can be found in Section C.1.3. It can be seen that the implemented spectroscopic and experimental setup is sensitive enough to investigate truly size-selected mono-dispersed silver clusters (from Ag_{55} to Ag_9) on BK7 by means of S-SHG spectroscopy.

A few interesting observations are discussed in the following text. All spectra (including those in Section C.1.3) exhibit one peak maximum of lorentzian character rather than multiple distinct peak maxima which have been observed in the gas phase for very small size-selected clusters (see Section 4.2). This can be attributed to the influence of the support material. The binding to the support material leads to a fast decay of the plasmon which is reflected by a greater damping constant and hence a broadend peak (see Section 1.5.3.4).

---

[14] The cluster current depends on many parameters and settings of the cluster source and is thus different for different cluster sizes.

[15] The spectral artifacts have different origins and are of experimental nature. The laser-power correction might not be sufficient. Also, slight differences of the incident angle between reference spectrum and raw spectrum lead to increased oscillations. These artifacts could in principle be smoothed, as it was the case in previous work [25, 82], because they are not of physical orgin and do not influence the value of the peak maximum. However, to ensure a proper presentation the unsmoothed spectra are shown here.

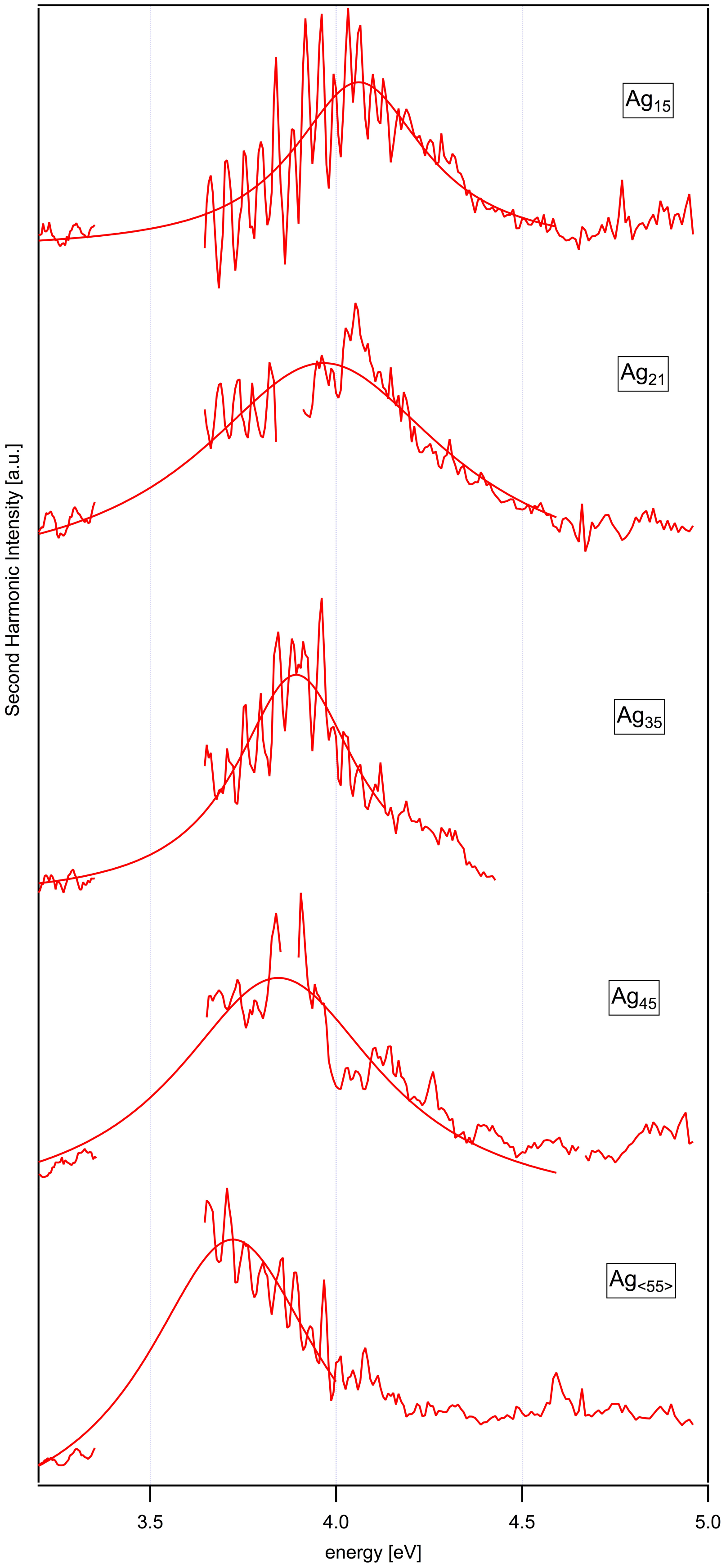

Figure 43: Spectra of size-selected clusters.

In this type of presentation a blue shift of the peak maximum towards smaller clusters can be observed. The parameters of the lorentzian fits for different cluster sizes are shown in Figure 44 and 45.

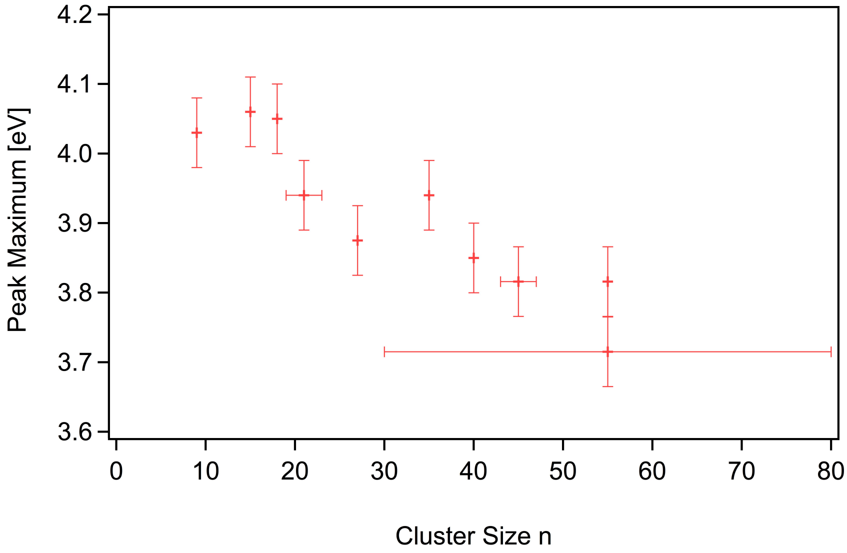

Figure 44: Resonance position as a function of cluster size. Ag_{21} and Ag_{45} were measured with a lower resolution, thus the error is about one atom. For repeatedly measured spectra the mean value is plotted. The last point at 3,7 eV corresponds to the Ag_{35} RF-only spectrum. A clear blue shift of the resonance position towards smaller clusters can be observed.

In Figure 44 the fitted peak positions are plotted as a function of cluster size[16]. A distinct blue shift can be observed for decreasing cluster size. This observation can presumably be attributed to the clusters' "spill-out effect" of the 5s electrons. An intrinsic property of the "spill-out effect" is the 1/D law, described in Section 1.5.3.4. This law reflects the growing surface contribution with respect to bulk effects in small clusters.

The intensities of the peak maxima are shown in Figure 45. In a first approximation the growing S-SHG intensity with increasing cluster size reflects the growing number of electrons participating in the "plasmon" oscillation[17]. In classical Mie theory the intensity of the S-SHG peak would scale with the particle volume and thus with the cluster size N (compare Equation 66). This should lead to a linear increase of the "plasmon" intensity as a function of cluster size. A contrary behavior is observed here. The peak intensity in Figure 45

---

[16] Ag_{21} and Ag_{45} were performed with a lower QMS resolution (see Section 2.4.1) in order to increase cluster current. This is reflected by the error bars.

[17] This approximation is only valid if the signal's shape (FWHM) is equal for all spectra. Then, the intensity scales with the integrated signal.

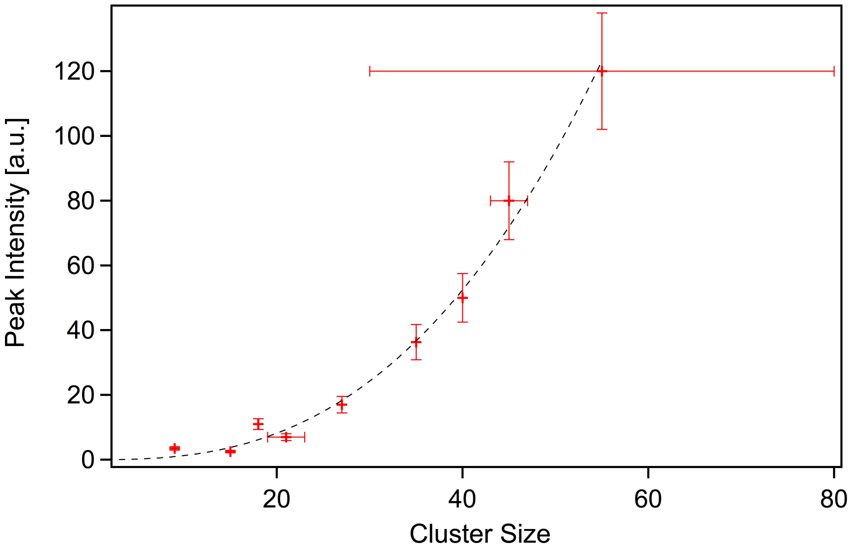

Figure 45: Peak intensity of S-SHG spectra of size-selected clusters.

increases with a power of 2,6 as a function of cluster size[18]. The strong signal intensity increase of size-selected clusters might have different origins.

An interpretation of the growing magnitude of the signal intensity might originate from the structure of the clusters. A deviation from the sphere-like shape could be more pronounced for small clusters. Then, the nonlinear increase could result from a transition of oblate-like structures for smaller clusters to spherical-like structures for bigger clusters. The plasmon oscillation which leads to the nonlinear signal would then nonlinearly increase with increasing cluster size.

Another possible explanation is the binding to the support material if the clusters are assumed to possess sphere-like character. The amorphous support surface is rather rough [25]. This might lead to an averaged absolute amount of binding atoms independent of the cluster size, which in turn leads to relatively more conduction electrons contributing to the SHG signal for bigger cluster sizes.

In Figure 46 the measured resonance positions are plotted as a function of $1/D$. Here, D is defined as the inverse nominal particle diameter

$$D = 2a_0 r_s N^{\frac{1}{3}} \tag{67}$$

where N is the number of atoms in the cluster, $a_0 = 0,0529$ nm and $r_s = 3,02$ is the electron density parameter of bulk silver [113]. This type of presentation of the plasmon resonance allows the size evolution to be plotted from bulk $(1/D) = 0$ to molecular-like clusters $(N \leq 8)$ [153]. The classical Mie resonance for silver nanoparticles in

---

[18] This is the value of the fit.

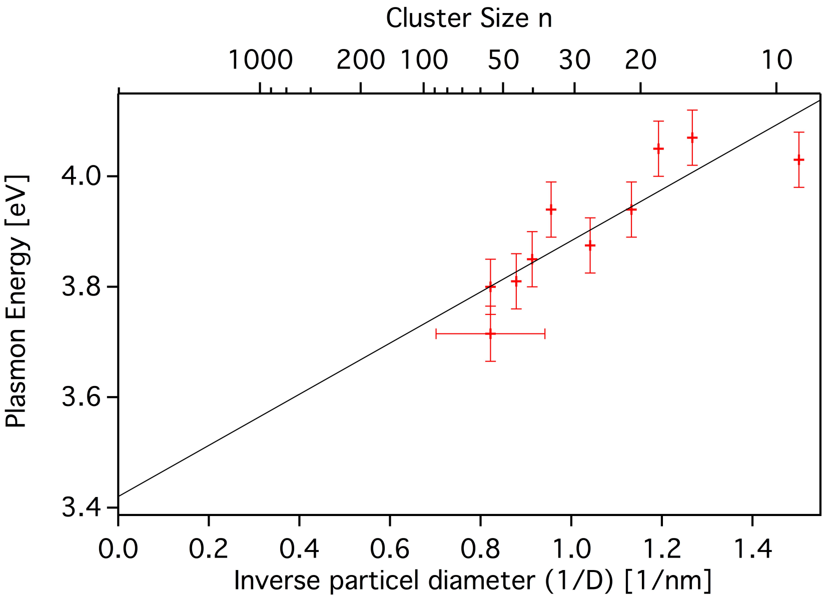

Figure 46: Resonance position of size-selected clusters as a function of inverse particle diameter including a linear fit.

vacuum is at $\hbar\omega(\infty) = 3,5$ eV (see Section 1.5.3.2) in the limit of large D (see Section 1.5.3.1). The strong blue shift of the data from Figure 46 is fitted by a linear function and extrapolated towards the axis intercept. The slope of the function is $b = 0,48 \pm 0,08$ eV/nm and the axis intercept is $a = 3,42 \pm 0,08$ eV. This $1/D$ behavior has been mentioned in Section 1.5.3.4. It reflects the growing surface contribution with respect to bulk effects with decreasing cluster size. The "spill-out effect" (see Section 1.5.3.4) of the electrons leads to a reduced s-d screening interaction in the outer region of the silver cluster. Inside the cluster the d-bands' strong depolarization field lowers the plasma frequency of the "free" electron gas. This effect however vanishes at the cluster surface. The "spilled out" electrons are hardly effected by the depolarization field of the 4d electrons. Thus, their plasma frequency is blue-shifted towards the unscreened value. The growing surface-to-volume ratio increases this effect with decreasing cluster size [39]. Hence, a blue shift of the plasmon frequency is observed. This effect has also been observed by other groups for size-selected clusters in vacuum and in matrices which will be shown in the next section.

The value of the axis intercept ($a = 3,42 \pm 0,08$ eV), hence the value of the large (classical) D limit from the fit, is in good agreement with the classical limit of $\hbar\omega(\infty) = 3,5$ eV. However it is red-shifted by $\approx 0,1$ eV. A red shift of the classical limit could potentially be attributed to a number of different origins:

The particles deposited on the substrate might not be spherical, but of oblate shape as mentioned previously. This leads to a plasmon splitting for the parallel and the orthogonal modes of the plasmon oscillation. To account for this effect shape factors were introduced and Mie theory was extended by this factors in Section 1.5.3.6. Including these shape factors however, leads to a blue shift of the perpendicular mode (1,0 mode) of the Mie plasmon for supported clusters[19]. Hence, this effect cannot be the major origin of the observed red shift of the classical limit. Another difference compared to the classical Mie limit of $3,5$ eV is the support of the cluster. The surrounding medium is thus not homogeneous, as would be the case for clusters in vacuum. This influences the dielectric constant of the surrounding and thus the resonance (Fröhlich frequency) of the plasmon oscillation (see Section 1.5.3.1).

For spherical particles the limit of the Mie resonance can be calculated using Equation 53. Vacuum (dielectric constant: $\epsilon_{vacuum} = 1$) leads to the aforementioned bulk limit of the Mie resonance of $\hbar\omega(\infty) = 3,5$ eV. For supported clusters however, the surrounding is not homogeneous. Thus, the dielectric constant of the surrounding must be modified. Taking the classic limit of the measured data of $a = 3,42 \pm 0,08$ eV leads to a dielectric constant for the surrounding of $\approx 1,3$. With a dielectric constant of BK7 substrate ($\epsilon_{BK7} = n^2 = 1,536^2 \approx 2,36$) the factor x by which the constants must be weighted can be calculated by:

$$\frac{\epsilon_{Vacuum} + \epsilon_{BK7}}{x} = 1,3 \tag{68}$$

This estimation leads to a factor $x \approx 2,6$. Since the plasmon oscillation is perpendicular to the surface a factor of $x = 2$ would represent an averaged influence of vacuum and support on the plasmon oscillation[20]. A value of x greater than 2 hence indicates a greater influence of the vacuum. This is reasonable for the data presented here if the clusters are assumed to be roughly spherical. The cluster-surface contat is then presumably small.

Another approach to estimate the contact area for different shapes of clusters can be made by using following estimation: The averaged dielectric constant of the surrounding must fulfill following equation:

$$\epsilon_m = y \cdot \epsilon_{BK7} + (1 - y) \cdot \epsilon_{Vacuum} \tag{69}$$

It can be seen that for supported clusters on a flat surface y must be a quantity between $0,5$ (both surroundings have the same influence) and 0 (only the vacuum has an influence on the averaged dielectric constant). Taking the aforementioned values for ϵ_m, ϵ_{BK7} and ϵ_{Vacuum}

---

[19] Note, that only the perpendicular $(1,0)$ mode is probed here (see Section 1.5.3.6). Other possible modes for larger clusters are not accessible by S-SHG spectroscopy. The linear absorption method of CRD spectroscopy can be used to probe the $(0,1)$ mode [25].

[20] A factor of 2 would lead to an averaged dielectric constant of the surrounding of $\epsilon_{average} = 1,68$.

leads to $y \approx 0,22$. Thus, the averaged dielectric constant of the surrounding is given by ~ 22 % of BK7 and ~ 78 % of vacuum. This is however an averaged value over all cluster sizes and might depend on cluster size. It is, nevertheless close to 30 % contact area which was observed by Hilger et al. for nanoparticles with diameters of $D = 2,0 \pm 0,5$ nm supported on SiO_2 [89] and is thus a reasonable value.

In the aforementioned interpretation of the measured data all clusters were assumed to possess spherical-like shape. The observed blue shift of the resonances was explained by the "spill-out effect". The observed red shift of the classical limit was attributed to support influences. Deposited clusters might however not always consist spherical shape.

Another approach towards the interpretation of the measured plasmon energies of supported size-selected clusters was given by Thämer [25, 82]. Here, the pronounced (plasmon) oscillation peak at $\sim 3,68$ eV for particles with a mean diameter of $\sim 1,5$ nm was interpreted including particle shape effects. A deviation of the particle shape from a sphere leads to a splitting of the Mie plasmon resonance and hence to different shape parameters for different particle axes (see Section 1.5.3.6). The assumed plasmon splitting was backed up by linear absorption measurements (cavity ring-down spectroscopy). Here, and in contrast to S-SHG spectroscopy the parallel mode $(1,1)$ of the plasmon oscillation can be measured, too. Using both spectroscopic techniques parts of both plasmon modes could be measured and the shape parameters were calculated. By defining direction-dependent dielectric constants the measured data were explained within classical Mie theory (neglecting quantum size effects such as the "spill-out effect" mentioned before). It was concluded, that the particles lie with their short axis perpendicular to the surface and the shape parameters were calculated [82][21].

However, by this interpretation the aforementioned blue shift with decreasing cluster size cannot be explained. To this extent quantum size effects, such as the "spill-out effect" should be considered for an extensive interpretation of the measured data. Shape effects might lose significance for decreasing cluster size, as well as for cooled deposited clusters, as was shown by Hilger et. al. [89]. Wenzel et al. investigated supported silver nanoparticles with a diameter of $0,8$ nm to 10 nm [154] during growth process. By measuring both resonance modes they could calculate the shape of the investigated particles. They found that small deposited particles are almost of spherical shape whereas larger clusters are oblate with axial ratios significantly lower than $a/b = 0,5$. They also performed temperature-dependent measurements and found a smaller axial ratio (clusters are of spherical shape) for decreasing temperature. The results were explained by

---

[21] The calculated shape parameters are: $L_x = L_z = 0,177$, $L_y = 0,646$.

size- and temperature-dependent relaxation times which the nanoparticles need to reach their equilibrium shape.

In conclusion, whether shape effects of the supported clusters or quantum size effects are the major origin of the discussed blue shift cannot be answered unambiguously. For the small clusters which are investigated in this thesis the influence of shape effects presumably decreases whereas quantum size effects are of more importance. However, both effects certainly play a role and influence the measured spectra. A good interpretation of the data can be achieved using the assumption that the deposited silver clusters exhibit sphere-like shapes instead of being oblate. Thus, it is more likely that the observed findings are dominated by quantum size effects instead of shape effects. The next section will compare the aforementioned results with previous measurements from literature, and underlines this assumption. However, for an exhaustive interpretation of the measured data theoretical investigations such as TDDFT [37, 155] or ab-initio calculations [116] which include both, the amorphous support material and the size-selected clusters are essential.

4.2.2 *Comparison with Literature*

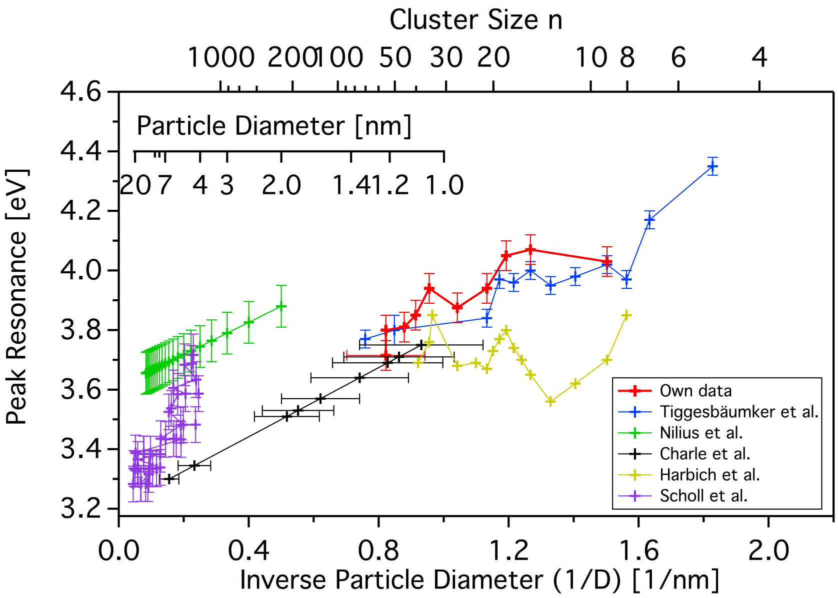

Figure 47: Comparison of measured data with results from other publications. The results from this work are drawn in red. For size-selected clusters the diameter was determined using Equation 67 and plotted versus the inverse particle diameter. For nanoparticles the data were plotted as a function of particle diameter shown in the inset of the diagram. (Tiggesbäumker [113]. Nilius et al.: [39]. Charle et al.: [151, 88]. Harbich et al.: [33]. Scholl et al. [38])

A comparison to other results from literature is given in Figure 47. Here, the aforementioned results are compared to measurements of silver clusters or nanoparticles from other publications [113, 39, 88, 33]. Some of these papers have already been mentioned in Section 1.5.3.8. Most presented data show a strong blue shift with decreasing cluster size which has been discussed in Section 1.5.3.8. The plotted data are discussed in the following.

The data from Tiggesbäumker et al. were measured by photo depletion spectroscopy in the gas phase. Closed shell clusters such as $Ag^{+}{}_{9}$ and $Ag^{+}{}_{21}$ showed a main single peak due to collective oscillation of the 5s electrons. Clusters with partially filled shells showed a splitting of the Mie resonance into several components. Here, an averaged frequency was calculated for better comparison, which is also plotted in Figure 47 and Figure 48. The resonance frequencies of the positively charged free Ag clusters converge reasonably well with increasing diameter D towards the classical limit at $3,5$ eV. This behavior is expected from theory since no other effects such as support or surroundings as well as cluster-cluster interactions "perturb" the results.

Charle et al. measured the Mie plasmon resonance of Ag clusters ($1,5$ nm ≤ 30 nm) embedded in cold Ar matrices by means of absorption spectroscopy [151, 88]. Fitting their data towards the classical limit leads to an experimental value of $\hbar\omega = 3,21$ eV. This value is strongly red-shifted compared to the value of classical Mie limit. However, it can be attributed to the embedding argon matrix, which changes the dielectric constant of the surrounding.

The data from Harbich et al. were gained by measuring absorption spectra of size-selected silver clusters in cold matrices [33, 36]. They found 1 to 3 major absorption peaks and stated, that for these size-selected clusters the aforementioned $1/D$ behavior vanishes and drastic deviations occur. The data are a good link to the aforementioned measurements by Charle et al. if extrapolated towards smaller clusters (see Figure 48) however, they show drastic deviations for smaller clusters. These are attributed to the cold and well defined temperature of the clusters in the matrices.

Nilius et al. measured plasmon resonances of deposited silver nanoparticles which were stimulated by electron injection [39]. They calculated the classical limit of the resonance peak for deposited clusters at $3,45$ eV including effects of cluster shape and influence of the surrounding[22]. However, fitting their data towards the classical limit leads to an experimental value of $3,6$ eV which is significantly higher than the calculated position and blue-shifted instead of red-shifted to the classical Mie resonance ($3,5$ eV). This deviation was discussed

---

[22] This was done by taking geometric depolarization factors of $0,4$ for the given cluster shape and an averaged dielectric constant of the surrounding (70 % vacuum and 30 % alumina film).

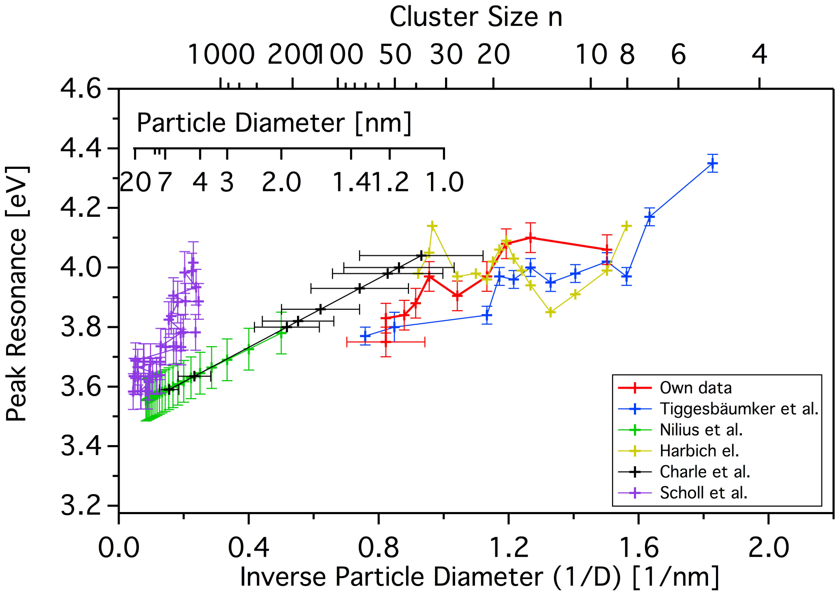

Figure 48: Comparison of measured data with results from other publications (see also Figure 47). Here, the data were scaled to converge to the classical vacuum bulk limit of 3,5 eV as described in the text.

and attributed to two possible effects. Firstly, an image dipole interaction between the cluster and the NiAl surface could presumably lead to a blue shift of the plasmon energy (see Section 1.5.3.5). Secondly, the internal plasmon potential is affected by the electrostatic field induced by the negatively charged tip. This negatively charged field pushes the silver electrons at the exposed surface into the cluster volume and leads to a local increase of the electron density, which in turn leads to a further blue shift.

Scholl et al. recently investigated supported silver nanoparticles on carbon and silica by electron microscopy and measured the size dependency of the surface plasmon [38]. Their results do not match the results from the other publications mentioned above, which has already extensively been discussed by Haberland [153]. He states that the deviations are presumably due to influences by interactions with the underlying surface and residual ligand molecules. In fact, the rescaled resonances of Scholl et al. are the only data that do not match (within small deviations) the resonance peaks for supported size-selected silver clusters that are presented in this thesis.

Given that the dielectric function for silver is nearly linear between 3 eV and 4 eV the aforementioned data can be shifted by the difference between the measured resonance bulk value and the Mie resonance bulk value to obtain the corresponding energies in vacuum[23]. For the data from Harbich et al. and Charle et al. [33, 36, 88] this difference

---

[23] This approach for better comparison has also previously been used in literature [153].

is given by ca. $-0,29$ eV. This shift can be attributed to matrix effects as discussed previously. The dielectric constant of the argon matrix is $1,75$ leading to a bulk limit Mie resonance of $3,22$ eV. For the plasmon resonance measured by Nilius et al. [39] the difference is $0,11$ eV.

The data can be rescaled by these differences in order to compare them with obtained resonance energies in vacuum. This leads to Figure 48.

It can be seen, that the rescaled data of supported size-selected clusters in this thesis are in remarkably good agreement to resonances of size-selected clusters and nanoparticles from other publications. The rescaled peak resonance as well as the observed blue shift for smaller clusters coincide with other publications as previously described. It should however be noted that these are the very first optical spectra of size-selected clusters on surfaces. The aforementioned spectra from other publications in the same size regime are either measured in matrices or in vacuum which makes their significance for further investigations arguable to some extent.

4.2.3 *Stability and Oxidation*

In this section the interaction between background gases and deposited clusters is investigated. The presented results are preliminary, but show some interesting and new features. For a comprehensive interpretation of these results more measurements and especially theoretical support is needed.

Size-selected clusters were exposed to different background gases whilst the S-SHG signal of the plasmon resonance was recorded. Oxygen was the gas of potential interest for this type of investigation. However, argon and helium were also investigated[24]. This was done by using a new gas-line which is described in Section 2.3.3 in detail.

Not much is known in literature about the oxidation of small size-selected supported silver clusters (see Section 1.5.3.10). It has not been investigated by nonlinear spectroscopic methods, yet. At room temperature planar silver surfaces chemically bind oxygen only at defects [70]. Cluster surfaces are however, always irregular and contain edges and corners, hence there are many oxidation sites. Supported size-selected clusters are a perfect model system for the investigation of the potential interactions of clusters and adsorbed molecules. The observed decrease in S-SHG intensity can presumably be attributed to the oxidation of silver clusters. The spectra were measured as follows.

---

[24] Argon and helium did not have any influence on the "plasmon oscillation" of unselected silver clusters, as expected. Both were leaked into the chamber under same conditions as oxygen. The S-SHG signal remained constant, even if the background pressure was increased towards $1 \cdot 10^4$ mbar.

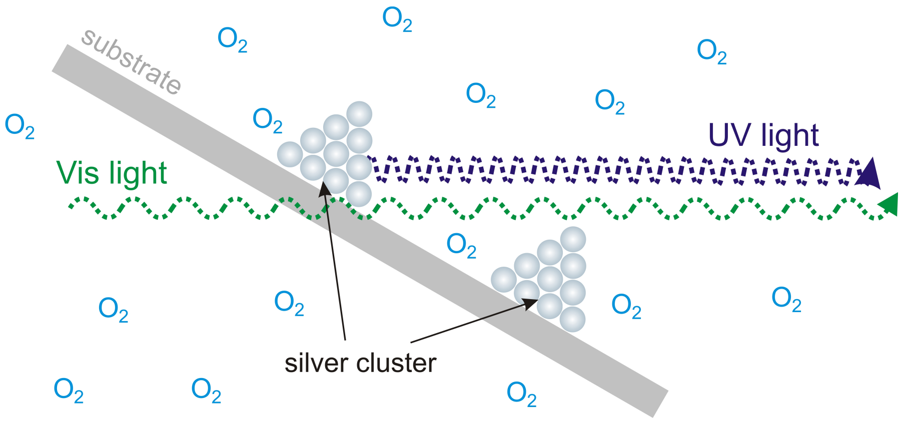

Figure 49: Schematic of the performed oxidation measurement of size-selected clusters.

First, size-selected clusters were deposited and S-SHG spectra were recorded as described in the previous Section 4.2. Afterwards the S-SHG signal was measured at resonance[25] for approximately 6 minutes. Then, oxygen was leaked into the UHV chamber with a background pressure of $5 \cdot 10^{-6}$ mbar[26]. The signal decreased with time but remained constant at a considerably lower intensity as soon as the leakage was discontinued. No shift of the resonance peak was measured [77]. Similar behavior of the nonlinear response of supported Na nanoparticles (R= 40 nm) which were exposed to oxygen ($1 \cdot 10^{-8}$ mbar) has been observed previously [120]. This led to the conclusion that the detected SH signal almost exclusively originates from the particle surface and "bulk" contributions were estimated amount to at most 10%.

An example of a time scan with oxygen background pressure is depicted in Figure 50. The S-SHG signal remains constant until oxygen is leaked into the chamber. The subsequent decay of the signal intensity is rapid in the beginning and proceeds more slowly at the end. For all measurements presented in the foloowing the signal was recorded for approximately 50 minutes before the time scan was stopped. The data were subsequently fitted by a double exponential decay function:

$$y = y_0 + A_1 \cdot e^{-\frac{(x-x_0)}{\tau_1}} + A_2 \cdot e^{-\frac{(x-x_0)}{\tau_2}}$$

The good agreement between measured data and the fit of the double exponential decay function can be observed[27]. This leads to the

---

[25] This resonance shifts slightly towards higher energies with decreasing cluster size (see Section 4.2).

[26] This background pressure value turned out to be a good compromise between reasonable time scans and good spectra for the subsequent fitting procedure.

[27] All other oxidation measurements for different cluster sizes (not shown in this thesis) showed similar double exponential decay behavior.

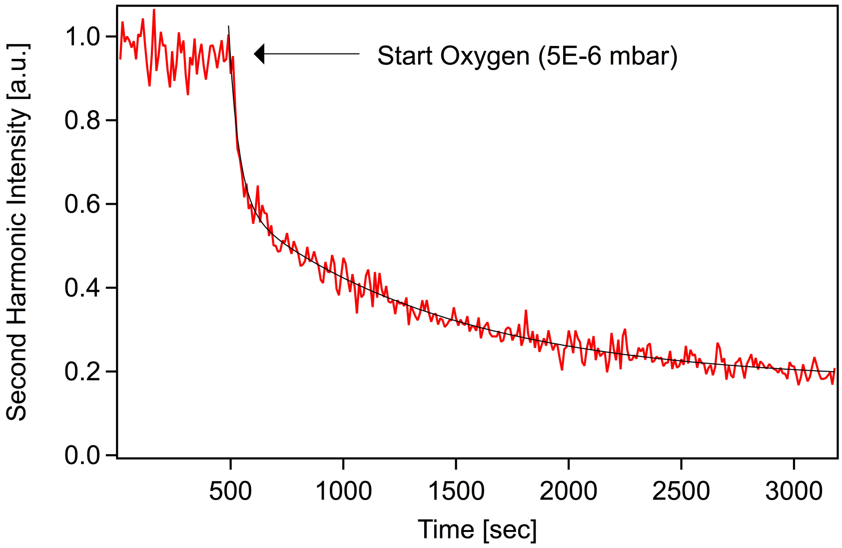

Figure 50: Example of an oxidation time scan with Ag_{21}. The oxygen is leaked into the UHV chamber after 500 seconds with a background pressure of $5 \cdot 10^{-6}$ mbar. The decrease in intensity is fitted by a double exponential decay function.

assumption that the decay of the signal's intensity is of twofold origin, hence a more complicated kinetic model is needed. The rapid decay in the beginning is described by the parameters of the first exponential decay function A_1 and τ_1, the smooth decay at the end by A_2 and τ_2 respectively. y_0 describes the offset of the function.

The values of the fitting parameters are plotted in Figure 51 as a function of cluster size. The errors were gained from the fits. No correlation between cluster size and the fitting parameters τ_1, A_2 and τ_2 can be observed. However, A_1 seems to decrease and y_0 seems to increase with cluster size. This behavior could arise from various sources, therefore further investigations are needed in order to provide an extensive interpretation. The following considerations should be taken into account.

Assuming a sticking coefficient of 1 and an exposure of one Langmuir, one monolayer of oxygen molecules on the surface is reached after approximately $0,2 - 1$ seconds at the used background pressure. The signal's rapid decrease in the beginning occurs on a much longer timescale. Taking a time constant of $\tau_1 = (60 \pm 20)$ seconds (see Figure 51) one half of the signals rapid decrease in the beginning is complete after (40 ± 15) seconds[28]. Note, that only the plasmon-decay is measured here and no information is gained on possible reaction products and how the plasmon oscillation is influenced by possible chemisorbtion or dissociation of adsorbed oxygen molecules.

---

[28] One half of the intensity is given by $x = -\tau \cdot ln(0,5)$.

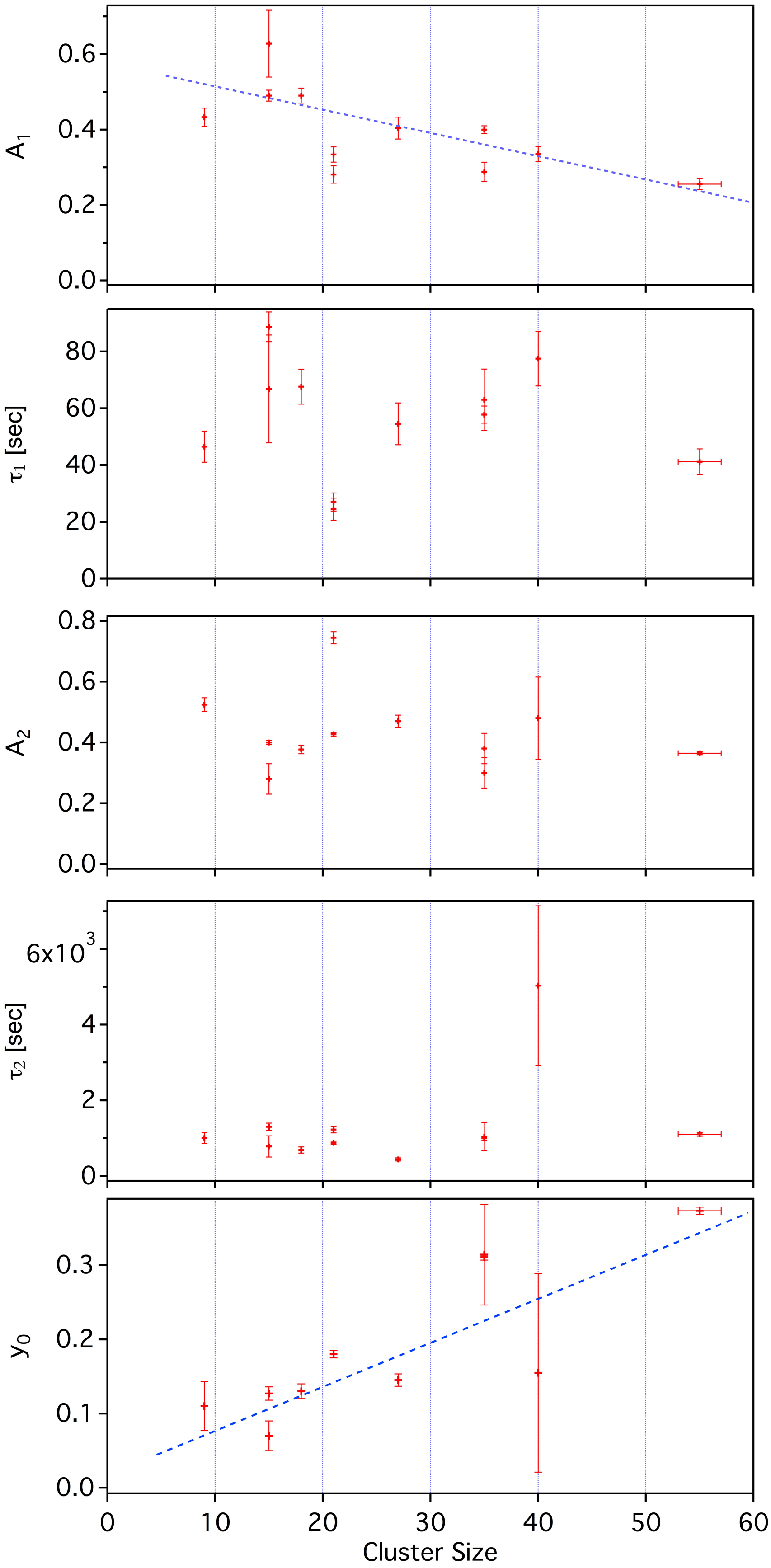

Figure 51: Fit parameters (including errors) for the double exponential decay functions. The blue lines are drawn to guide the eye (see text).

As described in Section 1.5.3.9, oxygen molecules might chemisorb on the surface of the clusters leading to a surface reaction. Then an electron transfer from the metal to the O anti-bonding π^* orbital occurs. As the S-SHG signal mainly arises from the surface of the cluster the signal is expected to decrease. The chemisorption of oxygen molecules at a silver surface has been observed for bulk materials before [119]. However, in contrast to the bulk metal the electron reservoir of the cluster is finite. The whole system stays neutral but a chemisorbed molecule charges the cluster by an elementary charge. This phenomenon has been observed for free clusters in vacuum [118]. Since the number of free electrons in the cluster which can be extracted is limited, a chemisorbed oxygen molecule lowers the probability for further chemisorption.

Further oxygen molecules, however, might still penetrate into the cluster leading to a volume reaction. Those oxygen molecules bind to the remaining silver atoms which leads to a complete vanish of the nonlinear signal.

Another approach to the understanding of the presented data is given by looking at the O-O bond of the oxygen molecules. Schmidt et al. showed a temperature-dependent reaction for nanoparticles in the gas phase (see Section 1.5.3.10). For temperatures above 77 K the molecules are chemisorbed on the cluster. However, for temperatures above 105 K the chemisorbtion turns into a permanent oxidation where the O reaches an oxidation state of -2. The O-O bond breaks at these temperatures. The reported data indicate that silver clusters presumably dissociate the oxygen molecules and an Ag_2O molecule is formed. The other highly reactive oxygen atom is directly ejected into the vacuum during dissociation. The remaining metallic part of the cluster can undergo a new cycle of chemisorption and subsequent oxidation allowing the complete cluster to oxidize.

The temperature of the clusters is difficult to evaluate. This is due to two reasons: Firstly, the substrate holder is cooled by liquid nitrogen, however the temperature at the substrate itself is unknown. It depends on the heat conductivity of the substrate and the heat radiation from the surrounding. Secondly, the clusters are exposed and excited by ps-laserlight making a accurate temperature definition complicated. However, it is reasonable that the temperature is sufficiently high to break the O-O bond leading to a complete oxidation of the cluster with the mechanism described previously. This could in principle explain the measured data.

The signal offset, y_0, which seems to increase with cluster size might be an indication that the cluster does not oxidize completely, leaving electrons which contribute to the plasmon-like transitions.

These preliminary results need further investigation (experimental and theoretical) in order to provide an extensive interpretation including kinetic models. Possible tunable parameters are the cluster-size,

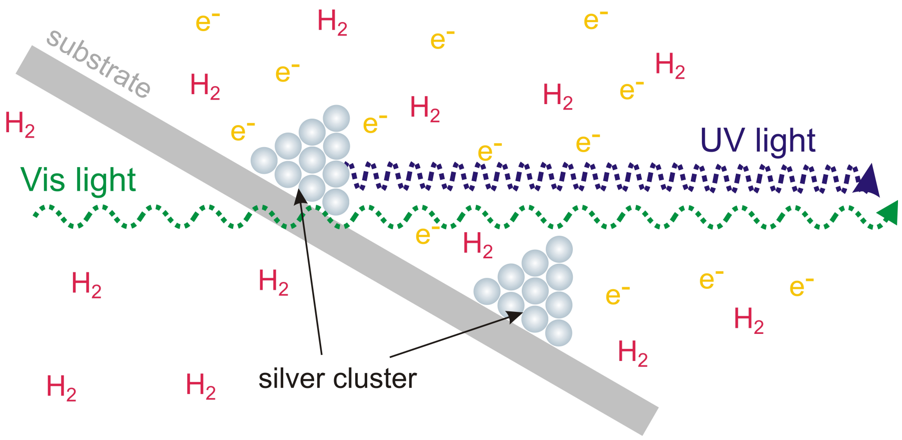

Figure 52: Schematic of the performed hydrogen measurement of size-selected clusters.

temperature, background pressure and the laser power. Also other background gases could in principle be investigated.

4.2.4 *Reaction with Hydrogen*

In the next experiment molecular hydrogen was used as the background gas. Atomic hydrogen is the lightest element and (atomic and molecular) hydrogen is highly combustible.

In order to investigate potential interactions of hydrogen and supported silver clusters it was leaked into the UHV chamber and identical measurements as with oxygen were performed (see Section 4.2.3). A schematic of the measurement is shown in Figure 52. No decrease in SHG intensity was observed, even at the highest background pressure (up to $1 \cdot 10^{-4}$ mbar).

In Figure 53 a measurement of Ag_x with hydrogen is shown. First, the signals intensity was recorded under UHV conditions. Hydrogen was subsequently leaked into the chamber with a background pressure of $5 \cdot 10^{-6}$ mbar. In contrast to oxygen no decrease in intensity was observed. The electron source (see Section 2.4.2) was switched on after ~ 1000 seconds which led to a rapid decrease in S-SHG intensity[29]. After a further ~ 100 seconds the electron source was switched off, and a smooth increase in S-SHG intensity was observed.

The decrease and increase of the intensity show exponential behavior[30]. A first possible explanation of this behavior is given in the following description. After leaking H_2 into the chamber the molecules are presumably physisorbed on the cluster surface within

---

[29] Note that the electron source did not have any influence on S-SHG measurements with other background gases.

[30] The time constants of the exponential decay fit for the decrease and increase of the function are $\tau_1 = 41 \pm 2$ s, and $\tau_2 = 570 \pm 15$ s, respectively.

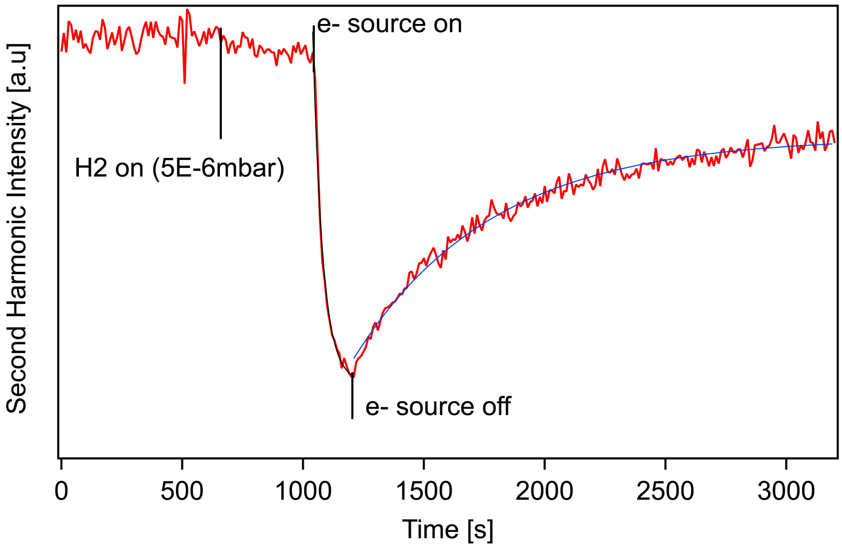

Figure 53: Example of a time scan with Ag_x and H_2. The hydrogen is leaked into the UHV chamber after $\sim$ 700 seconds with a background pressure of $5 \cdot 10^{-6}$ mbar. The SHG signal remains constant. After $\sim$ 1000 seconds the electron source is switched on. The signal decreases rapidly within $\sim$ 100 seconds. Afterwards the electron source is switched off and the signal increases and converges to its old value. The decrease and increase of the intensity is fitted by two exponential decay functions marked in black and blue, respectively.

seconds. In contrast to oxygen no chemisorbtion occurs, thus the free-electron behavior of the Ag electrons is not disturbed and no decrease in S-SHG intensity is observed. When the electron source is switched on, kinetic electrons with energies between $0 - 12$ eV are emitted and guided towards the cluster hydrogen complexes and might lead to a dissociation of the physisorbed hydrogen molecules [156]. Atomic hydrogen however is highly reactive and forms silver-hydride AgH. Since the electrons are bound within the AgH molecule they do not contribute to the plasmon-like oscillation, hence the intensity decreases. Silver-hydride however, is not stable and dissociates into Ag and H. These two mechanisms compete with each other, however as soon as the electron source is switched off silver hydride dissociates and silver clusters with free electrons remain leading to the original plasmon-like oscillation.

4.2.5 *Summary and Conclusion*

In the previous section unselected and size-selected supported silver clusters were investigated by means of S-SHG spectroscopy. It was shown by cavity ring-down spectroscopy that the distribution of the clusters on the substrate surface is of gaussian character and a method for the estimation of the coverage was introduced. Nonlinear spectra of unselected clusters $\mathrm{Ag}_{<55>}$ were plotted, discussed and compared to previous measurements from literature. A pronounced plasmon resonance was observed which already revealed the high sensitivity of this nonlinear background-free technique. Coverage-dependent measurements indicated a coalescence of the supported unselected clusters for coverages higher than $15 \cdot 10^{12}$ clusters/cm^2.

In addition, S-SHG spectroscopy of supported size-selected silver clusters was conducted. To the best of the authors knowledge these are the very first optical spectra of supported size-selected silver clusters in the size regime between $\mathrm{Ag}_{<55>}$ and Ag_9. The data show one pronounced peak for all cluster sizes which can be understood as a collective oscillation of the conduction electrons. It is very likely that these peaks are broadened due to cluster-support interactions as well as cluster temperature. The data reveal a pronounced blue shift with decreasing cluster size. This behavior was discussed in terms of quantum size effects and compared to other measurements in literature, which show a similar behavior.

In the next series of experiments cluster-molecule interactions induced by background gases were investigated. The gas of special interest was oxygen as silver is known to oxidate under certain conditions. The resonance intensity of the (size-selected) clusters was recorded over time and decreased whilst oxygen was leaked into the chamber. All data show a double exponential decay behavior which suggests the interpretation that the decrease of the signal intensity is based on two independent physical processes. The decrease of the intensity showed the enormous potential of these kinds of oxidation measurements for further investigations.

At the end a first measurement of the interaction of supported silver clusters and molecular hydrogen was presented. Hydrogen did not influence the S-SHG signal of the supported clusters. A rapid decrease in S-SHG intensity, however, was observed when silver cluster hydrogen complexes were exposed to kinetic electrons. A possible explanation of this behavior were given, however further measurements are necessary for a better understanding and clarification of this observation.

All presented types of spectra in this preceding chapter showed the enormous potential of the investigation of size-selected supported clusters by nonlinear spectroscopy. Supported clusters allow for the investigation of possible surface effects (in contrast to clusters in the gas phase) and are of fundamental interest for the design of new catalysts. Also, deposited clusters enable further investigations such as cluster-molecule interactions or catalytic reactions, as partly described in this section.

Many different organic molecules could in principle also be evaporated onto supported clusters from the solid phase using the evaporator described in Section 2.3.1.

Part V

SUMMARY AND OUTLOOK

5

SUMMARY

Cluster science in general is a diverse field with multidisciplinary implications for many scientific research fields. One primary interest of cluster science is the study of the evolution of material properties with size; starting from a single atom, over size-selected clusters, bigger nanoparticles and ending at bulk materials. Optical investigations of this evolution lead to a better understanding of the investigated system. This primary interest was already proposed by Gustav Mie in 1908 who stated[1]: "Because gold atoms surely differ in their optical properties from small gold spheres," it would "probably be very interesting to study the absorption of solutions with the smallest sub-microscopical particles; thus, in a way, one could investigate by optical means how gold particles are composed of atoms." [78].

Besides this scientific interest, cluster science is always accompanied by industrial interest due to the possible applications of small (size-selected) clusters. Here, the potential tailoring of the (catalytic) properties of clusters is investigated. The potential production of chiral supported clusters is a research field of especially great and current interest. The results of this work contribute towards a better understanding of both above mentioned topics.

This thesis comprises spectroscopic measurements of supported chiral 2,2´-dihydroxy - 1,1´−binaphthyl (Binol) molecules and supported mono-dispersed size-selected silver clusters under UHV conditions. Also, the interaction of supported size-selected clusters with adsorbed molecules was investigated. As the optical response of such samples is very weak, extremely sensitive and sophisticated spectroscopic methods were needed. An existing experimental setup was modified for the spectroscopic investigation. A state of the art spectroscopic setup including a picosecond lasersystem was built and installed to provide nonlinear spectroscopic methods for the investigation of both supported mono-dispersed size-selected clusters and chiral adsorbates. Nonlinearity came into play here, as techniques, which are based on second order nonlinear processes, provide the high sensitivity which was required for the detection of the very weak optical response of such samples.

---

[1] Original: "...da die Goldatome sich sicher optisch anders verhalten als kleine Goldkügelchen. Es wäre daher wahrscheinlich sehr interessant, die Absorption der Lösungen mit allerkleinsten amikroskopischen Teilchen zu untersuchen und gewissermaßen optisch den Vorgang zu verfolgen, wie sich die Goldteilchen aus den Atomen aufbauen."

THEORY

In this context the nonlinear susceptibility tensor $\chi^{(2)}$ was introduced and shown to describe the nonlinear interaction of light and matter. Surface Second-Harmonic-Generation (S-SHG) spectroscopy, as well as Second-Harmonic-Generation Optical-Rotatory-Dispersion (SHG-ORD) spectroscopy were derived from considerations of the symmetry properties of $\chi^{(2)}$. It was shown that S-SHG is a very sensitive and effective nonlinear spectroscopic method for the spectroscopic investigation of adsorbates on surfaces and that SHG-ORD is an extremely chiral-sensitive tool to probe chiral adsorbates at surfaces. The SHG-ORD effect was compared to its linear analogue (ORD) and shown to be material (tensor elements, orientation) as well as incident-angle dependent. The probe molecule of interest ($2,2'$-dihydroxy - $1,1'$-binaphthyl) was described and it was shown that the nonlinear chiral response can be described by only including electric dipole transitions. Therefore, it was the ideal molecule to test this nonlinear effect.

Silver was shown to be the perfect material for the spectroscopic investigation of very small clusters. The optical properties of metal clusters were first explained classically within the Mie theory which was later expanded by theoretical considerations derived for the "quantum size regime" of very small size-selected clusters. Theoretical models for possible cluster-cluster as well as cluster-support interactions were derived from classical Mie theory.

EXPERIMENTAL SETUP

A new setup was built and adapted to the UHV chamber in order to investigate small supported size-selected clusters as well as chiral adsorbates spectroscopically. It allows for S-SHG measurements, as well as chiral-sensitive measurements of adsorbates by SHG-ORD spectroscopy. Both spectroscopic methods can readily be employed without the need for realignment, which is greatly advantageous for daily laboratory work. S-SHG spectroscopy was shown to provide the high sensitivity which was needed in order to investigate small supported size-selected clusters with very low coverage. SHG-ORD spectroscopy provides an extremely high sensitivity for the distinction between enantiomers which is up to 6 orders of magnitudes greater than it's linear analogue. Both spectroscopies were controlled by newly programmed software which provides fully automated S-SHG scans as well as SHG-ORD scans.

For the investigation of molecules an HV evaporator was built and added to the experimental setup. A quartz microbalance was added to the setup to monitor the evaporation process. This combination allowed for precise evaporation of very thin molecular films which was crucial in order to understand the chiroptical signal.

A sophisticated reference method for S-SHG spectroscopy was introduced to properly treat the measured raw data. It directly allowed the extraction of reference-corrected S-SHG spectra from raw data. SHG from the pure substrate (BK7) in the wavelength range of interest was used to obtain the reference spectrum. This was used to correct the measured raw data. The accuracy of the presented procedure was demonstrated by applying the method to the study of a thin molecular film of 2, 2´-dihydroxy-1, 1´−binaphthyl (Binol) supported on a BK7 substrate. The successful mathematical description of the nonlinear spectrum of the substrate was a crucial step, necessary for the extraction of the nonlinear spectra from the measured raw data and was subsequently used throughout this thesis [25, 140].

A new gas line was built and attached to the experimental setup. It allowed for the performance of gas-background pressure-dependent spectroscopic measurements under UHV conditions.

Furthermore a new picosecond laser-system was installed and used in conjunction with the experimental setup during this work. It is composed of three different subsystems: a pump laser, a harmonics unit and a frequency conversion unit. It provides coherent radiation from 210 nm to 2100 nm with a repetition rate of 20 Hz, a pulse-length of 30 ps and pulse-energies between 0, 2 mJ and 1 mJ.

NONLINEAR SPECTROSCOPY OF BINOL

The new experimental setup was used to perform SHG-ORD measurements in vacuum under fully controlled layer thickness. Well defined thin molecular films of 2, 2′-dihydroxy-1, 1′binaphthyl (Binol) molecules at coverages between $5 \cdot 10^{15}$ molecules/cm^2 and $5 \cdot 10^{17}$ molecules/cm^2 on thin glass substrates (BK7) were investigated under UHV conditions. SHG-ORD measurements were performed with this new spectroscopic setup. This allowed for the determination of the rotation angle of the SH-signal of two enantiomers with extremely high chiroptical sensitivity. Coverage dependent orientation evolution of Binol molecular films was revealed by precise monitoring of the surface coverage while performing SHG-ORD experiments. Differences in the plane of polarization of up to $\nabla\phi = \phi_R - \phi_S = (75 \pm 2)^\circ$ were measured for different enantiomers and showed the extremely high chiroptical sensitivity of this nonlinear technique. The investigated molecules were stable and did not show any self-assembling effects under these conditions. Also, no photo-bleaching or photo-degradation effects could be observed. The reported data strongly confirm the in-plane isotropy for the investigated system, and thus support the validity of the chosen theoretical description.

The rotation angle changed dramatically with coverage until saturation. This behavior was attributed to orientational effects, thus the origin of this effect lies in the different orientations of the molecules' hyperpolarizability for different coverages. It could be shown, that coverage dependent measurements are crucial in order to understand the chiroptical response of molecular films. The data indicate that the molecules reach their final orientation at approximately $5 \cdot 10^{16}$ molecules/cm^2. The ratio of chiral to achiral tensor components could be calculated and showed to change with coverage [141].

NONLINEAR SPECTROSCOPY OF SILVER CLUSTERS

In the next series of experiments, unselected and size-selected supported silver clusters were investigated under UHV conditions by means of S-SHG spectroscopy. First, it was shown by the linear absorption technique of cavity ring-down spectroscopy that the distribution of the clusters on the substrate surface is of gaussian character. A method for the estimation of the coverage was introduced. These measurements already confirmed the successful deposition of (size-selected) clusters onto the substrate under UHV conditions. A coverage of $3 \cdot 10^{12}$ clusters/cm^2 was chosen for all following measurements which corresponds to ca. $0,05$ monolayers.

Afterwards, nonlinear spectra of unselected $\mathrm{Ag}_{<55>}$ clusters with an average diameter of $1,5$ nm were recorded and showed that plasmonic excitations inside the clusters give rise to a SHG signal. A pronounced resonance was observed which revealed the high sensitivity of this nonlinear background-free technique and could be interpreted by Mie theory. This resonance results from an excitation perpendicular to the substrate surface due to the selection rules of the SHG process. A peak located at $(3,76 \pm 0,05)$ eV was measured and attributed to a plasmon like transition at second harmonic frequency. The results were plotted, discussed and compared to previous measurements from literature.

Coverage-dependent measurements were subsequently performed. The recorded spectra showed a red shift when the coverage exceeded a value of $(15 \pm 3) \cdot 10^{12}$ cluster/cm^2. This observation was attributed to a potential coalescence of the clusters when this value was exceeded and hence showed the necessity to keep the coverage below this critical value. This interpretation was backed up by measurements of the signal's width and intensity.

In addition, S-SHG spectroscopy of supported size-selected silver clusters was conducted. The coverage was kept constant at $3 \cdot 10^{12}$ clusters/cm^2 for all sizes. The implemented spectroscopic and experimental setup was shown to be sensitive enough to investigate truly size-selected mono-dispersed silver clusters on BK7 by means of S-SHG spectroscopy. To the best of the authors knowledge these are the very first optical spectra of supported size-selected silver clusters in this size regime between $\mathrm{Ag}_{<55>}$ and Ag_9.

The data show one pronounced peak for all cluster sizes which can be understood as a collective oscillation of the conduction electrons. It is very likely that these peaks are broadened due to the temperature of the clusters as well as the cluster-support interaction. The data reveal a pronounced blue shift (from $\sim 3{,}7$ eV to $\sim 4{,}1$ eV) with decreasing cluster size. This behavior was discussed in terms of shape effects and quantum-size considerations and interpreted by the "spill-out" effect, which increases for smaller particles as the surface to volume ratio increases. The data were plotted as a function of the inverse particle diameter $(1/D)$, as this type of presentation of the plasmon resonance allows the size evolution to be plotted from bulk $(1/D) = 0$ to molecular like clusters. By fitting the data an averaged dielectric constant of the surrounding was estimated which consists of $\sim$ 22% of the BK7, and $\sim$ 78% of the vacuum dielectric constant. Hence, the contact area of the clusters is presumably small. These findings led to the conclusion that the data can be explained if the supported clusters are assumed to possess spherical-like shape as a first approximation. It was discussed how deviations of the clusters' shape would influence the spectra. The data were compared to literature measurements in the gas phase or embedded in matrices, which showed a similar behavior.

In the next series of experiments cluster-molecule interactions induced by background gases were investigated. For that purpose a gas-line was implemented to the analysis chamber, in order to perform partial background pressure-dependent S-SHG measurements. Oxygen was the gas of special interest as silver is known to oxidize under certain conditions. The resonance intensity of the (size-selected) clusters was recorded whilst oxygen was leaked with a background pressure of $5 \cdot 10^{-6}$ mbar into the chamber. The signal decreased over time but remained constant at a considerably lower intensity as soon as the leakage was discontinued. The measurements were performed as a function of cluster size. All data showed a double exponential decay behavior which suggests the interpretation that the decrease of the signals intensity is based on two independent physical processes. These preliminary results showed the enormous potential and high sensitivity of S-SHG spectroscopy of size-selected clusters in combination with background gases.

At the end a first measurement of the interaction of supported silver clusters and molecular hydrogen was presented. Hydrogen did not influence the S-SHG signal of the supported clusters. A rapid decrease in S-SHG intensity, however, was observed when silver cluster hydrogen complexes were exposed to kinetic electrons. This decrease and subsequent increase - when the electron current was discontinued - showed the usual exponential character (in contrast to oxygen). Possible explanations for this behavior were given, however further measurements are necessary for a better understanding and clarification of this promising observation.

6

OUTLOOK

In this chapter several suggestions for further measurements which can be performed using the current experimental setup are proposed. Also, small modifications of the experimental setup which would lead to a new field of possible measurements are suggested.

In this thesis it was shown that the employed experimental and spectroscopic setup is sensitive enough to spectroscopically investigate supported size-selected clusters starting with Ag_9. With cluster currents in the range of 20 pA to 30 pA the deposition times were approximately three hours for a sufficient resolution of the nonlinear spectra (this led to a coverage of $\sim 3 \cdot 10^{12}$ clusters/cm^2). Recording these spectra was however always accompanied by enormous experimental work. Higher cluster currents would decrease the deposition times required for this coverage or increase the resolution of the nonlinear spectra. Hence a further optimization or modification of the cluster source towards higher cluster currents of silver would in future lead to smaller errors and probably better resolved spectra. It should then be possible to probe smaller clusters than Ag_9. Also cluster sizes between Ag_9 and Ag_{55} which were not measured within this thesis are of potential interest. Deviations from the universal $1/D$ law which was discussed in section 4.2.1 are interesting and could lead to a better understanding of the structures of the deposited clusters.

Another aspect is the deposition of other metal clusters. As was shown in this thesis, silver clusters are the perfect system for spectroscopic investigations. However, other metals such as gold also exhibit resonance frequencies for small clusters (plasmon resonances), which are not as pronounced as those of silver but are of similar scientific interest. Au clusters e.g. provide considerably higher cluster currents with the experimental setup, which leads to higher coverages for similar deposition times. Their catalytic properties were shown to be size-dependent [10]. This could lead to exciting spectroscopic investigations of small size-selected gold clusters.

The oxidation measurements of small supported silver clusters can be modified in many ways. The preliminary results presented in this thesis are promising and open many new experimental approaches to these kinds of measurements. Firstly, background pressure dependent measurements could be performed for a given cluster size. Secondly, a newly constructed sample holder, where the temperature of the substrate can be varied, would provide temperature dependent measurements. Thirdly, IR-CRD measurements could probe vibrational transition frequencies of adsorbates and hence answer questions about the interactions involved. All of these measurements should lead to a better understanding of the oxidation of small supported size-selected silver clusters and could pave the way for a comprehensive kinetic model. Another interesting aspect concerning the oxidation is the even/odd effect which should influence the oxidation characteristics of small size-selected clusters. Not much is known about the chemical properties of small supported size-selected silver clusters. However, the electronic structure of the clusters is expected to be reflected in the chemical functionality [123].

The most interesting and promising future measurements should certainly lead to the production and proof of supported size-selected chiral clusters. The results of this thesis are a first important step for further chiroptical measurements. In recent years metal nanoparticles, protected by chiral and achiral ligands gained much interest and showed chirality. They possess promising physical and chemical properties in the field of nanotechnology and catalysis [30, 157, 158, 159], however all of these measurements were done in solution. Further investigations of supported chiral molecules, especially in combination with metal clusters or nanoparticles under UHV conditions might allow the preparation of chiral metal nanoparticles or clusters on surfaces, which would be a significant step in the promising field of heterogeneous enantioselective catalysis. The remarkably high value for the difference in rotation angle for two different enantiomers of one molecule provides hope that supported chiral clusters can also be probed in future by this chiroptical nonlinear setup. This enormous chiroptical sensitivity is needed to pave the way for these kind of measurements. However, there are different ways to reach this goal.

One promising way is to induce chirality in size-selected clusters by covalently bound chiral molecules as has been done in solutions [19, 23]. This could be done by either providing a chiral surface, on which size-selected clusters are deposited or by evaporating chiral molecules onto supported size-selected clusters. However, the temperature of the system will be crucial in order to induce chirality. Thus it should be adjustable.

Another approach towards supported chiral clusters would be the evaporation of ligand stabilized chiral clusters from the solid phase. Here the implemented evaporator and quartz-micro-balance would play a central role, however the stability of the complexes need to be ensured. Both ways could be constructive.

Theoretical [20, 21, 160, 161] and experimental [162] approaches lead to the conclusion that some sizes of gold clusters (Au$_{28}$, Au$_{34}^{-}$ Au$_{55}$) should be chiral in the lowest energy configuration. It would be a great measurement to prove these or similar results for supported size-selected clusters by the new chiroptical setup described in this thesis. Here a method must be found to produce and deposit these clusters in a enantiomerically pure form, e.g by providing a chiral surface.

Part VI

BIBLIOGRAPHY

BIBLIOGRAPHY

[1] Roy L. Johnston. *Atomic and Molecular Cluster*. Taylor and Francis, 2002. (Cited on pages 3, 45, 46, and 48.)

[2] T. Arai, K. Mihama, K. Yamamoto, and S. Sugano. *Mesocopic Materials and Clusters Their Physical and Chemical Properties*. Springer, 1999. (Cited on page 3.)

[3] L.A. Dykman and N.G. Khlebtsov. Gold nanoparticles in biology and medicine: Recent advances and prospects. *Acta Naturae*, 3(2):34–55, 2011. (Cited on page 3.)

[4] Gunter Schmid, Monika Baumle, Marcus Geerkens, Ingo Heim, Christoph Osemann, and Thomas Sawitowski. Current and future applications of nanoclusters. *Chem. Soc. Rev.*, 28:179–185, 1999. (Cited on page 3.)

[5] Joshua Jortner. Cluster size effects. *Zeitschrift für Physik D Atoms, Molecules and Clusters*, 24(3):247–275, 1992. (Cited on page 3.)

[6] Karl-Heinz Meiwes-Broer. *Metal Clusters at Surfaces: Structure, Quantum Properties, Physical Chemistry*. Springer, 2000. (Cited on page 3.)

[7] Puru Jena and A. W. Castleman. Clusters: A bridge across the disciplines of physics and chemistry. *Proceedings of the National Academy of Sciences*, 103(28):10560–10569, 2006. (Cited on page 3.)

[8] A. W. Castleman and Puru Jena. Clusters: A bridge across the disciplines of environment, materials science, and biology. *Proceedings of the National Academy of Sciences*, 103(28):10554–10559, 2006. (Cited on page 3.)

[9] B. V. Reddy, S. N. Khanna, and B. I. Dunlap. Giant magnetic moments in 4d clusters. *Phys. Rev. Lett.*, 70:3323–3326, May 1993. (Cited on page 3.)

[10] A. Sanchez, S. Abbet, U. Heiz, W. D. Schneider, H. Haekkinen, R. N. Barnett, and Uzi Landman. When gold is not noble: Nanoscale gold catalysts. *The Journal of Physical Chemistry A*, 103(48):9573–9578, 1999. (Cited on pages 3, 4, and 123.)

[11] Sungsik Lee, Chaoyang Fan, Tianpin Wu, and Scott L. Anderson. CO Oxidation on Aun/TiO2 Catalysts Produced by Size-Selected Cluster Deposition. *Journal of the American Chemical*

Society, 126(18):5682–5683, 2004. PMID: 15125657. (Cited on page 3.)

[12] J. W. Niemantsverdriet and I. Chorkendorff. *Concepts of Modern Catalysis and Kinetics*. Wiley-VCH, 2. edition, 2007. (Cited on page 3.)

[13] Ulrich Heiz. *Nanocatalysis (Nanoscience and Technology)*. Springer Berlin / Heidelberg, 1. edition, 2007. (Cited on page 4.)

[14] Z. Xu, F. S. Xiao, S. K. Purnell, O. Alexeev, S. Kawi, S. E. Deutsch, and B. C. Gates. Size-dependent catalytic activity of supported metal clusters. *Nature*, 372(6504):346–348, 11 1994. (Cited on page 4.)

[15] U. Heiz, A. Sanchez, S. Abbet, and W.-D. Schneider. Catalytic oxidation of carbon monoxide on monodispersed platinum clusters: Each atom counts. *Journal of the American Chemical Society*, 121(13):3214–3217, 1999. (Cited on page 4.)

[16] S. Abbet, A. Sanchez, U. Heiz, W.-D. Schneider, A.M. Ferrari, G. Pacchioni, and N. Rösch. Size-effects in the acetylene cyclotrimerization on supported size-selected Pdn clusters (1<n<30). *Surface Science*, 454–456(0):984 – 989, 2000. (Cited on page 4.)

[17] Avelino Corma, Patricia Concepcion, Mercedes Boronat, Maria J. Sabater, Javier Navas, Miguel Jose Yacaman, Eduardo Larios, Alvaro Posadas, M. Arturo Lopez-Quintela, David Buceta, Ernest Mendoza, Gemma Guilera, and Alvaro Mayoral. Exceptional oxidation activity with size-controlled supported gold clusters of low atomicity. *Nat Chem*, 5(9):775–781, 09 2013. (Cited on page 4.)

[18] T. Gregory Schaaff, Grady Knight, Marat N. Shafigullin, Raymond F. Borkman, and Robert L. Whetten. Isolation and selected properties of a 10.4 kda gold:glutathione cluster compound. *The Journal of Physical Chemistry B*, 102(52):10643–10646, 1998. (Cited on page 4.)

[19] Mostafa Farrag, Martin Tschurl, and Ulrich Heiz. Chiral gold and silver nanoclusters: Preparation, size selection, and chiroptical properties. *Chemistry of Materials*, 25(6):862–870, 2013. (Cited on pages 4 and 124.)

[20] I. L. Garzon, J. A. Reyes-Nava, J. I. Rodriguez-Hernandez, I. Sigal, M. R. Beltran, and K. Michaelian. Chirality in bare and passivated gold nanoclusters. *Phys. Rev. B*, 66:073403, Aug 2002. (Cited on pages 4 and 124.)

[21] I. L. Garzon, M. R. Beltran, G. Gonzalez, I. Gutierrez-Gonzalez, K. Michaelian, J. A. Reyes-Nava, and J. I. Rodriguez-Hernandez. Chirality, defects, and disorder in gold clusters. 24(1):105–109, 2003. (Cited on pages 4 and 124.)

[22] Michael-Rock Goldsmith, Christopher B. George, Gerard Zuber, Ron Naaman, David H. Waldeck, Peter Wipf, and David N. Beratan. The chiroptical signature of achiral metal clusters induced by dissymmetric adsorbates. *Phys. Chem. Chem. Phys.*, 8:63–67, 2006. (Cited on page 4.)

[23] Mostafa Farrag. *Preparation of Monolayer-Protected Gold and Silver Nanoclusters and their Optical, Chiroptical and Photochemical Properties*. PhD thesis, Technische Universität München, 2013. (Cited on pages 4 and 124.)

[24] Georgios Kyriakou, Simon K. Beaumont, and Richard M. Lambert. Aspects of heterogeneous enantioselective catalysis by metals. *Langmuir*, 27(16):9687–9695, 2011. (Cited on page 4.)

[25] Martin Thämer. *Linear and Nonlinear Surface Spectroscopy of Supported Size Selected Metal Clusters and Organic Molecules*. PhD thesis, 2012. (Cited on pages 4, 6, 20, 21, 33, 38, 39, 40, 41, 43, 44, 55, 63, 64, 67, 88, 89, 95, 96, 99, 101, 102, 119, and 150.)

[26] Walt A. de Heer, Kathy Selby, Vitaly Kresin, Jun Masui, Michael Vollmer, A. Chatelain, and W. D. Knight. Collective dipole oscillations in small sodium clusters. *Phys. Rev. Lett.*, 59:1805–1808, Oct 1987. (Cited on page 4.)

[27] Josef Tiggesbaumker and Frank Stienkemeier. Formation and properties of metal clusters isolated in helium droplets. *Physical Chemistry Chemical Physics*, 9(34):4748–4770, 2007. (Cited on page 4.)

[28] Michael Vollmer Uwe Kreibig. *Optical Properties of Metal Clusters*. Springer-Verlag, 1995. (Cited on pages 5, 33, 34, 35, 36, 37, 38, 40, 41, and 45.)

[29] Aras Kartouzian. *Optical properties of size-selected supported metal clusters measured by cavity ring-down spectroscopy*. Technische Universität München, 2010. (Cited on pages 5, 55, 56, 63, and 88.)

[30] Cyrille Gautier and Thomas Bürgi. Chiral gold nanoparticles. *ChemPhysChem*, 10(3):483–492, 2009. (Cited on pages 5 and 124.)

[31] J. Tiggesbäumker, L. Köller, H. O. Lutz, and K. H. Meiwes-Broer. Giant resonances in silver-cluster photofragmentation. *Chemical Physics Letters*, 190(1–2):42–47, 2 1992. (Cited on pages 5 and 46.)

[32] V. Kasperovich and V. V. Kresin. Ultraviolet photoabsorption spectra of silver and gold nanoclusters. *Philosophical Magazine Part B*, 78(4):385–396, 1998. (Cited on pages 5 and 47.)

[33] W. Harbich, S. Fedrigo, and J. Buttet. The optical absorption spectra of small silver clusters (n=8–39) embedded in rare gas matrices. *Zeitschrift für Physik D Atoms, Molecules and Clusters*, 26(1):138–140, 1993. (Cited on pages 5, 47, 103, 104, and 105.)

[34] W. Harbich, S. Fedrigo, and J. Buttet. The optical absorption spectra of small silver clusters (n=5–11) embedded in argon matrices. *Chemical Physics Letters*, 195(5–6):613 – 617, 1992. (Cited on page 5.)

[35] S. Lecoultre, A. Rydlo, J. Buttet, C. Félix, S. Gilb, and W. Harbich. Ultraviolet-visible absorption of small silver clusters in neon: Agn (n = 1–9). *The Journal of Chemical Physics*, 134(18):–, 2011. (Cited on page 5.)

[36] S. Fedrigo, W. Harbich, and J. Buttet. Collective dipole oscillations in small silver clusters embedded in rare-gas matrices. *Phys. Rev. B*, 47:10706–10715, Apr 1993. (Cited on pages 5, 47, 104, and 105.)

[37] Christine M. Aikens, Shuzhou Li, and George C. Schatz. From Discrete Electronic States to Plasmons: TDDFT Optical Absorption Properties of Ag n (n = 10, 20, 35, 56, 84, 120) Tetrahedral Clusters. *The Journal of Physical Chemistry C*, 112(30):11272–11279, 2008. (Cited on pages 5, 48, and 103.)

[38] Jonathan A. Scholl, Ai Leen Koh, and Jennifer A. Dionne. Quantum plasmon resonances of individual metallic nanoparticles. *Nature*, 483(7390):421–427, 03 2012. (Cited on pages 5, 34, 39, 41, 103, and 105.)

[39] N. Nilius, N. Ernst, and H.-J. Freund. Photon emission spectroscopy of individual oxide-supported silver clusters in a scanning tunneling microscope. *Phys. Rev. Lett.*, 84:3994–3997, Apr 2000. (Cited on pages 5, 41, 42, 90, 93, 100, 103, 104, and 106.)

[40] Sonja Sioncke, Thierry Verbiest, and Andre Persoons. Second-order nonlinear optical properties of chiral materials. *Materials Science and Engineering: R: Reports*, 42:115 – 155, 2003. (Cited on pages 11, 15, 21, 23, and 27.)

[41] Thierry Verbiest, Koen Clays, and Vincent Rodriguez. *Second-Order Nonlinear Optical Characterization Techniques An Introduction*. CRC Press, 2009. (Cited on pages 11, 21, 23, and 26.)

[42] R.W. Boyd. *Nonlinear Optics*. Nonlinear Optics Series. Elsevier Science, 2008. (Cited on pages 11, 16, and 17.)

[43] Y.R. Shen. *The principles of nonlinear optics*. Wiley classics library. Wiley-Interscience, 2003. (Cited on pages 11 and 31.)

[44] Pierre-Francois Brevet. *Surface Second Harmonic Generation*. Presses polytechniques et universitaires romandes, 1997. (Cited on page 11.)

[45] Vladimir G. Bordo and Horst-Günter Rubahn. *Optics and Spectroscopy at Surfaces and Interfaces*. Wiley-VCH, 2005. (Cited on pages 11 and 48.)

[46] J. Clerk Maxwell. A dynamical theory of the electromagnetic field. *Philosophical Transactions of the Royal Society of London*, 155:459–512, 1865. (Cited on page 11.)

[47] Christoph Logé and Ulrich Boesl. Laser mass spectrometry with circularly polarized light: Circular dichroism of molecular ions. *ChemPhysChem*, 13(18):4218–4223, 2012. (Cited on page 14.)

[48] Christoph Loge and Ulrich Boesl. Laser mass spectrometry with circularly polarized light: two-photon circular dichroism. *Phys. Chem. Chem. Phys.*, 14:11981–11989, 2012. (Cited on page 14.)

[49] K. Nakanishi, N. Berova, and R. Woody. *Circular Dichroism: Principles and Applications*. VCH, 1994. (Cited on page 14.)

[50] F. Hache, H. Mesnil, and M. C. Schanne-Klein. Application of classical models of chirality to surface second harmonic generation. *The Journal of Chemical Physics*, 115(14):6707–6715, 2001. (Cited on pages 15, 29, and 75.)

[51] Andre Persoons. Nonlinear optics, chirality, magneto-optics: a serendipitous road. *Opt. Mater. Express*, 1(1):5–16, May 2011. (Cited on page 16.)

[52] Bahaa E.A. Saleh and Malvin Carl Teich. *Grundlagen der Photonik*. WILEY-VCH Verlag, 2008. (Cited on page 16.)

[53] J. Eichler and H.J. Eichler. *Laser, Bauformen, Strahlführung, Anwendungen*. Springer, 2010. (Cited on page 16.)

[54] P. M. Rentzepis, J. A. Giordmaine, and K. W. Wecht. Coherent optical mixing in optically active liquids. *Phys. Rev. Lett.*, 16:792–794, May 1966. (Cited on page 21.)

[55] Y R Shen. Optical second harmonic generation at interfaces. *Annual Review of Physical Chemistry*, 40(1):327–350, 1989. (Cited on page 22.)

[56] N. Bloembergen and P. S. Pershan. Light waves at the boundary of nonlinear media. *Phys. Rev.*, 128:606–622, Oct 1962. (Cited on page 22.)

[57] Victor Mizrahi and J. E. Sipe. Phenomenological treatment of surface second-harmonic generation. *J. Opt. Soc. Am. B*, 5(3):660–667, Mar 1988. (Cited on page 22.)

[58] T. F. Heinz, C. K. Chen, D. Ricard, and Y. R. Shen. Spectroscopy of Molecular Monolayers by Resonant Second-Harmonic Generation. *Phys. Rev. Lett.*, 48(7):478–481, Feb 1982. (Cited on page 22.)

[59] T. F. Heinz, H. W. K. Tom, and Y. R. Shen. Determination of molecular orientation of monolayer adsorbates by optical second-harmonic generation. *Phys. Rev. A*, 28:1883–1885, Sep 1983. (Cited on pages 22 and 31.)

[60] Martti Kauranen, Thierry Verbiest, Sven van Elshocht, and Andre Persoons. Chirality in surface nonlinear optics. *Optical Materials*, 9:286–294, 1998. (Cited on page 23.)

[61] M. C. Schanne-Klein, F. Hache, A. Roy, C. Flytzanis, and C. Payrastre. Off resonance second order optical activity of isotropic layers of chiral molecules: Observation of electric and magnetic contributions. *The Journal of Chemical Physics*, 108(22):9436–9443, 1998. (Cited on page 23.)

[62] Martti Kauranen, Jeffery J. Maki, Thierry Verbiest, Sven Van Elshocht, and Andre Persoons. Quantitative determination of electric and magnetic second-order susceptibility tensors of chiral surfaces. *Phys. Rev. B*, 55:R1985–R1988, Jan 1997. (Cited on page 23.)

[63] Peer Fischer and François Hache. Nonlinear optical spectroscopy of chiral molecules. *Chirality*, 17(8):421–437, 2005. (Cited on pages 23 and 29.)

[64] Jeffrey D. Byers and Janice M. Hicks. Electronic spectral effects on chiral surface second harmonic generation. *Chemical Physics Letters*, 231(2–3):216–224, 1994. (Cited on pages 26, 29, 31, 75, and 84.)

[65] Martti Kauranen, Thierry Verbiest, Jeffery J. Maki, and Andre Persoons. Second-harmonic generation from chiral surfaces. *The Journal of Chemical Physics*, 101(9):8193–8199, 1994. (Cited on pages 26 and 75.)

[66] J. D. Byers, H. I. Yee, and J. M. Hicks. A second harmonic generation analog of optical rotatory dispersion for the study of

chiral monolayers. *The Journal of Chemical Physics*, 101(7):6233–6241, 1994. (Cited on pages 29, 32, 33, and 75.)

[67] J. D. Byers, H. I. Yee, T. Petralli-Mallow, and J. M. Hicks. Second-harmonic generation circular-dichroism spectroscopy from chiral monolayers. *Phys. Rev. B*, 49:14643–14647, May 1994. (Cited on pages 29, 31, and 75.)

[68] M.C Schanne-Klein, T Boulesteix, F Hache, M Alexandre, G Lemercier, and C Andraud. Strong chiroptical effects in surface second harmonic generation obtained for molecules exhibiting excitonic coupling chirality. *Chemical Physics Letters*, 362(1–2):103 – 108, 2002. (Cited on page 29.)

[69] Wikipedia.com. (Cited on page 30.)

[70] Rainer Kassing, Plamen Petkov, Wilhelm Kulisch, Cyril Popov, U. Kreibig, M. Gartz, A. Hilger, H. Hövel, M. Quinten, D. Wagner, and H. Ditlbacher. *Nato Science Series*, volume 223, pages 75–110. Springer Netherlands, 2006. (Cited on pages 33, 36, 37, 40, 48, 50, and 106.)

[71] Almuth Hilger. *Grenzflächen-Analyse durch Mie-Plasmon-Spektroskopie an Edelmetallclustern*. PhD thesis, RWTH Aachen, Feb 2001. (Cited on page 33.)

[72] Craig F. Bohren and Donald R. Huffman. *Absorption and Scattering of Light by Small Particles*. Wiley-VCH, 2004. (Cited on pages 33, 35, 38, and 40.)

[73] P. Drude. Zur Elektronentheorie der Metalle. *Annalen der Physik*, 306(3):566–613, 1900. (Cited on page 34.)

[74] H. Ehrenreich and H. R. Philipp. Optical Properties of Ag and Cu. *Phys. Rev.*, 128:1622–1629, Nov 1962. (Cited on page 36.)

[75] P. B. Johnson and R. W. Christy. Optical constants of the noble metals. *Phys. Rev. B*, 6:4370–4379, Dec 1972. (Cited on pages 36 and 37.)

[76] G. B. Irani, T. Huen, and F. Wooten. Optical Properties of Ag and Alpha-Phase Ag-Al Alloys. *Phys. Rev. B*, 3:2385–2390, Apr 1971. (Cited on page 36.)

[77] Tobias Lünskens. *Second-Harmonic-Generation-Spectroscopy of surface complexes*. Master-Thesis. Technische Universität München, 2012. (Cited on pages 36, 42, 43, 44, 45, 88, 91, 107, and 150.)

[78] G. Mie. Beiträge zur Optik trüber Medien, speziell kolloidaler Metalllösungen. *Annalen der Physik*, 330(3):377–445, 1908. (Cited on pages 37 and 117.)

[79] Erwin David. Deutung der Anomalien der optischen Konstanten dünner Metallschichten. 114(7-8):389–406, 1939. (Cited on page 38.)

[80] Sadafumi Yoshida, Tomuo Yamaguchi, and Akira Kinbara. Determination of the inter-island dielectric constant in aggregated silver films, by measurement of optical plasma resonance absorption. *J. Opt. Soc. Am.*, 62(12):1415–1419, Dec 1972. (Cited on page 38.)

[81] Monique Rasigni and Georges Rasigni. Optical properties of aggregated lithium deposits. *J. Opt. Soc. Am.*, 67(4):510–519, Apr 1977. (Cited on page 38.)

[82] Martin Thämer, Aras Kartouzian, Philipp Heister, Tobias Lünskens, Sabine Gerlach, and Ulrich Heiz. Small supported plasmonic silver clusters. *Small*, pages n/a–n/a, 2014. (Cited on pages 38, 41, 44, 88, 89, 95, 96, and 102.)

[83] U. Kreibig and C. v. Fragstein. The limitation of electron mean free path in small silver particles. 224(4):307–323, 1969. (Cited on page 39.)

[84] U. Kreibig and L. Genzel. Optical absorption of small metallic particles. *Surface Science*, 156, Part 2(0):678–700, 1985. (Cited on page 40.)

[85] A. Liebsch. Surface-plasmon dispersion and size dependence of mie resonance: Silver versus simple metals. *Phys. Rev. B*, 48:11317–11328, Oct 1993. (Cited on page 40.)

[86] B.N.J. Persson. Polarizability of small spherical metal particles: influence of the matrix environment. *Surface Science*, 281(1–2):153 – 162, 1993. (Cited on pages 40, 41, and 91.)

[87] U. Kreibig, M. Gartz, A. Hilger, and R. Neuendorf. Interfaces in nanostructures: optical investigations on cluster-matter. *Nanostructured Materials*, 11(8):1335 – 1342, 1999. (Cited on pages 41, 42, and 50.)

[88] K.-P. Charlé, L. König, S. Nepijko, I. Rabin, and W. Schulze. The Surface Plasmon Resonance of Free and Embedded Ag-Clusters in the Size Range 1,5 nm < D < 30 nm. *Crystal Research and Technology*, 33(7-8):1085–1096, 1998. (Cited on pages 41, 93, 103, 104, and 105.)

[89] A. Hilger, N. Cüppers, M. Tenfelde, and U. Kreibig. Surface and interface effects in the optical properties of silver nanoparticles. 10(1):115–118, 2000. (Cited on pages 42 and 102.)

[90] U. Kreibig, G. Bour, A. Hilger, and M. Gartz. Optical properties of cluster–matter: Influences of interfaces. *physica status solidi (a)*, 175(1):351–366, 1999. (Cited on pages 42 and 43.)

[91] H. Hövel, S. Fritz, A. Hilger, U. Kreibig, and M. Vollmer. Width of cluster plasmon resonances: Bulk dielectric functions and chemical interface damping. *Phys. Rev. B*, 48:18178–18188, 1993. (Cited on pages 42 and 43.)

[92] B. N. J. Persson and A. Baratoff. Theory of photon emission in electron tunneling to metallic particles. *Phys. Rev. Lett.*, 68:3224–3227, May 1992. (Cited on page 43.)

[93] E. Zaremba and B. N. J. Persson. Dynamic polarizability of small metal particles. *Phys. Rev. B*, 35:596–606, Jan 1987. (Cited on page 43.)

[94] U. Kreibig. Interface-induced dephasing of Mie plasmon polaritons. 93(1):79–89, 2008. (Cited on page 43.)

[95] Prashant K. Jain, Wenyu Huang, and Mostafa A. El-Sayed. On the universal scaling behavior of the distance decay of plasmon coupling in metal nanoparticle pairs: A plasmon ruler equation. *Nano Letters*, 7(7):2080–2088, 2007. (Cited on pages 43 and 91.)

[96] W. Rechberger, A. Hohenau, A. Leitner, J.R. Krenn, B. Lamprecht, and F.R. Aussenegg. Optical properties of two interacting gold nanoparticles. *Optics Communications*, 220(1–3):137 – 141, 2003. (Cited on pages 43 and 91.)

[97] Thearith Ung, Luis M. Liz-Marzán, and Paul Mulvaney. Optical Properties of Thin Films of Au@SiO2 Particles. *The Journal of Physical Chemistry B*, 105(17):3441–3452, 2001. (Cited on page 43.)

[98] M. Quinten, U. Kreibig, D. Schönauer, and L. Genzel. Optical absorption spectra of pairs of small metal particles. *Surface Science*, 156, Part 2(0):741 – 750, 1985. (Cited on pages 43 and 91.)

[99] B. N. J. Persson and A. Liebsch. Optical properties of two-dimensional systems of randomly distributed particles. *Phys. Rev. B*, 28(8):4247–4254, 1983. (Cited on page 43.)

[100] T. Yamaguchi, S. Yoshida, and A. Kinbara. Optical effect of the substrate on the anomalous absorption of aggregated silver films. *Thin Solid Films*, 21(1):173 – 187, 1974. (Cited on page 43.)

[101] P. Royer, J.L. Bijeon, J.P. Goudonnet, T. Inagaki, and E.T. Arakawa. Optical absorbance of silver oblate particles: Substrate and shape effects. *Surface Science*, 217(1–2):384 – 402, 1989. (Cited on pages 43 and 44.)

[102] H. Hövel, A. Hilger, and U. Kreibig I. Nusch. Experimental determination of deposition induced cluster deformation. *Z. Phys. D*, 42(203-208), 1997. (Cited on page 44.)

[103] W. D. Knight, Keith Clemenger, Walt A. de Heer, Winston A. Saunders, M. Y. Chou, and Marvin L. Cohen. Electronic shell structure and abundances of sodium clusters. *Phys. Rev. Lett.*, 52:2141–2143, Jun 1984. (Cited on page 45.)

[104] Z. Penzar and W. Ekardt. Electronic shell structure and metal clusters: the self-consistent spheroidal jellium model. 17(1):69–72, 1990. (Cited on page 45.)

[105] Marvin L. Cohen and Walter D. Knight. The physics of metal clusters. *AIP*, 43(12)(42), 1990. (Cited on page 45.)

[106] Ian Michael Goldby. *Dynamics of Molecules and Clusters at Surfaces*. PhD thesis, Clare College Cambridge, 1996. (Cited on page 46.)

[107] C. Jackschath, I. Rabin, and W. Schulze. Electron impact ionization of silver clusters Ag n ,n 36. 22(2):517–520, 1992. (Cited on page 46.)

[108] H. Grönbeck and A. Rosén. Analysis of the odd-even alternation in simple metal clusters. 36(2):153–157, 1996. (Cited on page 46.)

[109] O. Echt, K. Sattler, and E. Recknagel. Magic numbers for sphere packings: Experimental verification in free xenon clusters. *Phys. Rev. Lett.*, 47:1121–1124, Oct 1981. (Cited on page 46.)

[110] T.P. Martin, S. Bjørnholm, J. Borggreen, C. Bréchignac, Ph. Cahuzac, K. Hansen, and J. Pedersen. Electronic shell structure of laser-warmed Na clusters. *Chemical Physics Letters*, 186(1):53 – 57, 1991. (Cited on page 46.)

[111] A. L. Mackay. A dense non-crystallographic packing of equal spheres. *Acta Crystallographica*, 15(9):916–918, Sep 1962. (Cited on page 46.)

[112] T.P. Martin, T. Bergmann, H. Göhlich, and T. Lange. Observation of electronic shells and shells of atoms in large Na clusters. *Chemical Physics Letters*, 172(3–4):209 – 213, 1990. (Cited on page 46.)

[113] Josef Tiggesbäumker, Lars Köller, Karl-Heinz Meiwes-Broer, and Ansgar Liebsch. Blue shift of the Mie plasma frequency in Ag clusters and particles. *Phys. Rev. A*, 48:R1749–R1752, Sep 1993. (Cited on pages 46, 47, 99, 103, and 104.)

[114] W. Harbich, S. Fedrigo, F. Meyer, D. M. Lindsay, J. Lignieres, J. C. Rivoal, and D. Kreisle. Deposition of mass selected silver clusters in rare gas matrices. *The Journal of Chemical Physics*, 93(12):8535–8543, 1990. (Cited on page 47.)

[115] K. Yabana and G. F. Bertsch. Optical response of small silver clusters. *Phys. Rev. A*, 60:3809–3814, Nov 1999. (Cited on page 47.)

[116] Vlasta Bonačić-Koutecky, Vincent Veyret, and Roland Mitrić. Ab initio study of the absorption spectra of Agn (n=5–8) clusters. *The Journal of Chemical Physics*, 115(22):10450–10460, 2001. (Cited on pages 47 and 103.)

[117] Constantin Alexander Walenta. SHG spectroscopy of supported silver clusters. Master thesis, Technische Universität München, August 2013. (Cited on pages 48, 55, 57, 61, 69, 153, 154, and 155.)

[118] M. Schmidt, A. Masson, and C. Bréchignac. Oxygen and silver clusters: Transition from chemisorption to oxidation. *Phys. Rev. Lett.*, 91:243401, Dec 2003. (Cited on pages 48, 49, and 110.)

[119] Charles T. Campbell. Atomic and molecular oxygen adsorption on Ag(111). *Surface Science*, 157(1):43 – 60, 1985. (Cited on pages 48 and 110.)

[120] T. Götz, M. Buck, C. Dressler, F. Eisert, and F. Träger. Optical second-harmonic generation by supported metal clusters: Size and shape effects. 60(6):607–612, 1995. (Cited on pages 49 and 107.)

[121] Liana D. Socaciu, Jan Hagen, Ueli Heiz, Thorsten M. Bernhardt, Thomas Leisner, and Ludger Wöste. Reaction mechanism for the oxidation of free silver dimers. *Chemical Physics Letters*, 340(3-4):282–288, 2001. (Cited on page 49.)

[122] Jan Hagen, Liana D. Socaciu, Jérôme Le Roux, Denisia Popolan, Thorsten M. Bernhardt, Ludger Wöste, Roland Mitrić, Holger Noack, and Vlasta Bonačić-Koutecký. Cooperative effects in the activation of molecular oxygen by anionic silver clusters. *Journal of the American Chemical Society*, 126(11):3442–3443, 2004. PMID: 15025469. (Cited on page 49.)

[123] Liana D. Socaciu, Jan Hagen, Jérôme Le Roux, Denisia Popolan, Thorsten M. Bernhardt, Ludger Wöste, and Štefan Vajda. Strongly cluster size dependent reaction behavior of CO with O2 on free silver cluster anions. *The Journal of Chemical Physics*, 120(5):2078–2081, 2004. (Cited on pages 49 and 124.)

[124] Thorsten M. Bernhardt. Gas-phase kinetics and catalytic reactions of small silver and gold clusters. *International Journal of Mass Spectrometry*, 243(1):1–29, 2005. (Cited on page 49.)

[125] Matthias Hillenkamp, Giulia Di Domenicantonio, Olivier Eugster, and Christian Félix. Instability of Ag nanoparticles in SiO2 at ambient conditions. *Nanotechnology*, 18:015702, 2007. (Cited on page 50.)

[126] S.H. Jeong, D.C. Lim, J.-H. Boo, S.B. Lee, H.N. Hwang, C.C. Hwang, and Y.D. Kim. Interaction of silver with oxygen on sputtered pyrolytic graphite. *Applied Catalysis A: General*, 320(0):152–158, Jan 2007. (Cited on page 50.)

[127] Wei Gan, Bolei Xu, and Hai-Lung Dai. Activation of Thiols at a Silver Nanoparticle Surface. *Angewandte Chemie International Edition*, 50(29):6622–6625, 2011. (Cited on page 50.)

[128] Wei Gan, Grazia Gonella, Min Zhang, and Hai-Lung Dai. Communication: Reactions and adsorption at the surface of silver nanoparticles probed by second harmonic generation. *The Journal of Chemical Physics*, 134(4):041104, 2011. (Cited on page 50.)

[129] Sabine Gerlach. *nonlinear enantioselective spectroscopy of 1,1'bi-2-naphtol on BK7*. Master-Thesis. 2012. (Cited on pages 55, 65, 78, 153, 154, and 155.)

[130] U. Heiz, F. Vanolli, L. Trento, and W. Schneider. Chemical reactivity of size-selected supported clusters: An experimental setup. *Review of Scientific Instruments*, 68(5):1986–1994, 1997. (Cited on page 55.)

[131] E. Schumacher U.Heiz, A. Vayloyan. A new cluster source for the genearion of binary metal clusters. *Review of Scientific Instruments*, 68:3718, 1997. (Cited on page 56.)

[132] C. Lu and A.W. Czanderna. *Applications of Piezoelectric Quartz Crystal Microbalances*. Methods and Phenomena. Elsevier Science, 1984. (Cited on page 59.)

[133] Diethelm Johannsmann. Modeling of qcm data. (Cited on page 59.)

[134] Günter Sauerbrey. Verwendung von Schwingquarzen zur Wägung dünner Schichten und zur Mikrowägung. *Zeitschrift für Physik*, 155(2):206–222, 1959. (Cited on page 59.)

[135] D. R. Denison. Linearity of a heavily loaded quartz crystal microbalance. *Journal of Vacuum Science and Technology*, 10(1):126–129, 1973. (Cited on page 60.)

[136] Constantin Alexander Walenta. SHG-spectroscopy of size-selected silver clusters on glass surfaces. Bachelor's Thesis, Oct 2011. (Cited on page 63.)

[137] Simon Rittmeyer. SHG-ORD von geträgertem BINOL. Research internship report, Jun 2012. (Cited on page 65.)

[138] Bo Wang, Bokwon Yoon, Michael König, Yves Fukamori, Friedrich Esch, Ueli Heiz, and Uzi Landman. Size-Selected Monodisperse Nanoclusters on Supported Graphene: Bonding, Isomerism, and Mobility. *Nano Letters*, 12(11):5907–5912, 2012. (Cited on page 69.)

[139] A.S. Crampton. Electron spectroscopy with metastable atoms - new insights into classical systems and promise for size-selected clusters. Master's thesis, Technische Universität München, 2011. (Cited on page 69.)

[140] Aras Kartouzian, Philipp Heister, Martin Thämer, Sabine Gerlach, and Ulrich Heiz. In-line reference measurement for surface second harmonic generation spectroscopy. *J. Opt. Soc. Am. B*, 30(3):541–548, Mar 2013. (Cited on pages 70, 77, 78, 119, 157, and 158.)

[141] Philipp Heister, Tobias Lunskens, Martin Thamer, Aras Kartouzian, Sabine Gerlach, Thierry Verbiest, and Ueli Heiz. Orientational changes of supported chiral 2,2'-dihydroxy-1,1'binaphthyl molecules. *Phys. Chem. Chem. Phys.*, 16:7299–7306, 2014. (Cited on pages 75 and 120.)

[142] Jean Michel Brunel. Binol: A versatile chiral reagent. *Chemical Reviews*, 105(11):4233–4233, 2005. (Cited on page 75.)

[143] L. Persechini and J. F. McGilp. Chiral second-harmonic generation from small organic molecules at surfaces. *physica status solidi (b)*, 249(6):1155–1159, 2012. (Cited on page 75.)

[144] MA Kriech and JC Conboy. Imaging chirality with surface second harmonic generation microscopy. *Journal of the American Chemical Society*, 127(9):2834–2835, 03 2005. (Cited on page 75.)

[145] Sven Van Elshocht, Thierry Verbiest, Martti Kauranen, Andre Persoons, B. M. W. Langeveld-Voss, and E. W. Meijer. Direct evidence of the failure of electric-dipole approximation in second-harmonic generation from a chiral polymer film. *The Journal of Chemical Physics*, 107(19):8201–8203, 1997. (Cited on page 75.)

[146] Maritti Kauranen, Thierry Verbiest, and Andre Persoons. Chiral materials in second-order nonlinear optics. *Journal of Nonlinear Optical Physics and Materials*, 08(02):171–189, 1999. (Cited on page 75.)

[147] M. Vanbel, S. Vandendriessche, M. A. van der Veen, D. Slavov, P. Heister, R. Paesen, V. K. Valev, M. Ameloot, and T. Verbiest. Second-harmonic generation from complex chiral samples, 2013. (Cited on page 79.)

[148] Monique A. van der Veen, Frederik Vermoortele, Dirk E. De Vos, and Thierry Verbiest. Point group symmetry determination via observables revealed by polarized second-harmonic generation microscopy: (1) theory. *Analytical Chemistry*, 84(15):6378–6385, 2012. (Cited on page 79.)

[149] Monique A. van der Veen, Frederik Vermoortele, Dirk E. De Vos, and Thierry Verbiest. Point group symmetry determination via observables revealed by polarized second-harmonic generation microscopy: (2) applications. *Analytical Chemistry*, 84(15):6386–6390, 2012. (Cited on page 79.)

[150] Martin Thämer, Aras Kartouzian, Philipp Heister, Sabine Gerlach, Martin Tschurl, Ulrich Boesl, and Ulrich Heiz. Linear and nonlinear laser spectroscopy of surface adsorbates with sub-monolayer sensitivity. *The Journal of Physical Chemistry C*, 116(15):8642–8648, 2012. (Cited on pages 88, 89, and 150.)

[151] K. P. Charlé, W. Schulze, and B. Winter. The size dependent shift of the surface plasmon absorption band of small spherical metal particles. 12(1-4):471–475, 1989. (Cited on pages 93, 103, and 104.)

[152] M. H. Schaffner, F. Patthey, and W. D. Schneider. Size-selected Agn and Cun clusters supported on MgO(100) films. 9(1):609–612, 1999. (Cited on page 95.)

[153] Hellmut Haberland. Looking from both sides. *Nature*, 494(7435):E1–E2, 02 2013. (Cited on pages 99 and 105.)

[154] T. Wenzel, J. Bosbach, F. Stietz, and F. Träger. In situ determination of the shape of supported silver clusters during growth. *Surface Science*, 432(3):257 – 264, 1999. (Cited on page 102.)

[155] G. F. Zhao, Y. Lei, and Z. Zeng. Absorption spectra of small silver clusters agn (n = 4, 6, 8): A tddft study. *Chemical Physics*, 327(2–3):261–268, 9 2006. (Cited on page 103.)

[156] L. T. Hudson, N. H. Tolk, C. Bao, P. Nordlander, D. P. Russell, and J. Xu. Electron- and photon-stimulated desorption of atomic hydrogen from radiation-modified alkali halide surfaces. *Phys. Rev. B*, 62:10535–10543, Oct 2000. (Cited on page 112.)

[157] Igor Dolamic, Stefan Knoppe, Amala Dass, and Thomas Bürgi. First enantioseparation and circular dichroism spectra of Au38

clusters protected by achiral ligands. *Nat Commun*, 3:798, 04 2012. (Cited on page 124.)

[158] Mostafa Farrag, Martin Tschurl, Amala Dass, and Ulrich Heiz. Infra-red spectroscopy of size selected Au25, Au38 and Au144 ligand protected gold clusters. *Phys. Chem. Chem. Phys.*, 15:12539–12542, 2013. (Cited on page 124.)

[159] Cecilia Noguez and Ignacio L. Garzon. Optically active metal nanoparticles. *Chem. Soc. Rev.*, 38:757–771, 2009. (Cited on page 124.)

[160] Xochitl Lopez-Lozano, Luis A. Perez, and Ignacio L. Garzon. Enantiospecific adsorption of chiral molecules on chiral gold clusters. *Phys. Rev. Lett.*, 97:233401, Dec 2006. (Cited on page 124.)

[161] Anne Lechtken, Detlef Schooss, Jason R. Stairs, Martine N. Blom, Filipp Furche, Nina Morgner, Oleg Kostko, Bernd von Issendorff, and Manfred M. Kappes. Au34-: A chiral gold cluster? *Angewandte Chemie International Edition*, 46(16):2944–2948, 2007. (Cited on page 124.)

[162] Z.W. Wang and R. E. Palmer. Experimental Evidence for Fluctuating, Chiral-Type Au55 Clusters by Direct Atomic Imaging. *Nano Letters*, 12(11):5510–5514, 2012. (Cited on page 124.)

[163] A. Kartouzian, M. Thamer, T. Soini, J. Peter, P. Pitschi, S. Gilb, and U. Heiz. Cavity ring-down spectrometer for measuring the optical response of supported size-selected clusters and surface defects in ultrahigh vacuum. *Journal of Applied Physics*, 104(12):124313, 2008. (Cited on page 150.)

[164] Dr Roberatas Kananavicius. *PL2250 Series Laser - Technical Description and User's Manual*. EKSPLA, Savanoriu Ave 231, LT-02300 Vilnius, Lithuania, 2012. (Cited on page 153.)

Part VII

APPENDIX

A

SOFTWARE

In this chapter the hard- and software, which was used during the work for this thesis is presented. First, the general hard- and software connections are shown, then two LabVIEW programs, which were programmed during this work are introduced. These were of great importance for the daily work in laboratory and are explained in greater detail.

A.1 DATA CONNECTIONS

Important parts of the experimental setup are driven by computers and are described in the following. In Figure 54 a schematic overview of the used soft- and hardware and their connections is shown. On PC1 the main LabVIEW program (lab program: Section A.2.2) is installed. It is connected to the oscilloscope where the signals (from the PMT and the photodiode) are stored. Here, a second LabVIEW program is installed in order to provide a fast data transfer between PC1 and the oscilloscope. PC1 is also connected to the monochromator, the rotatable Pellin-Broca prisms, the rotatable Fresnel rhomb as well as to the ps-lasersystem and the ns-lasersystem. PC2 is used to operate both the QMS (Extrel 5500, Merlin 3.0) for the size selection of the clusters and the QMS (RGA, Stanford Research Systems RGA 300) for the control of the residual gases in the chamber. Mass spectra[1] of size-selected clusters as well as mass spectra of the background pressure in the analysis chamber are stored on this computer. PC3 is used to monitor the pressure in the different chambers (see Section A.2.1). PC4 and Laptop2 are used to operate the ns-lasersystem and the evaporation laser, respectively. On Laptop1 software for the QMB, the Beam-Profiler and a spectrometer are installed. Data from the evaporation processes are stored on this computer.

---

[1] For mass spectra of size-selected clusters the picoamperemeter is connected to PC2. See Figure 20.

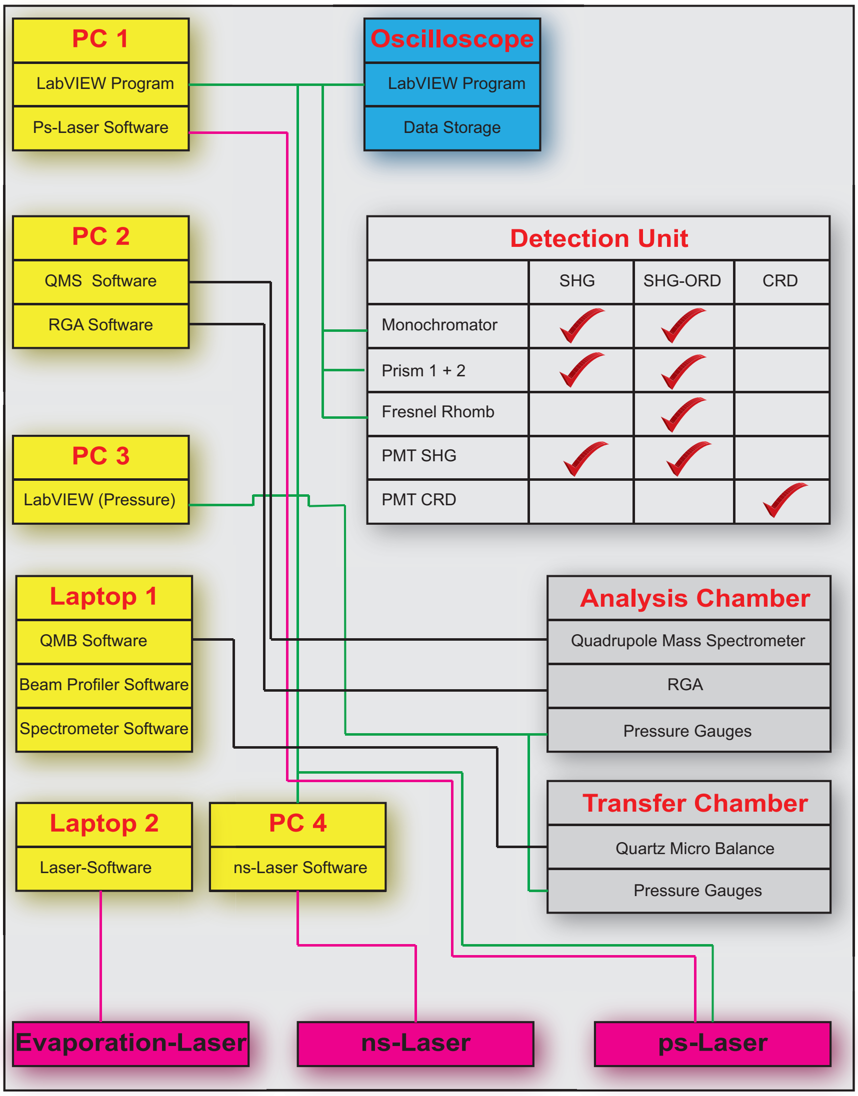

Figure 54: Schematic of the used hard- and software. The green lines illustrate the data transfer of the different LabVIEW programs while the black and purple lines show the data transfer of the software programs and the lasersystem, respectively.

A.2 LABVIEW PROGRAMS

Two LabVIEW programs were programmed in this work. They are depicted and described in the following. They simplified the daily work in laboratory to a great extent by fully automating data recording. Only the treatment and the handling of the programs are shown. The written program is not presented as this would be beyond the scope of this work.

The two programs described here are run on two different computers. The pressure program on PC3 is only connected to the vacuum gauges. The computer of the lab-program (PC1) is connected to the

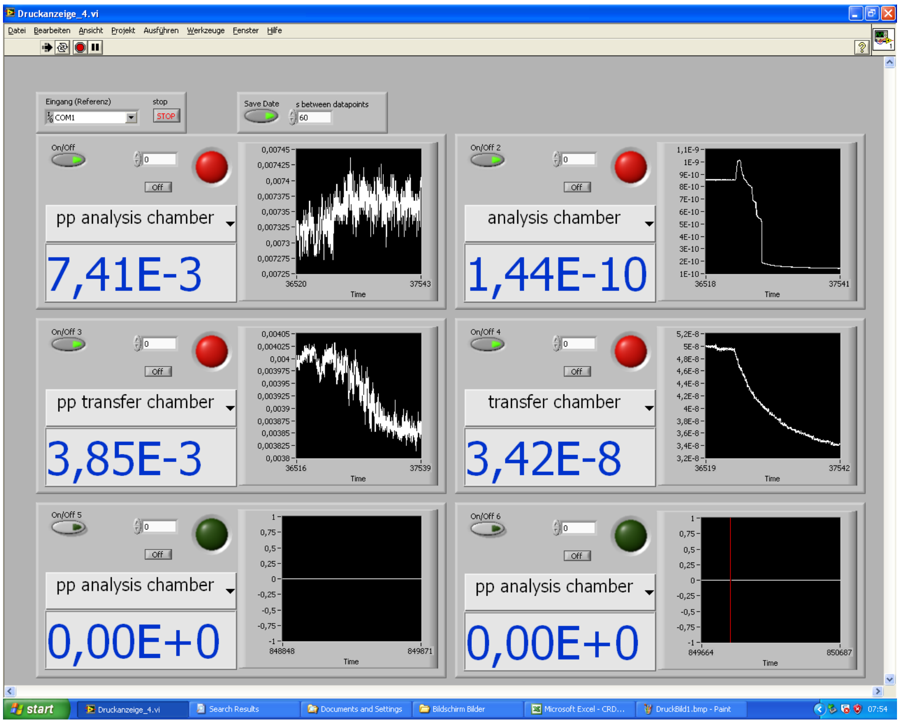

Figure 55: Picture of the LabVIEW pressure-control program. The pressure and its evolution of the analysis and transfer chamber as well as of their backing pumps are monitored. Channels 5 and 6 are switched off. In this picture the data are recorded every 60 seconds (see save-date button). In this example the critical value is set to zero and since the shown pressures exceed this value a red sign shines.

oscilloscope[2] where another LabVIEW program was programmed. Here, saving of the data occurs. It is furthermore connected to a monochromator (LOT-Oriel, Omni-λ 300), two movable pellin-broca-prisms, and a Fresnel Rhomb[3].

A.2.1 *Pressure-Control-Program*

For UHV experiments the exact value of the pressure in the chambers is always crucial and should permanently be monitored. Therefore, a program was written which numerically and graphically presents the pressure in the different chambers [4]. It allows for defining a critical value for the pressure in every chamber and gives a signal (graphically and acoustically) if this value is exceeded. It is also possible to save all values in tunable time intervals which was shown to be very important. Especially when the chambers are not controlled by the

---

[2] The oscilloscope (LeCroy, Waverunner 6051) is based on Microsoft Windows software.
[3] In Chapter 2 a more detailed description can be found.
[4] See Figure 16.

experimenter (i.e. at night time) the recording of the pressure-data is very useful. Also, during bake-out the evolution of the pressure in the chambers is of special interest. The program is depicted in Figure 55.

A.2.2 *Lab-Program*

The Lab-Program was programmed to provide automated measurements. All spectroscopic data presented in this thesis were measured with this program. The Lab-Computer (on which this program is running) can be connected to 3 different laser systems. The picosecond laser system, which was used for the data presented in this thesis, a nanosecond laser system (OPO) and an IR-Laser-System (used in ref. [77, 150]). In Figure 56 the user interface of the program is shown. In the upper left corner a laser-system can be selected. In the upper middle box the settings of the oscilloscope can be changed. Usually 100 counts were selected, thus for a S-SHG or a SHG-ORD measurement spectra are recorded a hundred times at each wavelength. In the greyed-out "timeout line" a value for the system to wait between two records must be defined. This increases the deadtime of the system but is necessary to ensure an errorless and smooth runing of the program. It should not be smaller than 70 ms[5]. In the upper right corner all important information about the ongoing measurement are presented and are self-explanatory. The blue bar shows the progress of the measurement graphically[6]. The end time of the measurement is calculated iteratively.

In the lower big box the parameter for different spectroscopic measurements can be selected. In the first tab one can choose between a SHG- or a CRD-measurement[7]. Since only SHG measurements are presented in this thesis the SHG-tab is chosen for the depicted picture. One of five tabs for different measurements can subsequently be chosen. At "Manual Adjustment" the wavelength of the chosen laser, the monochromator, the prisms and the Fresnel rhomb can be adjusted separately. This is very useful when adjusting the whole spectroscopic setup.

The second tab "Wavelength-Scan" is chosen when wavelength-scans, hence usual SHG-spectra are recorded. Then the chosen laser-system, the monochromator, the two pellin-broca prisms and the oscilloscope are all synchronized. The third tab "Polarisation-Scan" is chosen when a SHG-ORD measurements are performed. Here the Fresnel rhomb and the oscilloscope are synchronized. The scale in the blue bar in the upper right panel then switches from nm to de-

---

[5] This value is based on experience.

[6] In the example depicted here a wavelength scan from 740 nm to 800 nm was performed. It took 9 : 50 minutes and ended at 5 : 23 : 53 p.m..

[7] It is also possible to perform cavity ring-down (CRD) measurements with this experimental setup. The interested reader may refer to references [163, 150, 25].

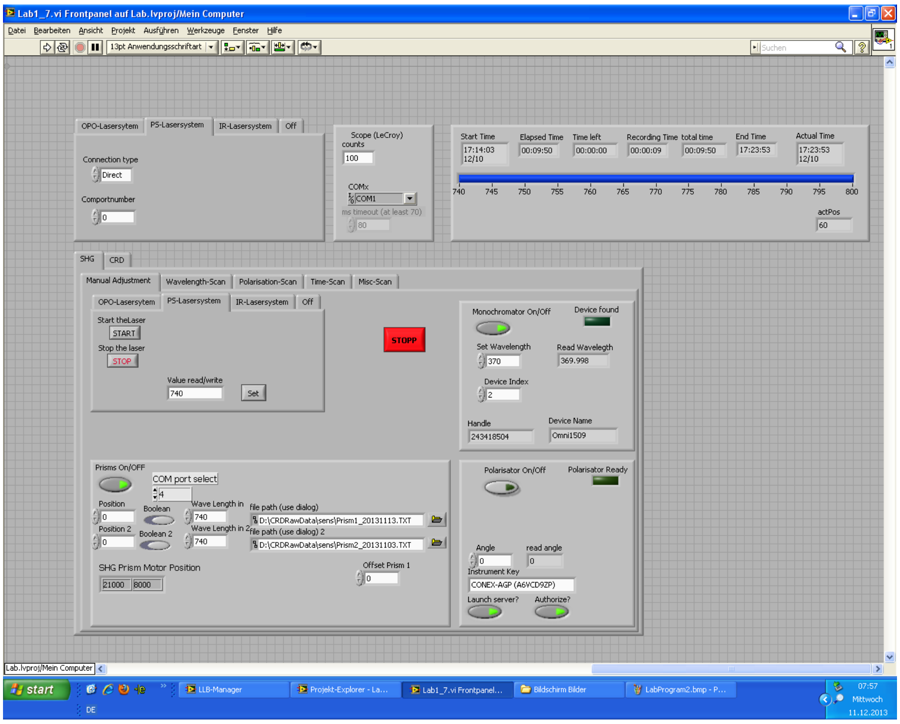

Connection type: Direct
Comportnumber: 0
Scope (LeCroy) counts: 100
COMx: COM1
ms timeout (at least 70): 80
Start Time: 17:14:03 12/10
Elapsed Time: 00:09:50
Time left: 00:00:00
Recording Time: 00:00:09
total time: 00:09:50
End Time: 17:23:53
Actual Time: 17:23:53 12/10
actPos: 60
Value read/write: 740
Set Wavelength: 370
Read Wavelegth: 369.998
Device Index: 2
Handle: 243418504
Device Name: Omni1509
COM port select: 4
Position: 0
Position 2: 0
Wave Length in: 740
Wave Length in 2: 740
file path (use dialog): D:\CRDRawData\sens\Prism1_20131113.TXT
file path (use dialog) 2: D:\CRDRawData\sens\Prism2_20131103.TXT
SHG Prism Motor Position: 21000 8000
Offset Prism 1: 0
Angle: 0
read angle: 0
Instrument Key: CONEX-AGP (A6VCD9ZP)

Figure 56: Picture of the Lab-program (see text).

grees. The fourth tab "Time-Scan" is chosen when time-dependent measurements at a given wavelength are performed. This is the case for oxidation measurements for example[8]. The last tab "Misc-Scan" is chosen when other parameters, which are not accessible by the LabVIEW program, must be modified during a measurement, i. e. the angle of incidence of the substrate. Then the user commands the program.

---

[8] Compare Section 106.

B

PS LASERSYSTEM

A new lasersystem was installed and used with the experimental setup during the work for this thesis[1]. It is composed of three different subsystems: a pump laser (EXPLA, PL2251), a harmonics unit (EKSPLA, H400) and a frequency conversion unit (EKSPLA, PG401/SH).

A scheme of the pump laser is shown in Figure 57. The pulse is generated by a laser diode made of Nd:YVO4. In the main oscillator, ps-pulses are generated via mode-locking and a saturable absorber. The emitted laser beam is partially separated. The main beam is used for seeding the regenerative amplifier; a small part is shone on a photodiode in order to monitor the intensity. A Nd:YAG crystal is used as the active material in the regenerative medium which is pumped by an additional laser diode. When the seeding beam enters the amplifier, a voltage is applied to the Pockel's cell (FR1) leading to a trapped beam in the cavity. When the maximum amplification is reached, the voltage is set to zero and the beam passes another amplification unit, that is based on a flash light pumped Nd:YAG crystal (R3). After passing some polarizers a beam with a wavelength of 1064 nm wavelength and a repetition rate of 20 Hz is emitted. The input beam enters the second part of the laser system, the harmonics unit (EKSPLA, H400), shown in Figure 58.

It contains a SHG and a THG unit to generate the second and respectively the third harmonic of the incident beam. This is done by nonlinear potassium dihydrogen phosphate crystals with a controlled

---

[1] Following description is based on ref. [129, 117, 164].

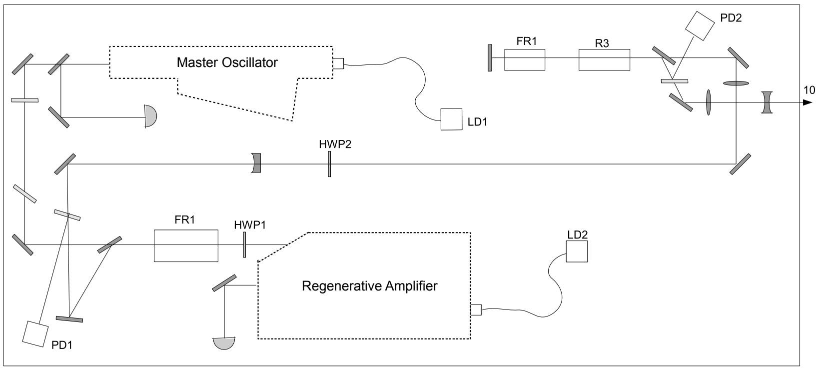

Figure 57: A scheme of the Pl2251 pump laser, containing the master oscillator, the laser dyes and the regenerative amplifier [129, 117].

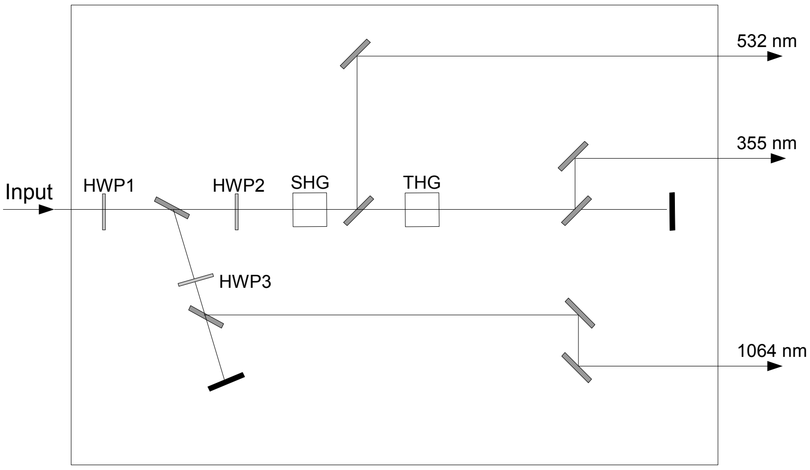

Figure 58: A scheme of the Harmonics Unit H400, containing a SHG and THG unit to generate the second and the third harmonic of the 1064 nm input beam [129, 117].

temperature to fulfill the phase-matching conditions and make nonlinear generation effective. In the current setup, only the third harmonic is used and it is separated by two dielectric mirrors. Typically the pulse energy is about 7, 5 mJ/pulse at the exit of the second unit. The third harmonic enters the third (conversion) unit, shown in Figure 59, where the OPA and the OPG process takes place and the laser light is tuned. The incident beam is split and 15% of the energy is led into a lithium triborate crystal, where it generates parametric fluorescence. The beam passes another pinhole and an Echelle grating to lower the spectral linewidth. Afterwards it enters the LBO crystal and takes part in the OPA process. The remaining 85% of the incident beam is delayed and is overlapped with the OPG beam in the LBO crystal. The angles of the LBO crystal and the grating are adjusted to tune the wavelength. If wavelengths between 210 nm and 420 nm are set, the SHG unit is moved into the beam line.

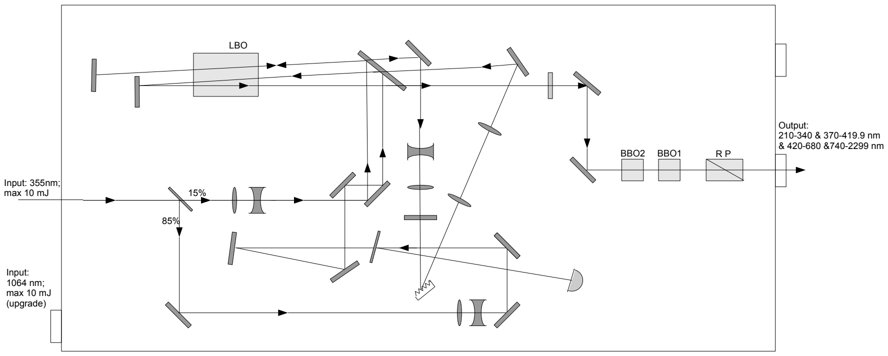

Figure 59: A scheme of the PG401/SH unit, where the tunable light is generated by a combined OPA and OPG process. The SHG unit containing the two BBO crystals can be moved into the beam line when the tunable light is set to UV light [129, 117].

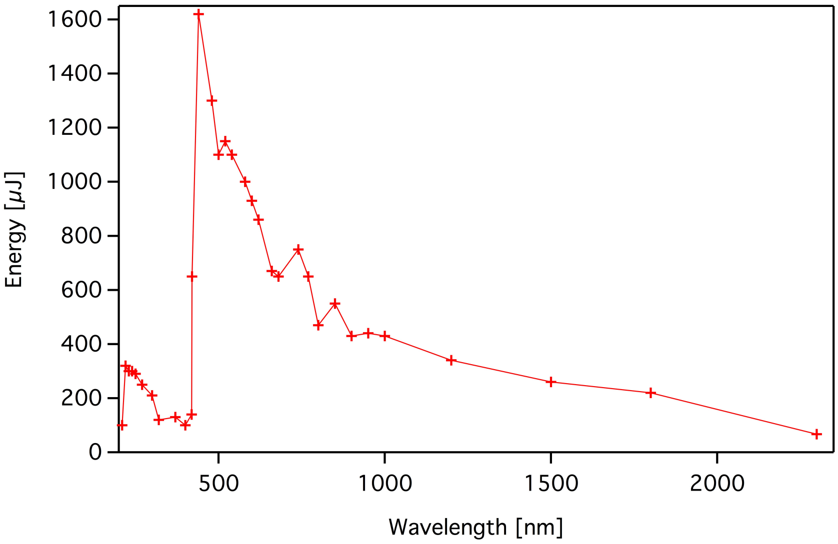

Figure 60: Pulse energy as a function of wavelength.

C

DETAILED SPECTRA

C.1 AG

C.1.1 *Example of Raw-Data Treatment*

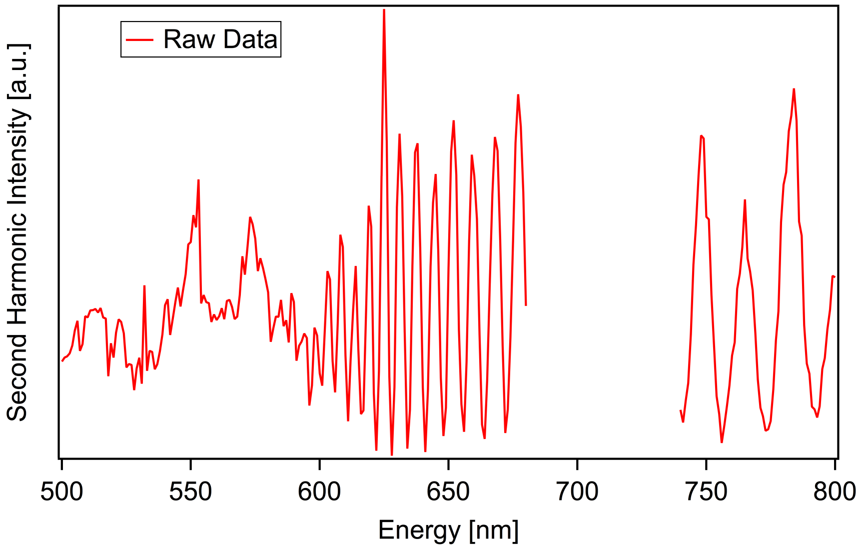

Figure 61: Raw signal from bare BK7 substrate. The oscillations in the spectrum above 600 nm result from the interference of the signals from both sides of the substrate. The other maxima result from the experimental setup (see Section 2.7 and ref. [140]).

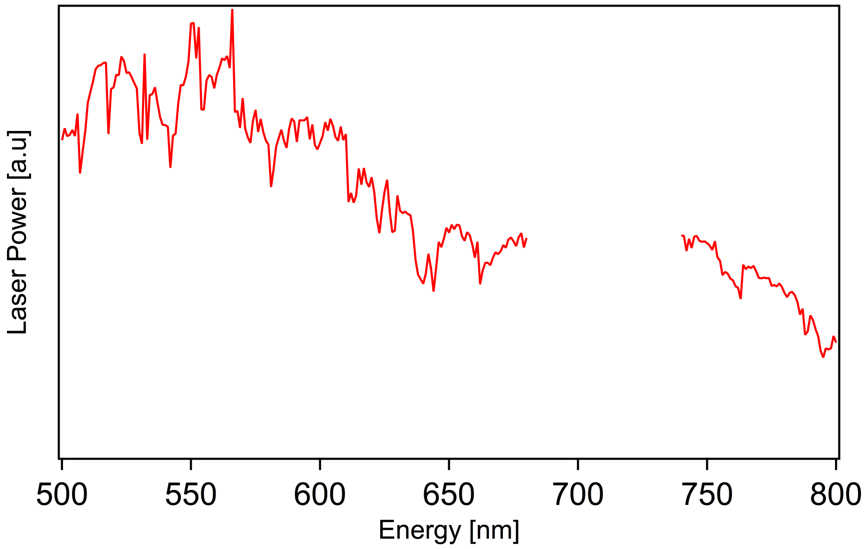

Figure 62: Recorded laser power.

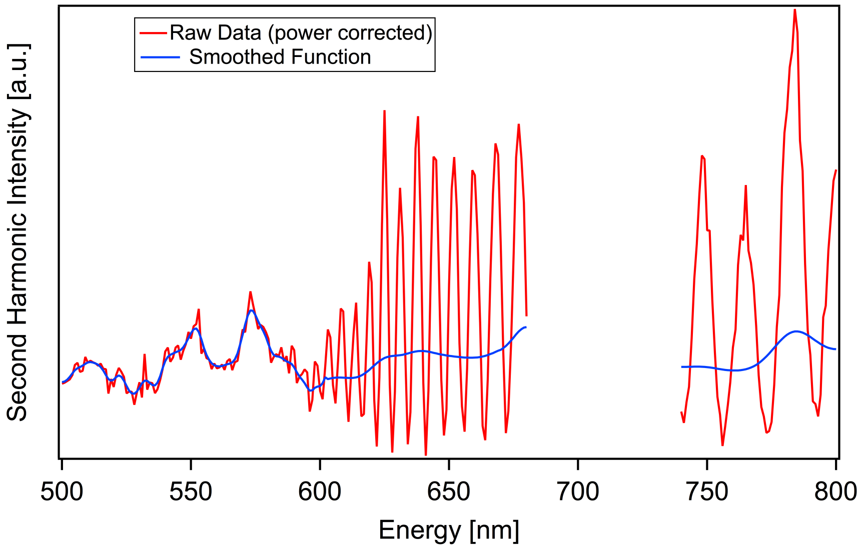

Figure 63: Power corrected raw data including a smoothed function. The smoothed function is multiplied by the transparency function of the substrate. It is used for the subsequent data treatment (see Section 2.7 and ref. [140]).

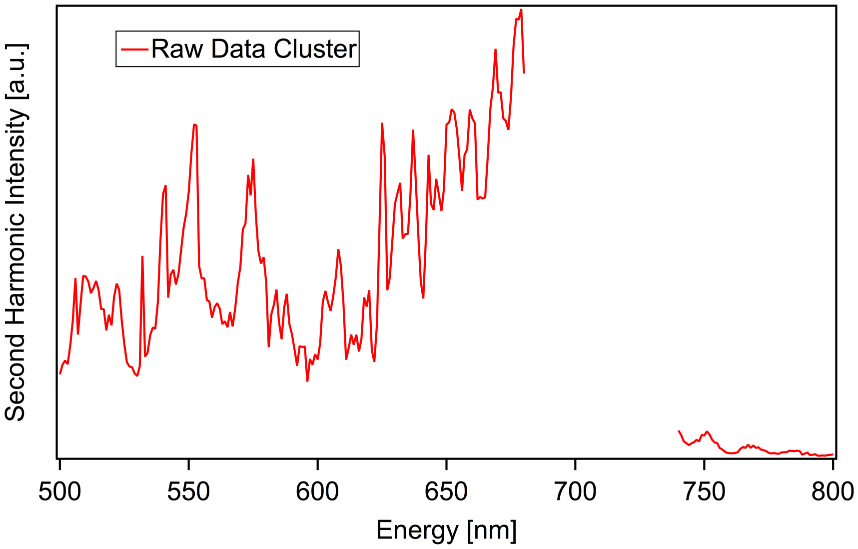

Figure 64: Raw spectrum of deposited clusters.

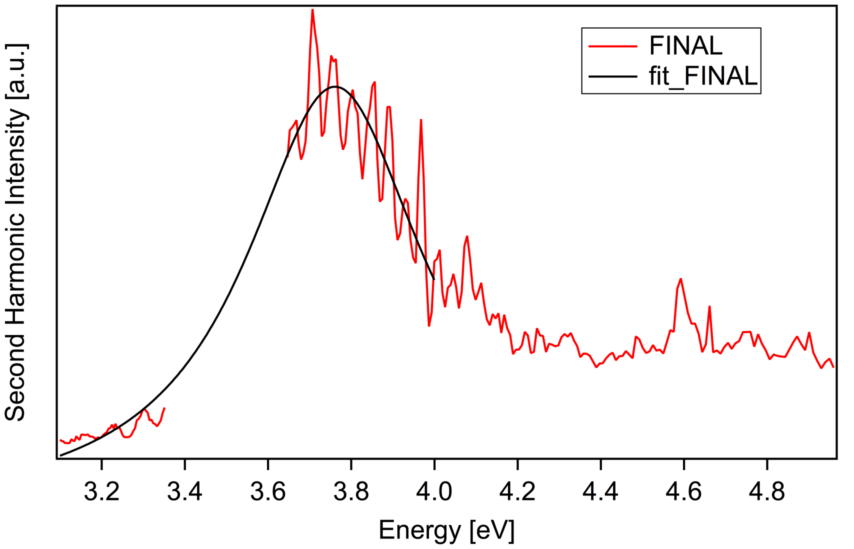

Figure 65: Final spectrum of deposited unselected clusters.

C.1.2 *Spectra of Unselected Clusters for Different Coverages*

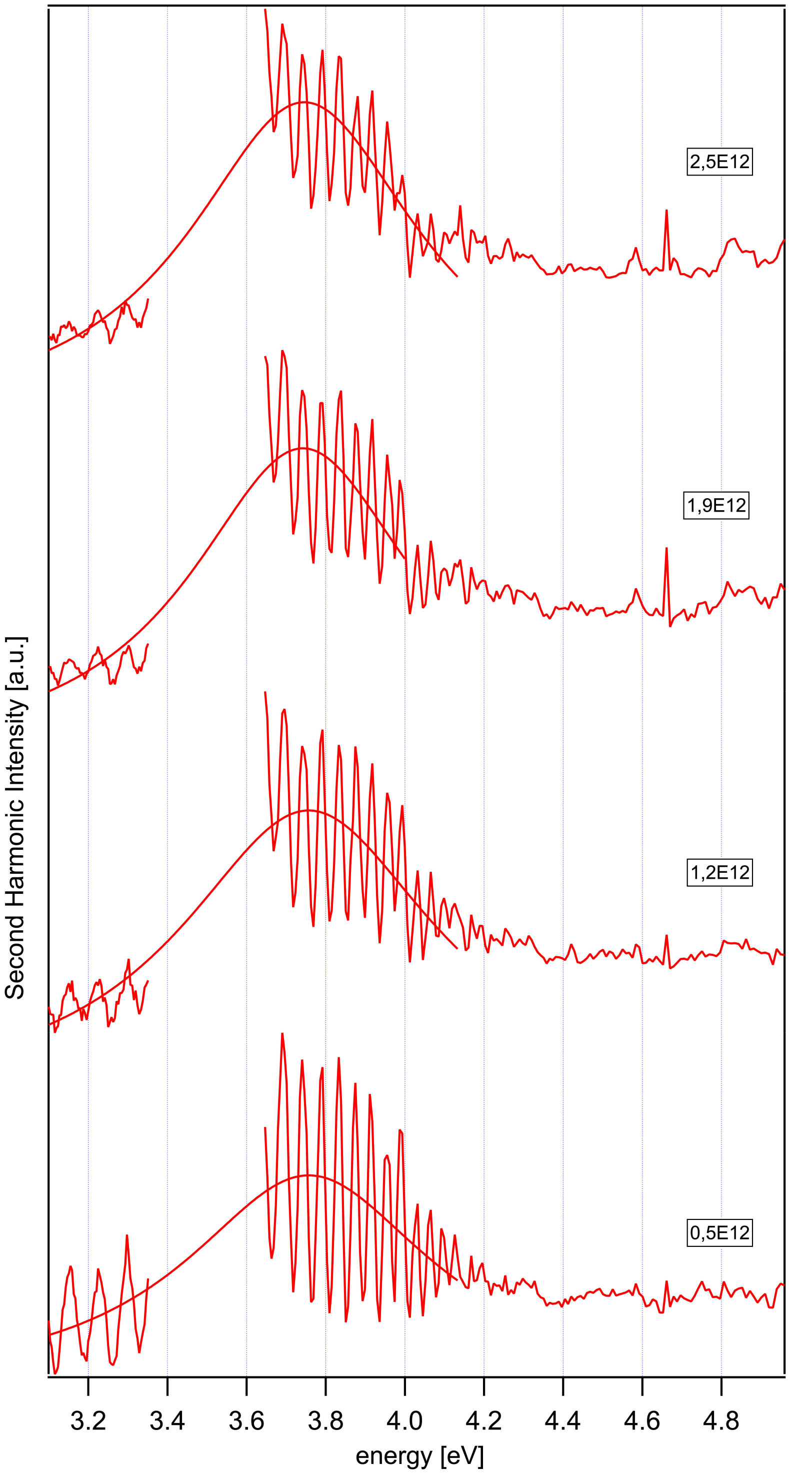

Figure 66: Spectra of unselected clusters.

C.1.3 *Detailed Spectra of Size Selected Clusters and Oxidation Fits*

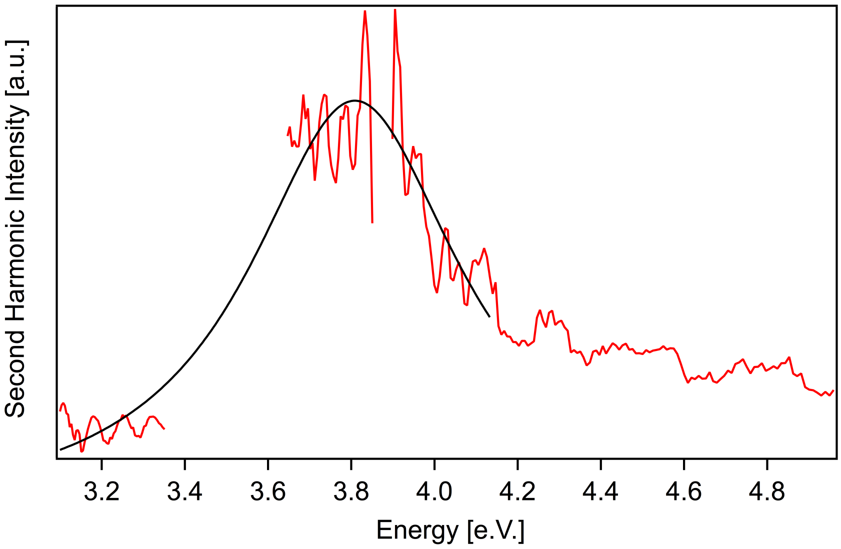

Figure 67: $Ag_{55\pm1}$

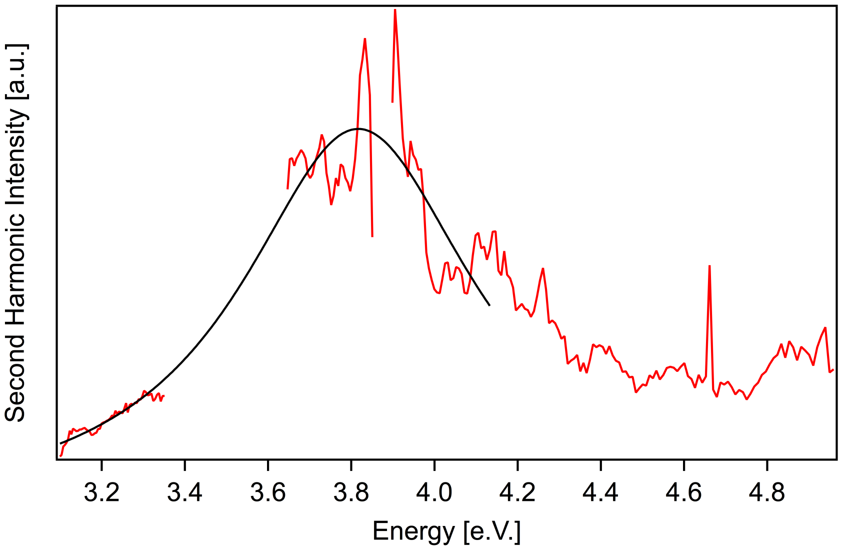

Figure 68: Ag_{45}

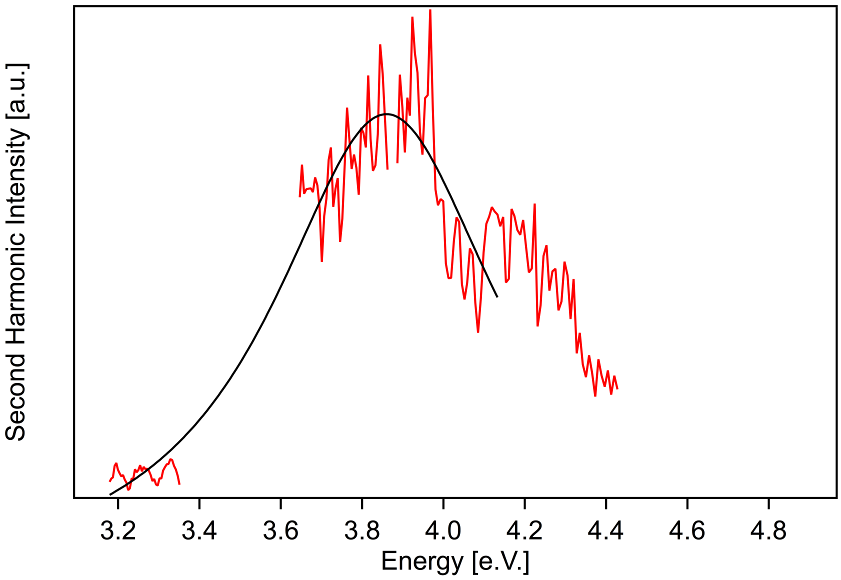

Figure 69: Ag_{40}

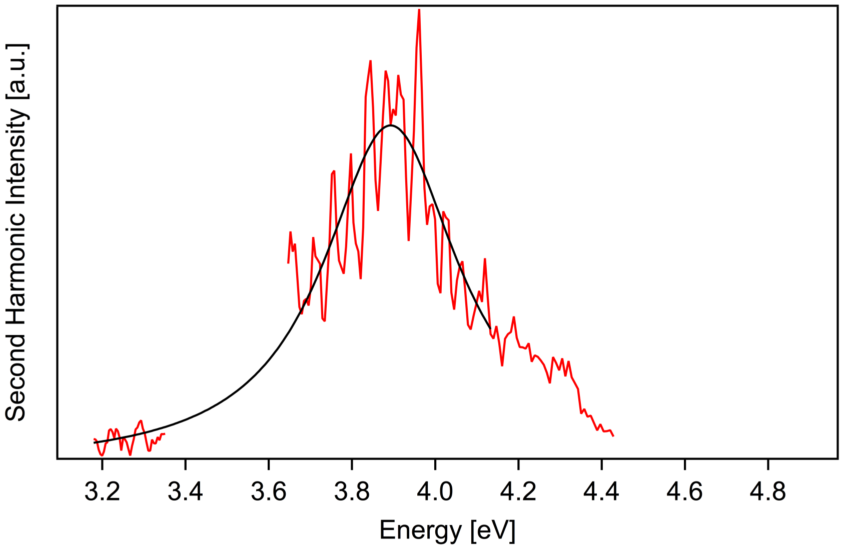

Figure 70: Ag_{35}

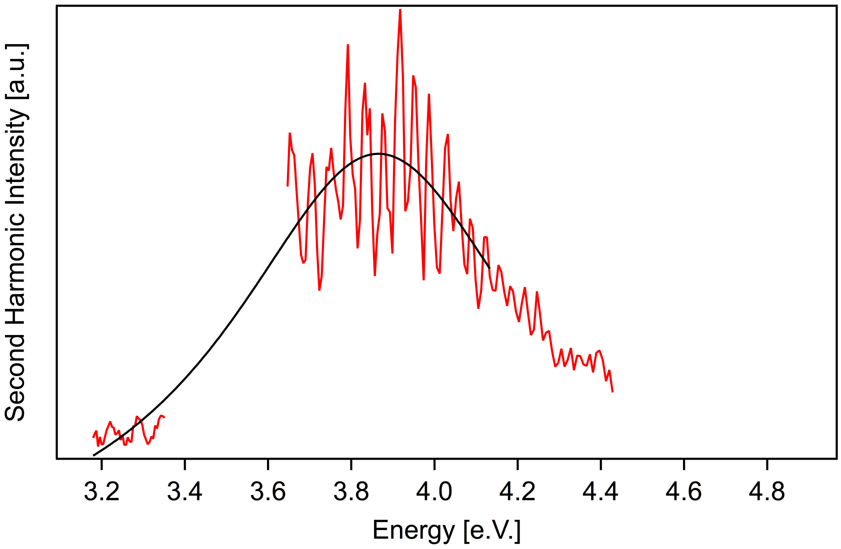

Figure 71: Ag_{27}

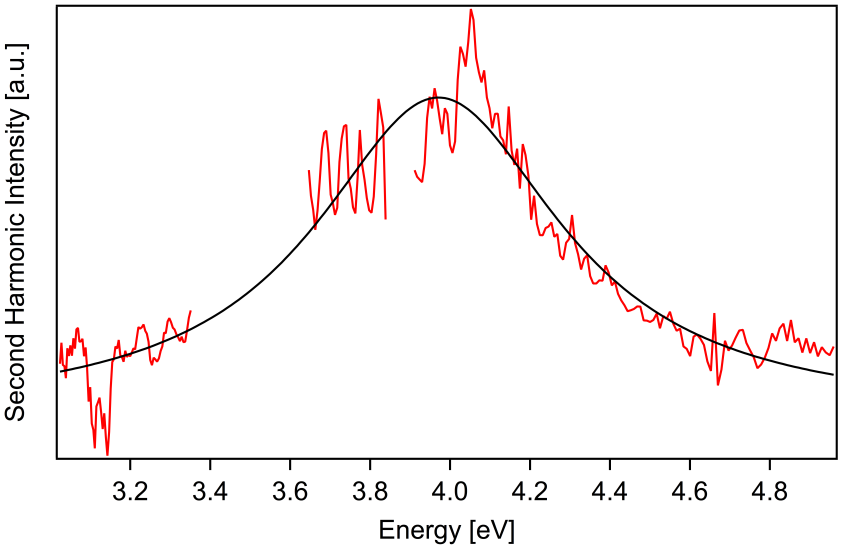

Figure 72: Ag_{21}

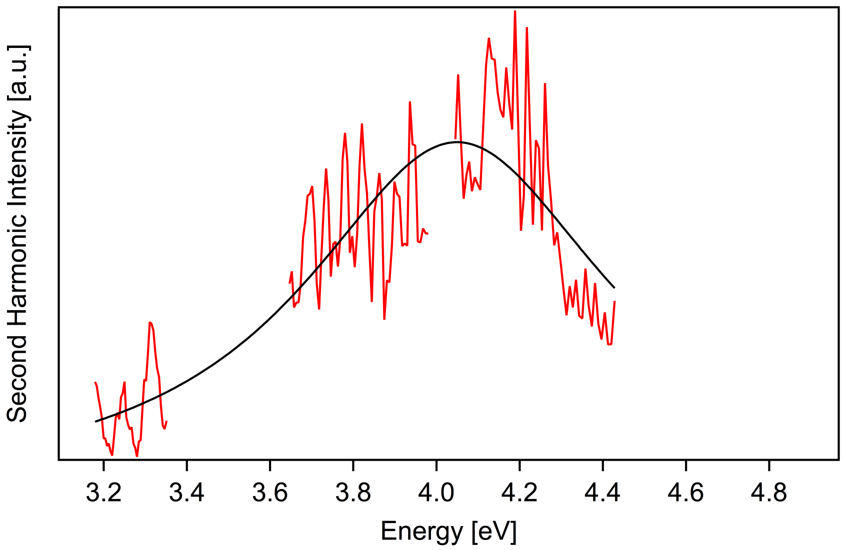

Figure 73: Ag_{18}

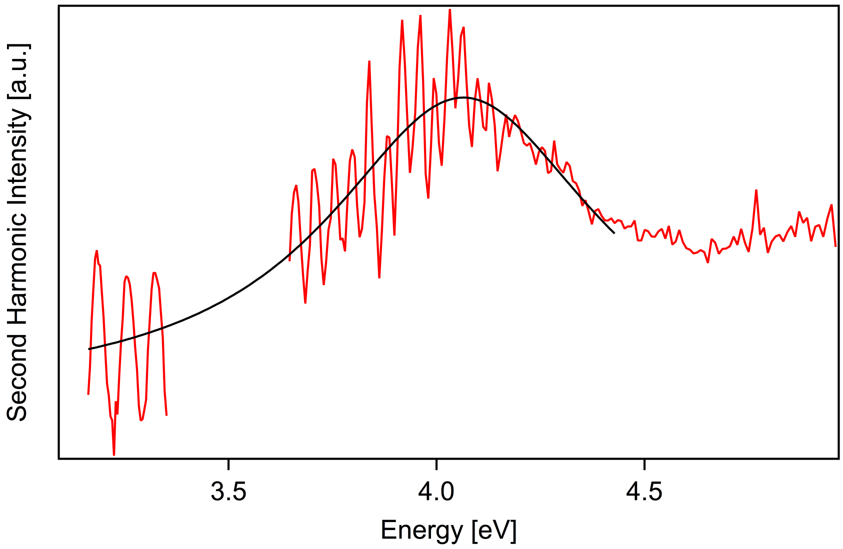

Figure 74: Ag_{15}

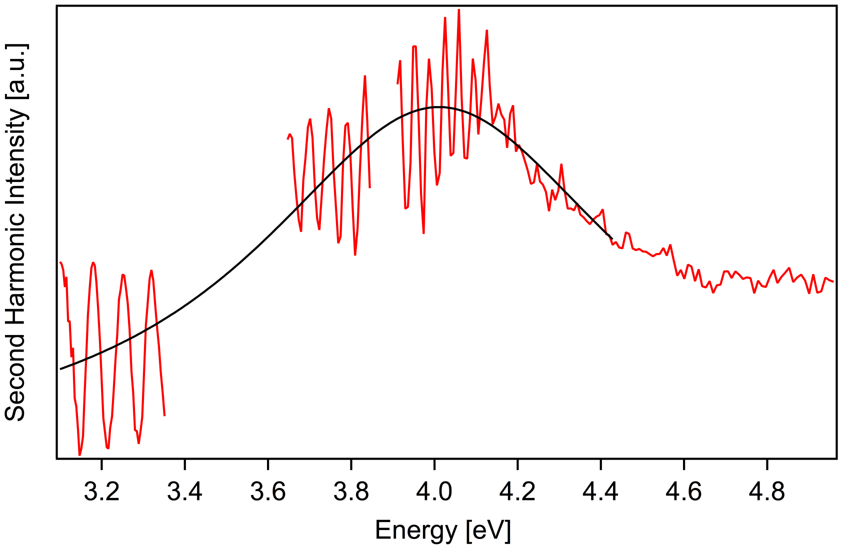

Figure 75: Ag_9

D

PICTURES OF LABORATORY

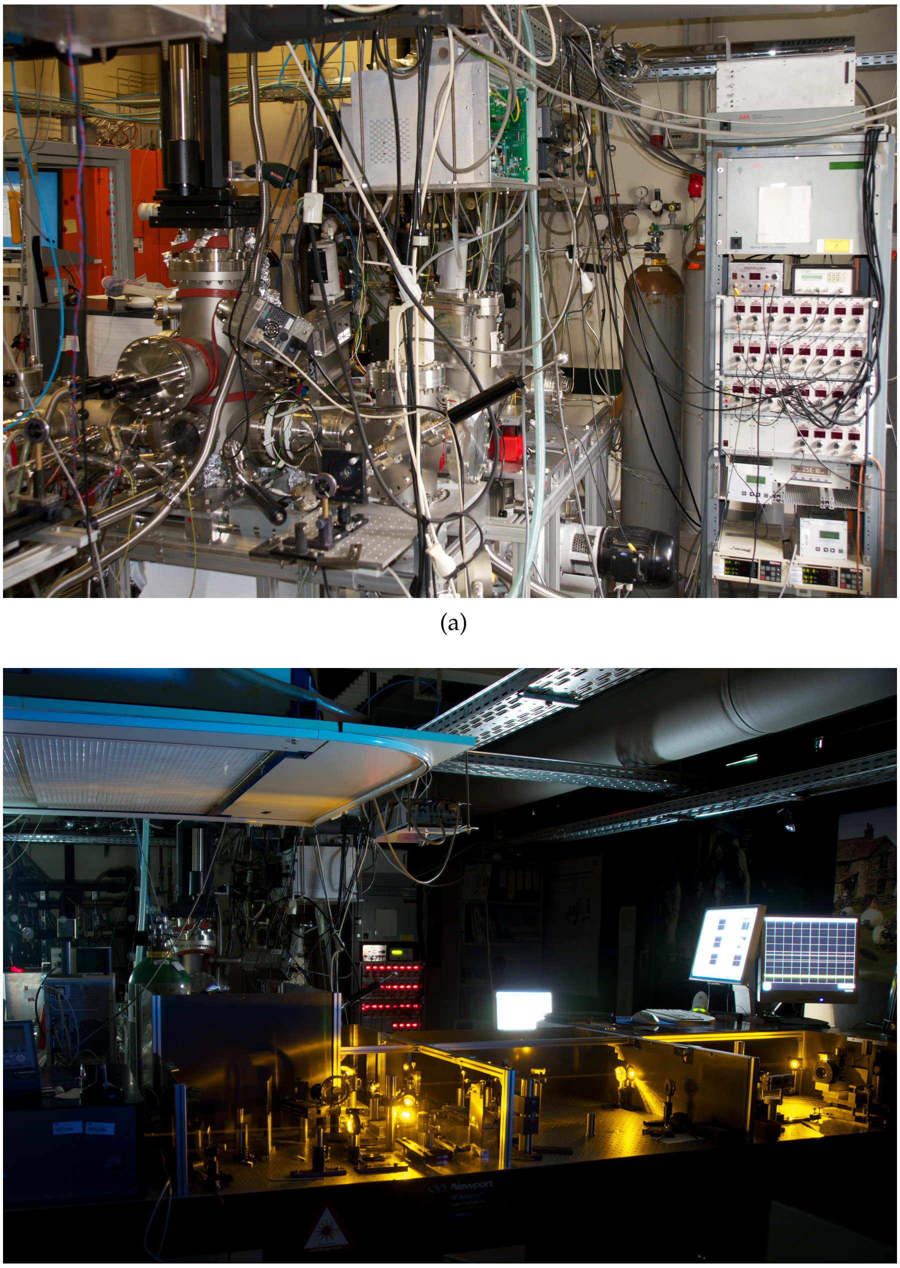

(a)

(b)

Figure 76: Pictures of the experimental setup. a) UHV chamber. b) Laser table including OPO lasersystem.

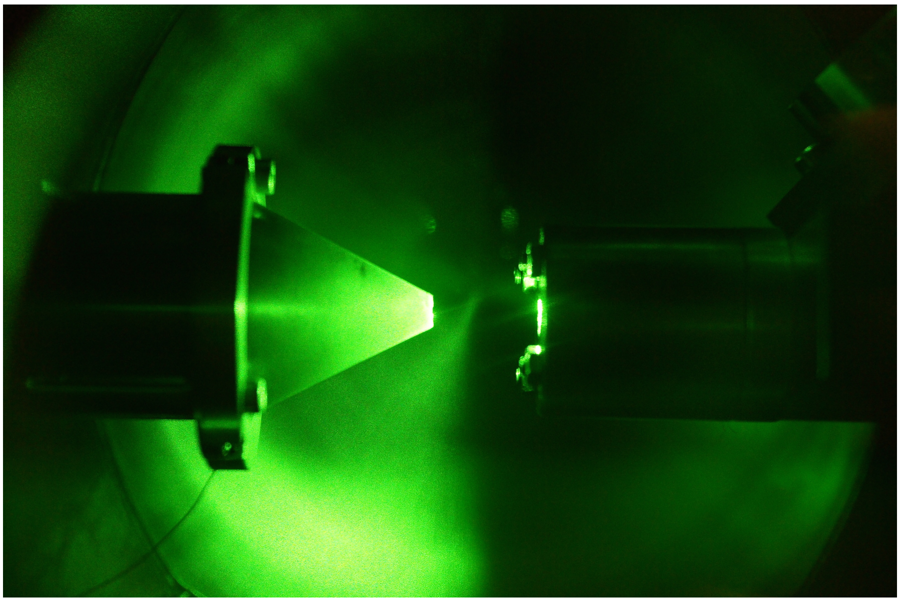

Figure 78: Picture of the skimmer and the nozzle during ablation.

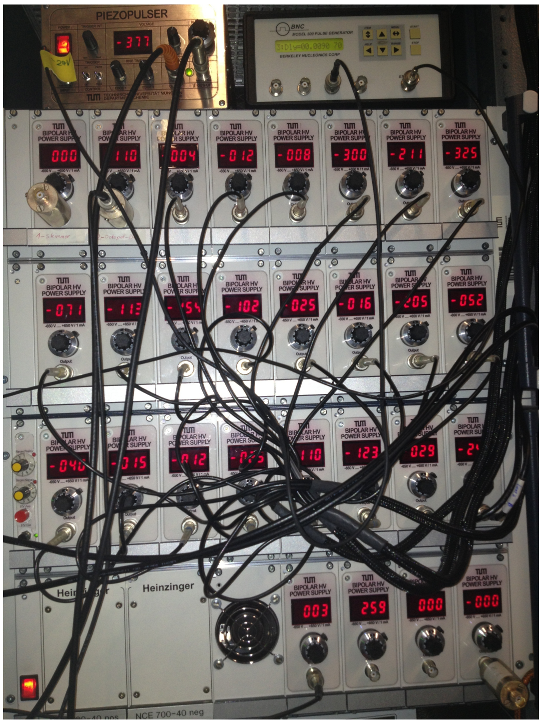

Figure 77: Picture of the power supply for the Einzel lenses inside the chamber. On the top left the "piezopulser" for the piezo, on the top right the pulsgenerator for the timedelay of the trigger from the ablation laser can be seen.

E

DECLARATION

Hiermit bestätige ich, dass die der Fakultät für Chemie der Technischen Universität München zur Promotionsprüfung vorgelegte Arbeit mit dem Tiel "Nonlinear Surface Spectroscopy of Supported Size-Selected Silver Clusters (n=9 – 55) and Supported Chiral 2, 2' - Dihydroxy - 1, 1'-Binaphthyl (Binol) Molecules" am Lehrstuhl für physikalische Chemie unter Anleitung und Betreuung durch Prof. Dr. Ueli Heiz ohne sonstige Hilfe erstellt und bei der Abfassung nur die gemäß § 6 Abs. 5 angegebenen Hilfsmittel benutzt worden sind. Die Dissertation ist in keinem anderen Prüfungsverfahren als Prüfungsleistung vorgelegt.

München, 16.06.14

Philipp Heister

F

PUBLICATIONS

- Philipp Heister, Tobias Lünskens, Martin Thämer, Constantin Walenta, Aras Kartouzian and Ueli Heiz. Nonlinear spectroscopy of supported size-selected silver clusters. 2014, *in prep.*

- Aras Kartouzian, Jerzy Antonowicz, Tobias Lünskens, Alexandra Lagogianni, Philipp Heister, Georgios Evangelakis and Roberto Felici. Toward cluster-assembled metallic glasses. *Materials Express. 4(3):228-234,* 2014

- Martin Thämer, Aras Kartouzian, Philipp Heister, Tobias Lünskens, Sabine Gerlach, and Ulrich Heiz. Small supported plasmonic silver clusters. *Small*, 2014.

- Philipp Heister, Tobias Lünskens, Martin Thämer, Aras Kartouzian, Sabine Gerlach, Thierry Verbiest and Ueli Heiz. Orientational changes of supported chiral 2,2′-dihydroxy- 1,1′binaphthyl molecules. *Phys. Chem. Chem. Phys.* 16:7299-7306, 2014.

- Aras Kartouzian, Philipp Heister, Martin Thämer, Sabine Gerlach, and Ulrich Heiz. In-line reference measurement for surface second harmonic generation spectroscopy. *J. Opt. Soc. Am. B*, 30(3):541–548, Mar 2013.

- M. Vanbel, S. Vandendriessche, M. A. van der Veen, D. Slavov, P. Heister, R. Paesen, V. K. Valev, M. Ameloot, and T. Verbiest. Second-harmonic generation from complex chiral samples, *Proc. SPIE*, 2013.

- Martin Thämer, Aras Kartouzian, Philipp Heister, Sabine Gerlach, Martin Tschurl, Ulrich Boesl, and Ulrich Heiz. Linear and nonlinear laser spectroscopy of surface adsorbates with sub-monolayer sensitivity. *The Journal of Physical Chemistry C*, 116(15):8642–8648, 2012.

- B. Gruner, M. Schlesinger, Ph. Heister, W. T. Strunz, F. Stienkemeier, and M. Mudrich. Vibrational relaxation and dephasing of Rb_2 attached to helium nanodroplets. *Phys. Chem. Chem. Phys.*, 13:6816–6826, 2011.

- M. Mudrich, Ph. Heister, T. Hippler, Ch. Giese, O. Dulieu, and F. Stienkemeier. Spectroscopy of triplet states of Rb_2 by femtosecond pump-probe photoionization of doped helium nanodroplets. *Phys. Rev. A*, 80:042512, Oct 2009.